



**HAL**  
open science

# Investigation of liquid water heterogeneities in large area PEM fuel cells using a two-phase flow multiphysics model.

Erwan Tardy

## ► To cite this version:

Erwan Tardy. Investigation of liquid water heterogeneities in large area PEM fuel cells using a two-phase flow multiphysics model.. Materials Science [cond-mat.mtrl-sci]. Université Grenoble Alpes [2020-..], 2021. English. NNT : 2021GRALI103 . tel-04610423

**HAL Id: tel-04610423**

**<https://theses.hal.science/tel-04610423>**

Submitted on 13 Jun 2024

**HAL** is a multi-disciplinary open access archive for the deposit and dissemination of scientific research documents, whether they are published or not. The documents may come from teaching and research institutions in France or abroad, or from public or private research centers.

L'archive ouverte pluridisciplinaire **HAL**, est destinée au dépôt et à la diffusion de documents scientifiques de niveau recherche, publiés ou non, émanant des établissements d'enseignement et de recherche français ou étrangers, des laboratoires publics ou privés.

## **THÈSE**

Pour obtenir le grade de

### **DOCTEUR DE L'UNIVERSITÉ GRENOBLE ALPES**

Spécialité : MEP : Mécanique des fluides Energétique, Procédés

Arrêté ministériel : 25 mai 2016

Présentée par

**Erwan TARDY**

Thèse dirigée par Pr. Yann BULTEL  
et codirigée par Dr. Jean-Philippe POIROT-CROUVEZIER

préparée au sein du Commissariat à l'Énergie Atomique et aux  
Énergies Alternatives  
dans l'École Doctorale I-MEP2 - Ingénierie - Matériaux, Mécanique,  
Environnement, Énergétique, Procédés, Production

**Étude de la distribution de l'eau liquide dans les piles  
à combustible PEM de grande surface à l'aide d'un  
modèle multiphysique d'écoulement diphasique.**

**Investigation of liquid water heterogeneities in large  
area PEM fuel cells using a two-phase flow mul-  
tiphysics model.**

Thèse soutenue publiquement le **10 décembre 2021**, devant le  
jury composé de :

**M. Laurent DAVOUST**

Professeur des universités, Institut Polytechnique de Grenoble  
Président du jury

**Mme Sophie DIDIERJEAN**

Professeur des universités, Université de Lorraine  
Rapporteuse

**M. Marc PRAT**

Directeur de recherche, Institut de Mécanique des Fluides de Toulouse  
Rapporteur

**M. Yann BULTEL**

Professeur des universités, Institut Polytechnique de Grenoble  
Directeur de thèse

**M. Jean-Philippe POIROT-CROUVEZIER**

Docteur, CEA-LITEN, Grenoble  
Invité

**M. Pascal SCHOTT**

Docteur, CEA-LITEN, Grenoble  
Invité





## **Acknowledgements / Remerciements**

Je tiens tout d'abord à remercier l'ensemble du personnel du Département de l'Électricité et de l'Hydrogène pour les Transports et du Service des Technologies PEMFC pour leur accueil chaleureux. Je souhaite également remercier le CEA-LITEN et la cellule Handicap pour avoir tout mis en œuvre pour faciliter et adapter l'accessibilité de mon poste de travail. Tout a été pensé pour que je puisse travailler dans de bonnes conditions malgré mon handicap.

Un immense merci à mon directeur de thèse, Yann Bultel, pour son accompagnement sans faille tout au long de mes travaux. Tu as toujours été présent ! Le bon déroulement de ma thèse n'aurait pu se faire sans toi.

Je remercie sincèrement Messieurs Jean-Philippe Poirot-Crouvezier et Pascal Schott pour leur aide précieuse et leur soutien. Leur encadrement a été tout autant qualitatif que quantitatif. Cette tâche complexe qu'est l'aboutissement d'une thèse est une réussite grâce à vous !

Je remercie chaleureusement Marion Chandestrès pour son accompagnement lors de mes premières années de thèse. Vos enseignements et votre pédagogie m'ont beaucoup aidé !

Un grand merci à Christophe Morel pour les nombreuses heures passées à m'aider à décortiquer cette théorie si complexe que sont les écoulements multiphasiques dans les milieux poreux. Sans vous, ce travail de fond aurait duré plusieurs thèses ! Je remercie également Guillaume Serre pour son implication et ses connaissances précieuses sur le diphasique.

Je tiens à remercier les membres du jury pour l'intérêt qu'ils ont bien voulu porter à mon travail. Je remercie particulièrement Sophie Didierjean et Marc Pratt pour leurs remarques pertinentes dans leurs rapports et lors de ma présentation. Merci à Laurent Davoust d'avoir présidé ma soutenance et examiné mon manuscrit.

Je remercie mes parents de m'avoir aidé et soutenu quotidiennement pendant ces quatre années intenses.

Enfin, je remercie toutes les personnes qui ont contribué de quelque manière à cette thèse.

*Je dédie cette thèse à mes parents.*

*All models are wrong, but some are useful.*

*– George E. P. Box –*

## **Abstract**

The Proton Exchange Membrane Fuel Cell (PEMFC) is a promising candidate for many applications particularly for the transportation in order to decarbonize this sector. Of the barriers, cost and durability represent two of the most significant challenges to achieving clean, reliable and cost-effective fuel cell systems. Proper management of the liquid water and heat produced in PEM fuel cells remains crucial to increase both its performance and durability. Indeed, large liquid water and temperature variations in the cell may accelerate long-term structural problems until irreversible degradation (membrane micro-cracks, pinholes, alteration of the catalyst chemical composition, etc.).

In this study, the complex theory of two-phase flow in PEM fuel cells is reviewed with a focus on the local volume-average of the conservation equations in a porous medium. From this theoretical analysis, two multiphysics and multi-component models are developed considering one-fluid and two-fluid thermodynamics to investigate the liquid water heterogeneities in large area PEM fuel cells. Both models consider the cell as a multi-layered system where each component is accurately in-plane discretized. This pseudo-3D approach is implemented in the commercial COMSOL Multiphysics® software to simulate a large surface cell operation with a reasonable computing time while keeping the real flow-field design. Numerical results are compared to liquid water measurements obtained by neutron imaging for several operating conditions. The advantages and drawbacks of both models are discussed. In addition, a sensitivity study is performed to analyze some key parameters in the modeling of water transport mechanisms. Finally, the numerical water distribution is examined in each component of the cell with both models.

## Résumé

La pile à combustible à membrane échangeuse de protons (ou PEMFC selon l'acronyme anglais) est une option sérieuse dans de nombreuses applications notamment pour décarboner le secteur du transport. Parmi les obstacles, le coût et la durabilité représentent les deux défis principaux à relever pour réaliser des systèmes de piles à combustible propres, fiables et rentables. Une bonne gestion de l'eau liquide et de la chaleur produites dans les piles à combustible de type PEM est cruciale pour augmenter à la fois ses performances et sa durabilité. En effet, de grandes variations d'eau liquide et de température peuvent détériorer de façon irréversible la structure des cellules (microfissures dans la membrane, changement de la composition chimique des catalyseurs, etc.).

Dans cette étude, la théorie complexe des écoulements diphasiques dans les piles à combustible de type PEM est décrite en mettant l'accent sur la moyenne volumique locale des équations de conservation en milieu poreux. À partir de cette analyse théorique, deux modèles multiphysiques et multi-composants ont été développés en considérant dans un premier temps un écoulement monophasique puis diphasique pour étudier les hétérogénéités de l'eau liquide dans les piles à combustible de grande surface. Les deux modèles considèrent la cellule comme un système multicouche où chaque composant est discrétisé selon son épaisseur. Cette approche pseudo-3D est implémentée dans le logiciel commercial COMSOL Multiphysics® pour simuler le fonctionnement d'une cellule grande surface avec un temps de calcul raisonnable tout en représentant de manière fidèle le design des plaques bipolaires. Les résultats numériques sont comparés à des mesures d'eau liquide obtenues par imagerie neutron pour plusieurs conditions opératoires. Les avantages et inconvénients des deux modèles sont discutés. De plus, une étude de sensibilité est réalisée pour analyser certains paramètres clés dans la modélisation des mécanismes de transport de l'eau. Enfin, la distribution de l'eau est examinée dans les différents composants d'une cellule avec les deux modèles.

# Contents

<b>Acknowledgements / Remerciements .....</b>	<b>3</b>
<b>Abstract / Résumé .....</b>	<b>6</b>
<b>Nomenclature.....</b>	<b>13</b>
<b>General Introduction .....</b>	<b>20</b>

## Chapter I – STATE OF THE ART

<b>Introduction .....</b>	<b>23</b>
<b>1. Mobility .....</b>	<b>23</b>
<b>2. PEM Fuel Cell Electric Vehicles .....</b>	<b>24</b>
2.1 Hydrogen for Mobility.....	24
2.2 Operating Principle of a PEM Fuel Cell.....	26
2.3 PEM Fuel Cell Components .....	27
2.3.1 Membrane.....	28
2.3.2 Catalyst Layer .....	29
2.3.3 Gas Diffusion Layer and Micro-Porous Layer .....	29
2.3.4 Membrane-Electrode Assembly.....	31
2.3.5 Bipolar Plates.....	31
2.4 PEM Fuel Cell System .....	32
2.5 Technical Targets for Fuel Cell Systems for Transportation Applications .....	34
<b>3. Water Management in PEM Fuel Cells .....</b>	<b>35</b>
3.1 Condensation and Evaporation .....	35
3.2 Water Management Mechanisms .....	35
3.2.1 Water Transport through the Membrane .....	35
3.2.2 Capillarity in Porous Layers.....	39
3.2.3 Convection Transport of Water in the Gas Channels .....	40
3.3 Effect of Water Management on PEM Fuel Cells Performance and Degradation ....	41
3.3.1 Membrane Dehydration .....	41
3.3.2 Cell Water Flooding.....	42
<b>4. State of the Art of Numerical PEMFC Models.....</b>	<b>43</b>
<b>Conclusion.....</b>	<b>46</b>

**Chapter II – MODEL FORMULATION OF THERMOFLUID  
MECHANICS IN PEM FUEL CELLS**

<b>Introduction</b> .....	<b>49</b>
<b>1. Interest of Averaging</b> .....	<b>49</b>
<b>2. Porous Medium</b> .....	<b>50</b>
2.1 Porosity .....	50
2.2 Representative Elementary Volume .....	52
<b>3. Single-Phase Flow</b> .....	<b>53</b>
3.1 Mathematical Averages .....	54
3.1.1 <i>Local Volume-Average</i> .....	54
3.1.2 <i>Local Volume-Average Associated to the Fluid-Phase</i> .....	54
3.1.3 <i>Local Intrinsic-Average Associated with the Fluid-Phase</i> .....	54
3.2 Theorems .....	55
3.2.1 <i>Theorem of the Volume-Average of a Gradient</i> .....	55
3.2.2 <i>Theorem of the Volume-Average of a Divergence</i> .....	56
3.3 Local Volume-Averaged Mass Equation .....	56
3.4 Favre Averaging .....	57
3.5 Local Volume-Averaged Species Mass Conservation Equation .....	57
3.6 Local Volume-Averaged Momentum Equation .....	59
3.7 Darcy’s Law .....	61
3.8 Local Volume-Averaged Energy Conservation Equation .....	62
<b>4. Two-Phase Flow</b> .....	<b>63</b>
4.1.1 <i>Multiphase Medium</i> .....	63
4.1.2 <i>k-Phase Volume Fraction</i> .....	63
4.2 Topological Equations .....	64
4.2.1 <i>Phase Indicator Function</i> .....	64
4.2.2 <i>Reynolds Transport Theorem</i> .....	64
4.3 Mathematical Averages .....	65
4.3.1 <i>Local Volume-Average Associated with the k-Phase</i> .....	65
4.3.2 <i>Local Intrinsic-Average Associated with the k-Phase</i> .....	65
4.4 Theorems .....	66
4.4.1 <i>Theorem of the Volume-Average of a Gradient</i> .....	66
4.4.2 <i>Theorem of the Volume-Average of a Divergence</i> .....	66
4.5 Local Volume-Averaged Mass Equation .....	67

4.6	Local Volume-Averaged Species Mass Conservation Equation.....	67
4.7	Local Volume-Averaged Momentum Equation .....	68
4.8	The Extended Two-Phase Darcy's Law .....	71
	<b>Conclusion.....</b>	<b>72</b>

### Chapter III – ONE-FLUID MODEL

	<b>Introduction .....</b>	<b>74</b>
<b>1.</b>	<b>Pseudo-3D Formulation.....</b>	<b>74</b>
<b>2.</b>	<b>Principle .....</b>	<b>75</b>
2.1	Integration Development .....	75
2.2	Advantages and Limitations .....	78
<b>3.</b>	<b>One-Fluid Equations .....</b>	<b>78</b>
3.1	Geometrical Domain.....	78
3.1.1	<i>Gas Channels and Gas Diffusion Electrodes .....</i>	<i>78</i>
3.1.2	<i>Cooling Circuit.....</i>	<i>79</i>
3.2	Electrochemical Model.....	82
3.2.1	<i>Reversible Potential .....</i>	<i>82</i>
3.2.2	<i>Overpotential.....</i>	<i>83</i>
3.2.3	<i>Cell Internal Resistance .....</i>	<i>83</i>
3.3	Source Terms .....	84
3.3.1	<i>Electrochemical Source Term .....</i>	<i>84</i>
3.3.2	<i>Heat Source Term.....</i>	<i>85</i>
3.4	Condensation Model.....	86
<b>4.</b>	<b>One-Fluid and Phase-Separated Models Analysis .....</b>	<b>87</b>
4.1	Models Comparison.....	87
4.1.1	<i>Equal Saturations between the Two Models .....</i>	<i>88</i>
4.1.2	<i>Equal Pressure Drops between the Two Models .....</i>	<i>89</i>
4.2	Sensitivity Analysis .....	91
4.2.1	<i>Sensitivity Analysis to C Parameter .....</i>	<i>91</i>
4.2.2	<i>Sensitivity Analysis to the Velocity Ratio .....</i>	<i>93</i>
<b>5.</b>	<b>Stack Design.....</b>	<b>95</b>
<b>6.</b>	<b>Numerical Procedure .....</b>	<b>96</b>
<b>7.</b>	<b>Results and Discussion.....</b>	<b>97</b>
7.1	Sensitivity Analysis to Water Transport Coefficients .....	97

7.1.1	<i>Sensitivity Analysis to EO Drag Coefficients</i> .....	98
7.1.2	<i>Sensitivity Analysis to Membrane Diffusion Coefficients</i> .....	99
7.2	Low Power Operating Conditions .....	100
7.2.1	<i>Low Current Density</i> .....	100
7.2.2	<i>High Current Density</i> .....	102
7.2.3	<i>Liquid Water Thickness along the Reference Cut Line</i> .....	102
7.3	Analysis of Results at the Local Level .....	103
7.3.1	<i>Water Distribution over the Cell Surface in Each Layer</i> .....	103
7.3.2	<i>Numerical Water Transport through the Membrane</i> .....	104
7.3.3	<i>Water Distribution at Rib/Channel Scale</i> .....	105
7.4	High Power Operating Conditions .....	108
<b>Conclusion</b> .....		<b>109</b>

## Chapter IV – TWO-FLUID MODEL

<b>Introduction</b> .....		<b>111</b>
<b>1.</b>	<b>Pseudo-3D Formulation</b> .....	<b>111</b>
<b>2.</b>	<b>Two-Fluid Equations</b> .....	<b>113</b>
2.1	Model Presentation .....	113
2.2	Source Terms .....	114
<b>3.</b>	<b>Stack Design</b> .....	<b>117</b>
<b>4.</b>	<b>Numerical Procedure</b> .....	<b>118</b>
4.1	Preliminary Simulation with a 1D Model.....	118
4.2	Meshing and Resolution with the Pseudo-3D Model .....	122
<b>5.</b>	<b>Results and discussion</b> .....	<b>123</b>
5.1	Two-Fluid Model versus Experimental Tests .....	123
5.2	Two-Fluid Model versus One-Fluid Model.....	126
5.2.1	<i>Total Liquid Water Comparison</i> .....	126
5.2.2	<i>Liquid Water Component Comparison</i> .....	128
5.3	Water Distribution over the Cell Surface in Each Layer .....	130
<b>Conclusion</b> .....		<b>133</b>
<b>General Conclusion</b> .....		<b>135</b>
<b>References</b> .....		<b>137</b>

<b>Appendix .....</b>	<b>147</b>
Appendix A: Local Volume-Averaged Mass Equation.....	147
Appendix B: Local Volume-Averaged Species Mass Conservation Equation .....	148
Appendix C: Local Volume-Averaged Species Mass Conservation Equation .....	150
Appendix D: Saturation Development .....	151
Appendix E: Water Content Measurement by Neutron Imaging .....	153
Appendix F: Relationship between the Saturations $s_1$ and $s_2$ for Equal Pressure Drop .....	154
Appendix G: nk Coefficient Sensitivity Study (from 2 to 5) .....	156
Appendix H: Physical and Geometric Parameters .....	157
Appendix I: Through-Plane Diffusive and Convective Mass-Fluxes .....	159

## Nomenclature

### Acronym

1D	One-dimensional
1-F	One-Fluid
2D	Two-dimensional
2-F	Two-Fluid
3D	Three-dimensional
AFC	Alkaline Fuel Cell
BEV	Battery Electric Vehicles
BP	Bipolar Plate
CEA	Commissariat à l'énergie atomique et aux énergies alternatives
CFD	Computational Fluid Dynamics
CL	Catalyst Layer
CPU	Central Processing Unit
CW	Cooling Water
DC	Direct Current
DNS	Direct Numerical Simulation
DOE	Department of Energy
DOF	Degrees of Freedom
EO	Electro-Osmotic
EOD	Electro-Osmotic Drag
FC	Fuel Cell
FCS	Fuel Cell System
FEM	Finite Element Method
GC	Gas Channel
GDE	Gas Diffusion Electrode
GDL	Gas Diffusion Layer
GHG	GreenHouse Gas
HEM	Homogeneous Equilibrium Model
HFCEV	Hydrogen Fuel Cell Electric Vehicles
HOR	Hydrogen Oxydation Reaction

HT-PEMFC	High Temperature Proton Exchange Membrane Fuel Cell
ICEV	Internal Combustion Engine Vehicle
IEA	International Energy Agency
LBM	Lattice Boltzmann Method
L-M	Lockhart-Martinelli
LT-PEMFC	Low Temperature Proton Exchange Membrane Fuel Cell
M <sup>2</sup>	Multiphase Mixture
MCFC	Molten Carbonate Fuel Cell
MD	Molecular Dynamics
MEA	Membrane-Electrode Assembly
MPL	Micro-Porous Layer
MUMPS	MULTifrontal MASSively Parallel Sparse direct Solver
NEDC	New European Driving Cycles
NMR	Nuclear Magnetic Resonance
N-S	Navier-Stokes
ORR	Oxygen Reduction Reaction
P3D	Pseudo-3D
PAFC	Phosphoric Acid Fuel Cell
PARDISO	PARAllel sparse DIrect SOLver
PDE	Partial Differential Equations
PEM	Proton Exchange Membrane
PEMFC	Proton Exchange Membrane Fuel Cell
PFSA	PerFluorocarbon-Sulfonic Acid
PIF	Phase Indicator Function
PNM	Pore Network Modeling
PTFE	PolyTetraFluoroEthylene
QM	Quantum Mechanics
RAM	Random Access Memory
REV	Representative Elementary Volume
RH	Relative Humidity
RHS	Right-Hand Side
VOF	Volume of Fluid
WLTP	Worldwide harmonized Light duty driving Test Procedure
WRI	World Resources Institute

## Latin

$A$	Surface	$m^2$
$A_c$	Channel section	$m^2$
$a$	Water activity	–
$a_i$	Thermodynamics parameters (Nernst equation)	V, V/K
$a_{EO}$	Electro-osmotic drag coefficient	–
$C$	Parameter depending on the flow regime (according to L-M)	–
$c_f$	Molar concentration of sulfonate sites	$mol/m^3$
$d$	Pore diameter (or characteristic length of a pore)	m
$d_c$	Hydraulic diameter	m
$D$	Diffusion coefficient	$m^2/s$
$D_m$	Mass diffusion coefficient	$m^2/s$
$D_M$	Membrane water diffusivity	$m^2/s$
$E_{rev}$	Reversible potential	V
$e$	Thickness, component thickness	m
$\underline{e}_x$	Unit vector in the x direction (Cartesian coordinates)	–
$\underline{e}_y$	Unit vector in the y direction (Cartesian coordinates)	–
$\underline{e}_z$	Unit vector in the z direction (Cartesian coordinates)	–
$F$	Faraday constant	C/mol
$H_0$	Free enthalpy	J/mol
$h$	Mesh element size	m
$g$	Gravitational acceleration vector	$m/s^2$
$I$	Identity tensor	–
$i$	Current density	$A/m^2$
	Intensity (Lambert-Beer law)	cd
$i_0$	Intensity of the dry cell image (Lambert-Beer law)	cd
$j$	Diffusive flux	$kg/(m^2 \cdot s)$
$J(s)$	Leverett J-function (saturation dependent)	–
$J_{conv}^+ J_{conv}^-$	Convective mass-fluxes across the layers (P3D)	$kg/(m^2 \cdot s)$
$J_{diff}$	Diffusive flux through the membrane	$kg/(m^2 \cdot s)$
$J_{diff}^+ J_{diff}^-$	Diffusive mass-fluxes across the layers (P3D)	$kg/(m^2 \cdot s)$
$J_{EO}$	Water electro-osmotic drag	$kg/(m^2 \cdot s)$

K	Absolute permeability	$m^2$
$K_2$	Forchheimer correction tensor	–
$K_{rk}$	Relative permeability of the k-phase	–
l	Characteristic length of the REV	m
L	System dimension	m
M	Mass molar	kg/mol
$\dot{m}$	Mass flow rate	kg/s
N	Number	–
n	Bruggeman factor	–
$n_f$	Unit vector perpendicular to $A_{sf}$	–
$n_k$	Unit vector perpendicular to $A_{Ik}$	–
	Key parameter in the two-phase flow modeling	–
P p	Pressure	Pa
$Q_T$	Joule effect	W/m <sup>2</sup>
R	Universal gas constant	J/(mol·K)
	Cell internal resistance	$\Omega$
r	Mass source induced by the electrochemical reaction	kg/(m <sup>3</sup> ·s)
S	Mass source term	kg/(m <sup>3</sup> ·s)
	Liquid-gas velocity ratio	–
$S_0$	Free entropy	J/(mol·K)
$S^{Ik}$	Mass source term at the k-phase interface	kg/(m <sup>3</sup> ·s)
$S^{sf}$	Mass source term at the solid-fluid interface	kg/(m <sup>3</sup> ·s)
s	Liquid saturation, saturation, liquid volume fraction	–
T	Stress tensor	N/m <sup>2</sup>
	Temperature	K <u>or</u> °C
t	Water thickness (Lambert-Beer Law)	m
	Time	s
u	Velocity in the x direction (Cartesian coordinates)	m/s
$U_{cell}$	Uniform cell potential	V
V	Volume, total volume	m <sup>3</sup>
$\underline{V}$	Velocity vector	m/s
$\underline{V}_I$	Microscopic velocity vector of the k-phase interface	m/s
$\underline{V}_r$	Mean velocity vector weighted by the phase change	m/s

$v$	Velocity in the y direction (Cartesian coordinates)	m/s
$w$	Velocity in the z direction (Cartesian coordinates)	m/s
$x$	Gas quality	–
$X$	Martinelli parameter	–
$Y$	Mass fraction	–

### Greek

$\alpha$	Volume fraction	–
$\beta$	Empirical coefficient	V, V/K
$\Gamma^{lk}$	Mass transfer due to phase change	kg/(m <sup>3</sup> .s)
$\Delta H_0$	Enthalpy of reaction	J/mol
$\delta_l$	Dirac (delta) generalized function	–
$\varepsilon$	Porosity	–
$\eta$	Overpotential (activation and diffusion)	V
$\eta_{ohm}$	Ohmic losses	V
$\theta$	Contact angle	°
$\lambda$	Water content	–
$\lambda_M$	Electrolyte membrane water content	–
$\mu$	Dynamic viscosity	Pa.s
$\rho$	Density	kg/m <sup>3</sup>
$\sigma$	Electrical <u>or</u> proton conductivity	S/m
	Liquid water/air surface tension	N/m
$\tau$	Viscous stress tensor	N/m <sup>2</sup>
	Tortuosity	–
$\phi_g$	Empirical two-phase multiplier (according to L-M)	–
$\chi$	Phase Indicator Function (PIF)	–
$\psi$	Quantity	–

## Operator

$\langle \rangle$	Ensemble averaging operator
$\langle \rangle_f$	Fluid volume-average (local intrinsic-average associated with the fluid-phase)
$\langle \rangle_k$	k-phase volume-average (local intrinsic-average associated with the k-phase)
$\overline{\phantom{x}}$	Favre (or mass weighted) averaging operator
$\overline{\phantom{x}}_f$	Favre (or mass weighted) averaging operator associated to the fluid volume
$\overline{\phantom{x}}_k$	Favre (or mass weighted) averaging operator associated to the k-phase volume
$\nabla \cdot$	Divergence
$\nabla$	Gradient
$\nabla^T$	Transpose gradient
$\frac{\partial}{\partial t}$	Time derivative

## Superscripts

"	Fluctuating part
eff	Effective
lk	Phase interface (between the k-phase and the other fluid phase as well as the solid matrix)
sf	Solid-fluid interface

## Subscripts

vap <sub>c</sub>	Condensed water vapor
c	Capillary, contact
cell	Cell
Chi	Chisholm
comp	Component
e	Electronic
f	Fluid, fluid-phase
g	Gas, gas phase
H <sub>2</sub>	Dihydrogen

H <sub>2</sub> O	Water
lk	Phase interface (between the k-phase and the other fluid phase as well as the solid matrix)
j	Specie
jf	j-specie in the fluid-phase
jk	j-specie in the k-phase
k	Liquid or gas phase, phase ( $\neq$ solid)
l	Liquid, liquid-phase
M	Membrane
nw	Non-wetting phase
O <sub>2</sub>	Dioxygen
p	Protonic
s	Solid
sat	Saturation value
sf	Solid-fluid interface
T	Total, thermal
v	Vapor
w	Wetting phase, water

### Prefix

a	Anode
c	Cathode

## General Introduction

Global warming is currently one of the major concerns with a world temperature increase of 1.1°C since the beginning of the last century. The climate change is largely caused by human activity and in particular by the transport sector, which emits a large amount of greenhouse gases. The transition to a green mobility seems to be well integrated by a majority of the population and governments. Electric cars are designed for an emission-free mode of transport as long as electricity is not produced in a polluting manner. However, electricity cannot be stored and its direct use through battery-powered vehicles reaches some limits in terms of autonomy and recharging time.

Hydrogen today appears to be a viable solution in the storage of electrical energy from a CO<sub>2</sub>-free source. The green hydrogen, produced notably by electrolysis, can be used as a clean fuel via fuel cells. Among the technologies envisaged, the Proton Exchange Membrane Fuel Cell (PEMFC) is the best solution to automotive application due to its excellent dynamic, high power density and good electrical efficiency especially thanks to its solid electrolyte. PEM fuel cells convert hydrogen into electrical energy when it reacts with oxygen to power a vehicle via an electric motor while only water and heat are emitted during the process. Despite a simple operating principle, the fuel cell is made-up of several key components that are closely interdependent to achieve optimal operation. Among them, the membrane, electrodes and gas diffusion layers forming the Membrane–Electrode Assembly (MEA) considered as the heart of the cell must ensure to well-defined mechanical and structural characteristics. Although promising, PEM fuel cells face some challenges in order to be large scale commercialized. The durability today appears to be the main issue to be solved. Indeed, degradations, which can be irreversible, are at the origin of the limited lifespan of PEM fuel cells. These degradations occur notably during a no-proper management of water and temperature.

A growing need to better understand the mechanisms of water transport and phase change has been addressed by the scientific community. Accordingly, many numerical models have been proposed in recent years, in particular to represent the multiphase flow. Several modeling approaches in different layers in PEM fuel cells and at different scales were developed for decades to study the transport phenomena.

This manuscript is mainly dedicated, through four chapters and an appendix, to the investigation of liquid water heterogeneities in large area PEM fuel cells by using a two-phase flow multiphysics model. The first chapter establishes the background of the study by describing the challenges of electric mobility. The various components of a PEM fuel cell are also presented in detail as well as its working principle. Further, the water transport mechanisms are identified as well as their impact on the durability and performance of the fuel cell. Finally, a non-exhaustive state of the art of two-phase flow models was presented at the end of the chapter.

The complex theory of the conservation equations governing the transport phenomena in PEM fuel cell are explained in Chapter II. They are described for a single-phase and two-phase flow from the local and instantaneous equations. They are then averaged to obtain the macroscopic equations namely mass, species, momentum and energy balance applied to a porous medium. All the definitions and mathematical tools used in the local volume-averaging method over the Representative Elementary Volume (REV) are detailed in this chapter.

In Chapter III, a one-fluid model, developed in a previous work [37], is improved and used in order to quantify and locate the liquid water in a large area fuel cell. This continuum mechanics model is implemented in a computational software with a Finite Element Method (FEM) resolution. The equations, detailed in Chapter II for a one-phase flow, are discretized in the model according to their pseudo-3D formulation. After validation by comparison of the numerical results with neutron imaging tests under low power operating (humid) conditions, the model is able to provide helpful temperature, water content, current density, etc. maps at the stack scale but also in the different layers of a cell. Finally, a sensitivity analysis was performed on key coefficients in the water transport mechanisms.

In the last chapter, a two-fluid model, also called Euler–Euler model, based on the description of the conservation equations for each phase is developed to simulate a high power operation in an automotive application. Indeed, the one-fluid model reaches some limits when dry conditions are simulated. The two-fluid model is validated by comparison with experimental tests obtained with neutron imaging. In such conditions, this latter model predicts a better description of the two-phase flow in PEM fuel cells compared to the one-fluid model. Accordingly, the water management is examined by exploiting the numerical results to finally analyze the distribution of liquid water at the stack and component scales.

**Chapter I**  
**STATE OF THE ART**

## Introduction

In the first chapter, the challenges around green mobility are briefly reviewed by introducing the hydrogen vector as a major asset in the decarbonation of the transport sector via Proton Exchange Membrane (PEM) fuel cell vehicles. The PEM operating principle is detailed as well as all the components constituting a cell. In addition, the main targets around PEM fuel cells to achieve a sufficient technology maturity are quickly discussed. Afterward, the mechanisms of water transport within a cell are presented in detail. Indeed, water management remains a complex issue to solve in order to optimize performance and limit degradation of the fuel cell. Finally, a non-exhaustive state of the art of PEM fuel cell modeling is introduced with a focus on two-phase flow models.

### 1. Mobility

The transport sector mainly contributes to global Greenhouse Gas (GHG) emissions – about 14% of annual emissions (including non-CO<sub>2</sub> gases) and around a quarter of CO<sub>2</sub> emissions according to the World Resources Institute [1] from burning fossil fuels (also confirmed by 2016 data from the International Energy Agency [2]). In France, it is the most important source of GHG emissions (31%) (Fig. I-1), ahead of emissions produced by buildings, agriculture or industry [3]. Among transportation, road travel represents 90% of emissions, mostly with cars, used by 72% of French people daily, followed by trucks and commercial vehicles [3]. It is expected in the coming years that the transport sector will become more and more prominent compared to other sectors due to a growing demand for human mobility and freight transport [1]. Mobility is therefore at the heart of the ecological transition in order to adopt a sustainable development model. The societal mentality is changing regarding transport, particularly road travel, with a desire to reduce its impact on the environment (car sharing, public transport, etc.). Government policies have also played a role in promoting the purchase of clean vehicles through financial bonuses or by regulating vehicle emissions. In this direction, the European Commission proposes in its green deal entitled *Fit for 55* to reduce CO<sub>2</sub> emissions from new cars by 55% by 2030 and to zero emission by 2035 [4].

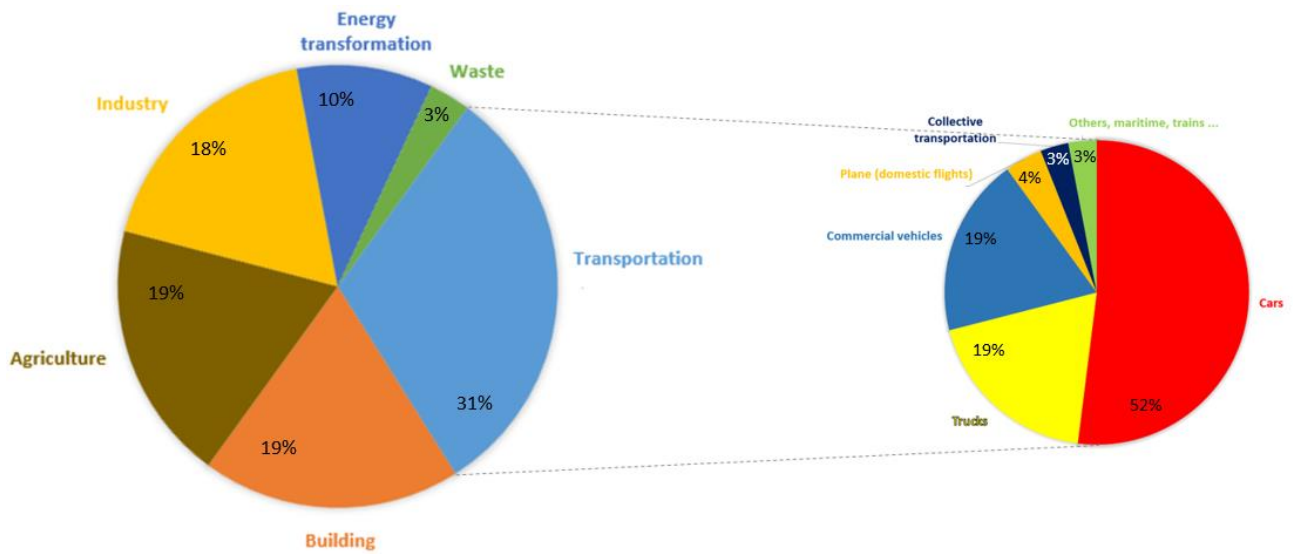


Fig. I-1. Greenhouse gas emissions by sector in France – data from June 2019 Report [3].

## 2. PEM Fuel Cell Electric Vehicles

Fuel cell vehicles appear to be serious candidates in order to decarbonize the transport sector. They are electrically powered by converting chemical energy stored by fuel, usually hydrogen, into electricity via a fuel cell as the name suggests. Among the different fuel cell technologies, the Proton Exchange Membrane Fuel Cell (PEMFC) appears to be the most appropriate technology for automotive application due to its excellent dynamic, high power density, good electrical efficiency (~ 60–65%) [5] and solid polymer electrolyte. PEM fuel cells can be mainly distinguished in two different technologies according to the operating temperature: Low Temperature (LT-PEMFC) from 60 to 95°C and High Temperature (HT-PEMFC) from 120 to 180°C. This work is exclusively focused on LT-PEMFC, only called PEMFC in the rest of the document.

### 2.1 Hydrogen for Mobility

As discussed before, in order to reduce GHG emissions, electric mobility is at the top of the list in the ecological transition of the transport sector if the electricity is produced in a renewable way (wind, hydro, solar, biomass, etc.). However, despite recent progress, electrical energy is reaching its limits in its direct use through batteries. Indeed, the electricity storage with batteries

is challenging for the automotive application due to its volume, weight and recharge time. For example, the batteries of the Renault Zoé<sup>1</sup> R110 have a weight of 326 kg for a total weight of 1.5 t. They are recharged in 6h 55min (using a specific domestic plug called *Wallbox* - 7.4 kW) to achieve a maximum range of 395 km according to the WLTP<sup>2</sup> cycle. However, the vehicle autonomy on the motorway (120-130 km/h) drops by around 40% compared to the WLTP cycle [6]. Therefore, the Hydrogen Fuel Cell Electric Vehicles (HFCEVs) appears to be an alternative to battery-powered vehicles and more suitable for the automotive cycle: driving range → mass → consumption according to Van De Kaa et al. [7] and Bethoux [8]. Indeed, HFCEVs have an average range of 500 km up to 1000<sup>3</sup> km (close to the range of a conventional car) despite a lower system efficiency than Battery Electric Vehicles (BEVs) due to the high energy density per kg of hydrogen (33.3 kWh/kg), around 3.7 times more than gasoline and 4.5 than ethanol. The other significant advantage of HFCEVs is the refueling time (~ 3–5 min) corresponding to that of an Internal Combustion Engine Vehicle (ICEV).

The use of “green”<sup>4</sup> hydrogen, produced mainly by water electrolysis<sup>5</sup> from renewable electricity, is essential for the development of sustainable mobility without GHG emissions. Green hydrogen is then becoming a high potential energy carrier, which can deliver or store a tremendous amount of renewable energy. In addition, green hydrogen allows the flexibility and stability of the electricity network by storing intermittent production (solar, wind). The hydrogen is pressurized (typically at 350 bars up to 700 bars) and stored in tanks to be converted back into electricity through a PEM fuel cell to power the electric motor of a HFCEV. However, considering the overall energy efficiency, i.e. from the electricity production to its use, a battery-powered vehicle directly using electricity is more efficient than a PEMFC vehicle (Fig. I-2).

---

<sup>1</sup> Renault Zoé: the best-selling electric vehicle from 2016 to 2020 in France according to [9].

<sup>2</sup> WLTP: the World harmonized Light-duty vehicles Test Procedure is a global harmonized standard reproducing realistically the average use of a vehicle. It replaces the previous New European Driving Cycle (NEDC) as the European vehicle homologation procedure.

<sup>3</sup> The new Toyota Mirai, a hydrogen-powered vehicle, covered more than 1,000 km with a single charge in real driving conditions in May 2021 in France, which corresponds to a new autonomy record for a fuel cell vehicle [10].

<sup>4</sup> The European Commission has not yet harmonized hydrogen terminologies (by color).

<sup>5</sup> Electrolysis of water is the process of using electricity to decompose water into oxygen and hydrogen gas. Its production cost is estimated at 6 €/kg. Note that hydrogen production is currently dominated by the methane steam reforming (96%) due to an economical process (1.5 €/kg) but associated with a very significant CO<sub>2</sub> emission [<https://www.connaissancedesenergies.org/fiche-pedagogique/production-de-lhydrogene>]. In addition, substantial sources of natural hydrogen have recently been discovered [11]–[12]. The feasibility of exploiting such sources is studied [13].

Finally, the current chicken and egg situation regarding hydrogen as fuel, namely to produce hydrogen vehicles or build hydrogen stations, is evolving. Indeed, many hydrogen plans have been adopted around the world and in Europe, as Germany (9 b€) and France (7.2 b€), by investing in production or distribution structures encouraging car manufacturers to develop hydrogen vehicles.

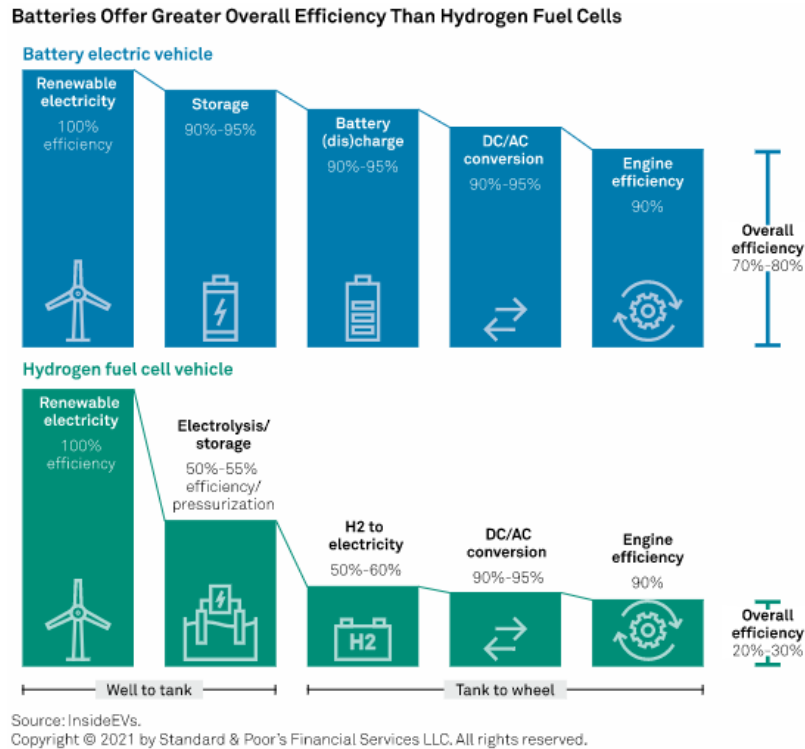
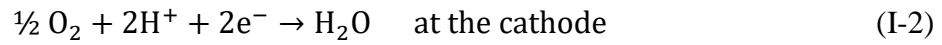
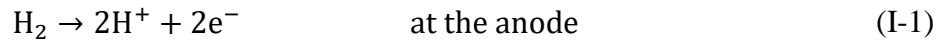


Fig. I-2. Overall energy efficiency for BEV (blue) and HFCV (green) [14].

## 2.2 Operating Principle of a PEM Fuel Cell

PEM fuel cells convert the chemical energy of hydrogen into electrical energy (Fig. I-3). Pure hydrogen is generally supplied to the anode in contrast to oxygen fed to the cathode. Indeed, ambient air contains enough oxygen to be used as such by the fuel cell. Unlike a battery, which is an electrical storage system, the fuel cell requires a constant supply of fuel (hydrogen) and oxidant (oxygen) to provide electricity. The electrochemical reactions occur simultaneously at the interface of the electrodes and electrolyte both at the anode (oxidation of hydrogen) and at the cathode (reduction of oxygen). The PEM fuel cell reactions are written as follows:



Hydrogen Oxidation Reaction (HOR) releases electrons to provide electricity via the external circuit and protons, which are transported through the membrane to reach the cathode where they react with the oxygen and electrons thus producing water. As an exothermic process, significant heat is produced during the combustion of hydrogen. The heat source is detailed in Chapter III.

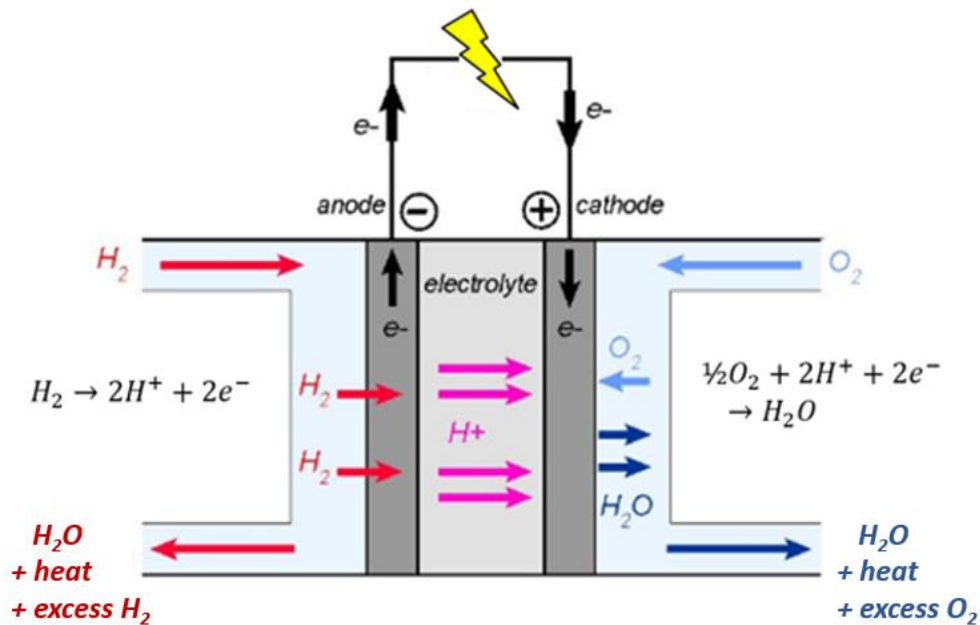


Fig. I-3. Schematic of the PEMFC working principle.

### 2.3 PEM Fuel Cell Components

Each cell is an assembly of several layers, each playing a specific role in the cell operation. Optimal functioning is only achieved if all the interactions between these layers operate correctly. Indeed, it is necessary to sufficiently and uniformly supply the reactive sites with gas, to collect the current while removing the water and heat produced during the Oxygen Reduction

Reaction (ORR).

### 2.3.1 Membrane

The membrane has a crucial role in PEM fuel cells as a solid electrolyte (unlike other types of fuel cell with liquid electrolyte: alkaline (AFC), molten carbonate (MCFC) and phosphoric acid (PAFC) fuel cells). Some properties are required to operate properly:

- Its proton conductivity must be high in order to limit voltage losses due to its internal resistance. The ionomer conductivity is closely related to the water content in the membrane (this point is discussed in more detail in Chapter III-3.2.3).
- Its electronic conductivity must be as low as possible to avoid short circuits and current losses.
- The membrane must be impermeable to gas to avoid any mixing. Indeed, the permeation of hydrogen towards the cathode generates a so-called permeation current, decreasing the performance of the fuel cell.
- The membrane must have good chemical, mechanical and thermal resistance for a sufficient life in operation.
- The membrane must be both resistant and flexible to allow the use of thin membrane.

Materials composed of perfluorinated macromolecules, typically PerFluorocarbon-Sulfonic Acid (PFSA), best correspond to the required membrane qualities. PFSA structure includes acid functions allowing the transport of protons during the dissociation of the  $\text{SO}^3\text{-H}^+$  acid group in the presence of water. The proton exchange membrane must therefore be correctly hydrated to have a good proton conductivity. Nafion® (Fig. I-4) developed and marketed by DuPont™ is historically one of the most widely used polymer in PEM fuel cells that largely fulfills the required specifications. Its cost relatively decreased these last years, to reach several tens €/m<sup>2</sup> for large quantities. Similar materials have been developed such as Fumapem® (Fumatech™), Flemion® (Asahi Glass™), Aciplex® (Asahi Chemical™), etc. For automotive application, the membrane thickness ranges generally between 8 and 50 µm depending on the manufacturing process. Indeed, porous PolyTetraFluoroEthylene (PTFE) films are generally used as support material to manufacture composite membrane in order to increase its mechanical stability and to reduce its thickness.

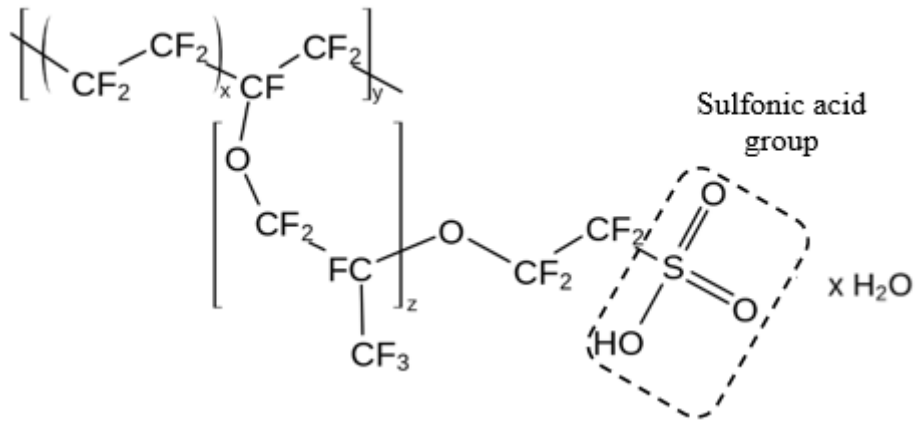


Fig. I-4. Chemical structure of Nafion®.

### 2.3.2 Catalyst Layer

A thin though volumetric Catalyst Layer (CL) is usually pressed on the membrane where the electrochemical reactions take place (on the catalytic surface). As the name suggests, the catalytic layer contains a catalyst to accelerate reactions. The most widely used in PEM fuel cells is platinum at both the anode and cathode. It is deposited in the form of nanoparticles dispersed on carbon particles. Due to its high cost (around 28,000 €/kg, September 2021 data from [15]), many studies have been carried out to minimize its loading [16], to find an efficient platinum alloy (Pt-Ni, Pt-Cr, Pt-Co) [17] or to replace it by a non-precious catalyst [18]. Outside allowing electrochemical reaction, the catalyst layer has also to transport electron, protons and gases. Therefore, it is usually a porous media composed of carbon/platinum and ionomer. Catalyst layers have a small thickness (5–10  $\mu\text{m}$ ) in order to limit potential losses due to the transport of protons and gas diffusion. Their porosity is of the order of 50%.

### 2.3.3 Gas Diffusion Layer and Micro-Porous Layer

Gas Diffusion Layers (GDLs) are designed to supply, as the name suggests, the catalytic layers with sufficient gas from the channels. These layers also perform important other functions to:

- evacuate the production of liquid water and heat from the catalytic layers to channels
- electrically connect the catalytic layers with the bipolar plates
- mechanically support the catalyst layers and membrane

For these reasons, the gas diffusion layers must require some properties:

- to be sufficiently porous ( $\sim 70\text{--}80\%$ )
- to be electrically and thermally conductive
- to be rigid enough

The GDL materials used are generally composed of carbon cloth (Fig. I-5a) (E-TEK®, ELAT®, GDL-CT®) or carbon paper fibers (Fig. I-5b) (AvCarb®, Sigracet®, Toray®, SpectraCarb®, Zoltek®). GDLs are generally treated [19], typically with PTFE (PTFE loadings from 5% to 30%), to become hydrophobic in order to avoid flooding. Some authors have studied the fuel cell performance for different PTFE loadings. For instance, Chen et al [20] obtained an optimum power density of the cell with a PTFE loading of 10%.

In addition, a Micro-Porous Layer (MPL) (porosity  $\sim 35\%$ ) can be added between the catalytic and gas diffusion layers to minimize the contact resistance and improve water management [21]-[22]. MPLs are relatively thin (around  $50\ \mu\text{m}$ ) and GDLs have a few hundred micrometers thickness.

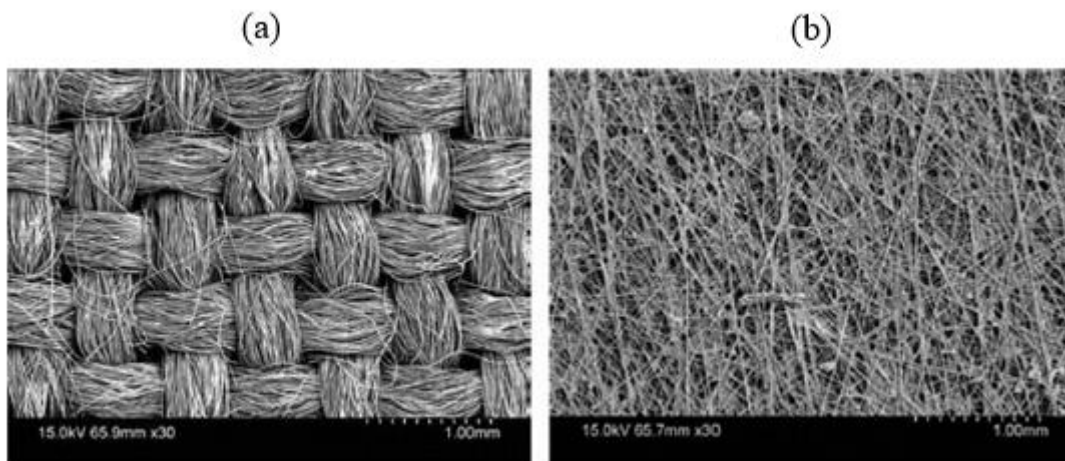


Fig. I-5. SEM micrographs of (a) the E-TEK® EC-CC1-060 carbon cloth and (b) the Toray® TGP-H-090 5% wet-proof PTL carbon paper [23].

### 2.3.4 Membrane-Electrode Assembly

A Gas Diffusion Electrode (GDE) is composed of one catalyst layer, one (possible) microporous layer and one gas diffusion layer. A membrane sandwiched between the anode and cathode GDEs form the Membrane-Electrode Assembly (MEA) considered the core component of the cell. Fig. I-6 represents a membrane-electrode assembly structure and proton, electron and gas transport in a  $H_2/O_2$  PEMFC [24].

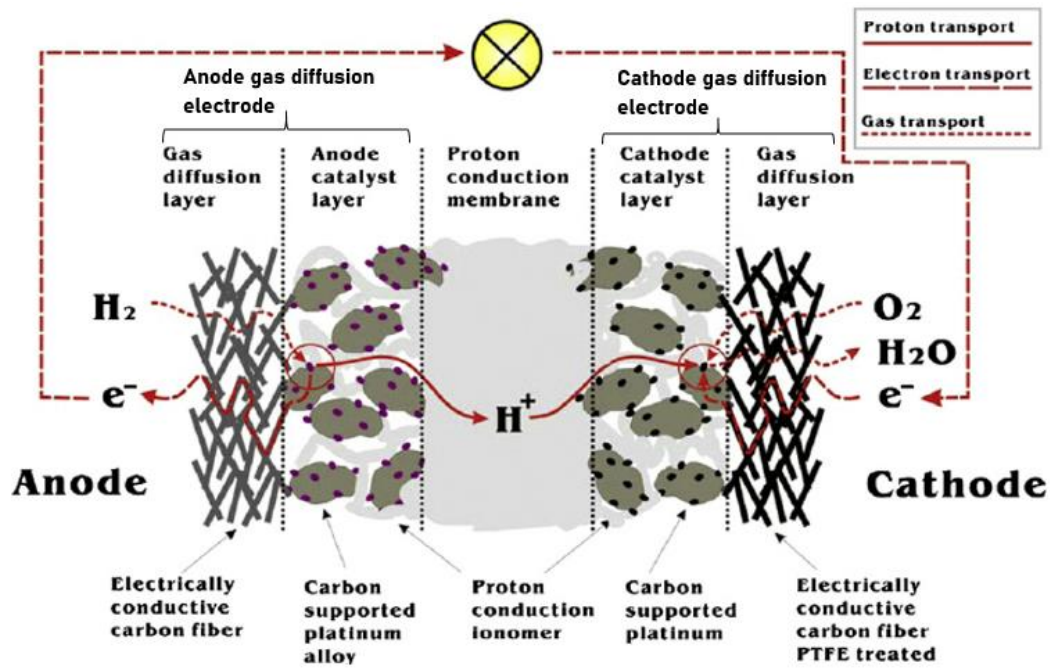


Fig. I-6. Membrane-electrode assembly structure and proton, electron and gas transport in a  $H_2/O_2$  PEMFC [24].

### 2.3.5 Bipolar Plates

Each MEA is surrounded by plates that uniformly distribute the reactants through Gas Channels (GCs) to the anode and cathode. Each cell is connected to the adjacent one via an assembled plates, so called Bipolar Plate (BP), which therefore ensure the distribution of hydrogen to one cell and oxygen to the adjacent cell. Bipolar plates must:

- be electrically conductive to connect the cells
- be thermally conductive to remove the heat produced from active areas via a cooling circuit often formed inside the bipolar plate
- be impermeable to gases to separate the adjacent cells

- be robust while being as light as possible to minimize weight
- be corrosion resistant.

Different designs of flow-field have been studied with square, rectangular or trapezoidal sections, counter-current or co-current hydrogen and air flows, etc. The dimensions of the section of the GCs are relatively small; rarely exceeding 1 mm. Fig. I-7 shows several flow-field designs such as serpentine, parallel or interdigitated. Other configurations are nature inspired (biomimicry) [25] based on the structure of a leaf for example. Another important characteristic of bipolar plates is the material used. Graphite/composite and metallic materials are the most common. Each has advantages and drawbacks (corrosion and stress resistance, chemical stability, manufacturing process, etc.) [26]-[28]. Recently, CEA researchers have developed a new method for printing bipolar plates based on a carbon ink allowing continuous production, thereby reducing cost and offering power densities similar to those of metal bipolar plates [29].

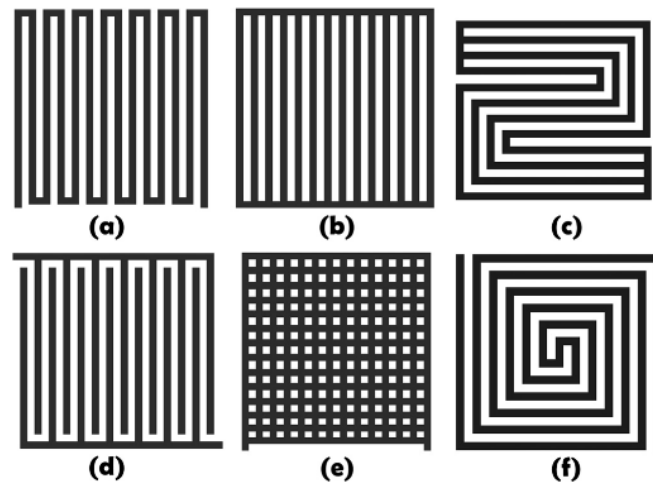


Fig. I-7. Schematic of various flow field designs: (a) Serpentine, (b) parallel, (c) parallel-serpentine, (d) interdigitated, (e) mesh (grid, superparallel) and (f) spiral-serpentine [25].

## 2.4 PEM Fuel Cell System

One membrane-electrode assembly and one bipolar plate (which can be split into two monopolar plates) form a single cell. Each cell delivers typically a voltage between 0.6 and 0.8 V under operation depending on the operating conditions. It is then necessary to pack several cells in series forming a stack to deliver the desired voltage of several hundred volts for automotive



## 2.5 Technical Targets for Fuel Cell Systems for Transportation Applications

Despite growing interest in hydrogen, PEM fuel cell electric vehicles represent a minority of the vehicle market with only 162 registrations for passenger cars in France in 2020 [39]. Some improvements are still necessary to reach a sufficient maturity of the PEMFC technology allowing a mass production and a large scale commercialization. The U.S. Department of Energy (DOE) regularly reports on component/FCS performance and cost targets in PEM fuel cells for the transportation application [40]. Fig. I-10 presents the current FCS status and its future objectives. The FCS energy efficiency has already reached its target set for 2025, in contrast to the price of the system, which is on the way to reach it, even more if a larger scale commercialization is launched. The specific power seems limited especially due to the weight of the bipolar plates (most often made of metallic materials). The system durability is currently the most significant issue in PEM fuel cells because of (irreversible) degradation caused notably by a no-proper management of water and temperature in the fuel cell. This point is discussed in the next section.

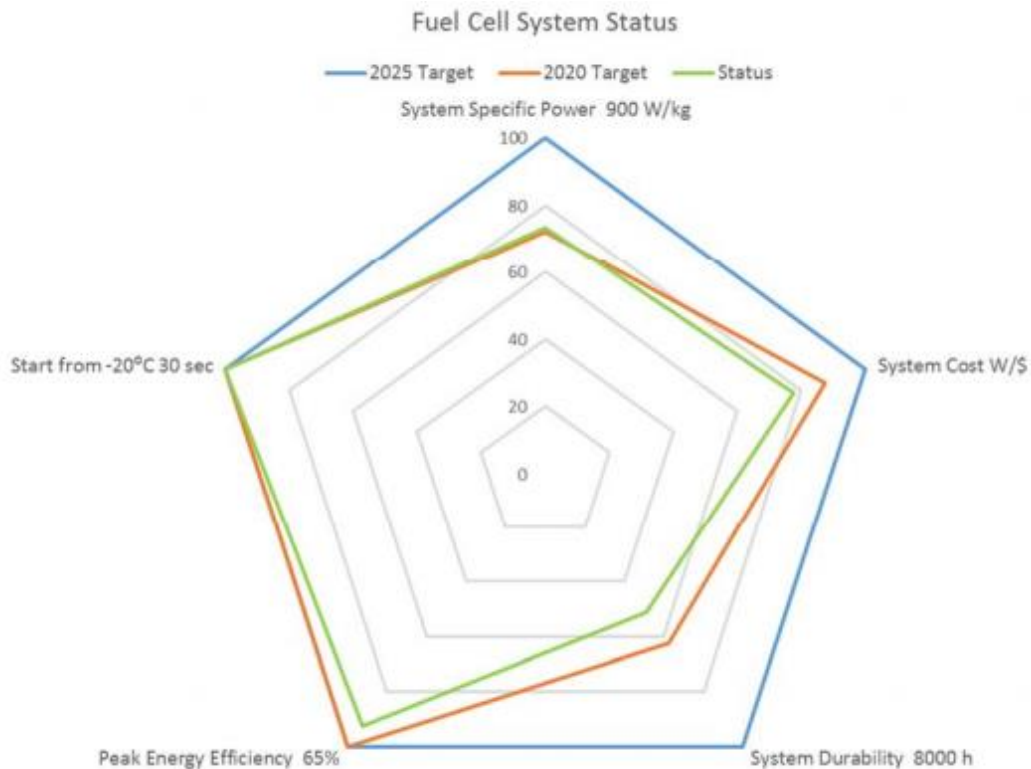


Fig. I-10. Fuel Cell System Status (2017) versus Targets (The green line indicates the status as a fraction of the targets) [40].

### 3. Water Management in PEM Fuel Cells

Water management is one of the biggest challenges in the development and commercialization of PEM fuel cells. Indeed, a proper water management in PEM fuel cells is necessary to optimize their performance and increase their lifespan. Water is present in all the layers of the cell because of:

- pre-humidification (sometimes up to saturation) of the inlet gases to ensure good proton conductivity of the membrane
- water production during the oxygen reduction reaction at the cathode
- water transport mechanisms (discussed in the next section).

Water phase change and transport mechanisms are presented in this section as well as the impact of water on the performance and degradation of the cell.

#### 3.1 Condensation and Evaporation

Water can either be present in liquid or vapor form. Condensation occurs only when the gas becomes entirely saturated with water vapor during a decrease of the local temperature (in contact with the cooling circuit for example), the reactant gas consumption or water vapor accumulation (due to its ORR production and transport between layers). In other words, gas relative humidity locally reaches 100%, causing condensation. Evaporation occurs when liquid water and unsaturated gas are both present. The gas relative humidity can decrease below 100% if there is either a diminution of the local pressure or an augmentation of the local temperature.

#### 3.2 Water Management Mechanisms

##### 3.2.1 Water Transport through the Membrane

Water is transported through the membrane by two main phenomena: Electro-Osmotic Drag (EOD) and diffusion. The hydraulic permeation is generally negligible compared to the two phenomena mentioned. Electro-osmotic drag is the motion of liquid water induced by an applied potential across the membrane. Therefore, water molecules are exclusively dragged from the anode to cathode due to the current-carrier protons. EOD is usually formulated according to the protonic flux and water content as follows:

$$J_{EO} = \frac{a_{EO} M_{H_2O}}{F} i \quad (I-4)$$

where  $a_{EO}$  is the EOD coefficient, which depends exclusively on the membrane water content  $\lambda_M$  defined as the averaged number of water molecules per sulfonic acid group. The EOD coefficient has been the subject of numerous studies by experimental tests or mathematical modeling. Different formulations can be found in the literature. Springer et al. [41] proposed a linear relation; Hwang et al. [42] and Meier et al. [43] considered a quadratic evolution while Zawodzinski et al. [44] supposed a discontinuous relation. Peng et al. [45] developed a new method based on hydrogen pump to measure the electro-osmotic drag coefficient in representative PEMFC operating conditions. More recently, Xu et al. [46] experimentally study the EO drag coefficients in Nafion® membrane in acid, sodium and potassium forms by electrophoresis NMR. New correlations of the electro-osmotic drag coefficient according to the water content can be extracted from their work. Table I-1 lists several EO drag coefficient laws, which are plotted against the water content in Fig. I-11. A sensitivity analysis is performed with the one-fluid model in Chapter III.

**Table I-1**

Electro-osmotic drag coefficients.

Author(s)	Expression	
Springer et al. [41]	$a_{EO} = \frac{2.5 \lambda_M}{22}$	(I-5)
Hwang et al. [42]	$a_{EO} = -3.4 \cdot 10^{-19} + 0.05 \lambda_M + 0.0029 \lambda_M^2$	(I-6)
Meier et al. [43]	$a_{EO} = 1 + 0.028 \lambda_M + 0.0026 \lambda_M^2$	(I-7)
Zawodzinski et al. [44]	$a_{EO} = \begin{cases} 1 & \text{if } \lambda_M \leq 14 \\ 0.1875 \lambda_M - 1.625 & \text{if } \lambda_M > 14 \end{cases}$	(I-8)

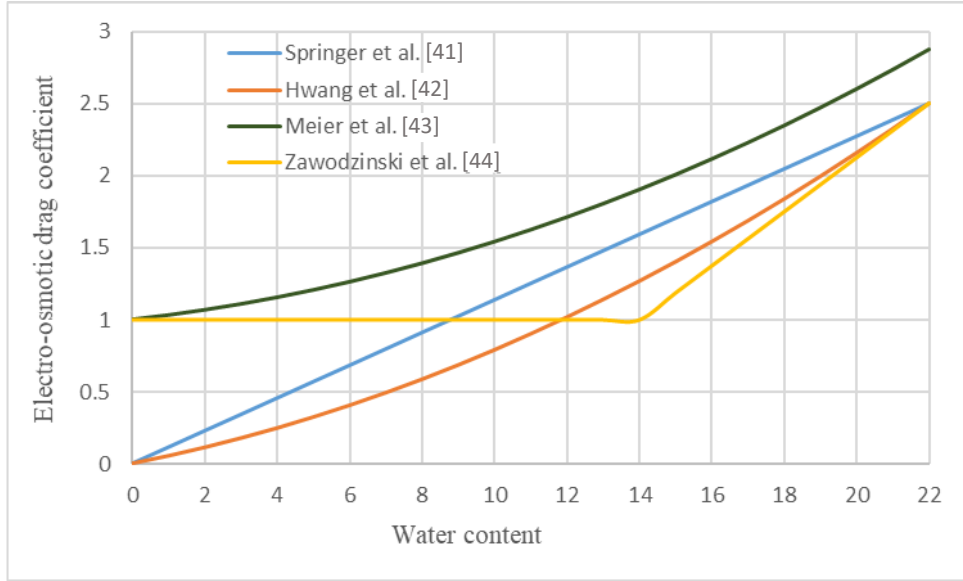


Fig. I-11. Electro-osmotic drag coefficients from Table I-1 versus water content.

Water diffusion is induced by the water concentration gradient between the cathode and anode. It drives water from high concentration areas to lower concentration areas. Diffusion can take place on both directions even if it mainly drags water from the cathode to anode. Indeed, the ORR production and electro-osmotic drag accumulate water at the cathode side. This phenomenon is then called back diffusion from the cathode side toward the anode one, which is necessary for a good hydration of the membrane on the anode side. A Fick's law is generally considered in order to describe the diffusive flux density by:

$$J_{\text{diff}} = D_M \frac{M_{\text{H}_2\text{O}}}{e_M} c_f (\lambda_{\text{aCL}} - \lambda_{\text{cCL}}) \quad (\text{I-9})$$

where  $D_M$  is the membrane water diffusivity,  $e_M$ , the membrane thickness,  $c_f$ , the molar concentration of sulfonate sites in Nafion®,  $\lambda_{\text{aCL}}$  and  $\lambda_{\text{cCL}}$ , the water contents at the interfaces between the membrane and anode/cathode catalyst layer pores, respectively. Springer's law [41] formulates the water content only depending on the water activity  $a$ :

$$\lambda(a) = \begin{cases} 0.043 + 17.81a - 39.85a^2 + 36^3 & \text{if } a \leq 1 \\ 14 + 1.4(a - 1) & \text{if } a > 1 \end{cases} \quad (\text{I-10})$$

where  $a$  difference in water uptake in contact with liquid (hypothetically represented by  $a > 1$ ) or saturated vapor ( $a \leq 1$ ) was observed by Schroeder [47]. A linear extrapolation is used in

both models (presented in Chapter III and IV) to avoid numerical instability caused by the water content discontinuity formulation in Eq. (I-10). Many authors have proposed correlation for the water diffusivity through the membrane. Table I-2 references some diffusivity formulations from Fuller [48], Zawodzinski et al. [49] and Motupally et al. [50], which are plotted against the water content in Fig. I-12. Similarly to the EOD coefficient, a sensitivity analysis of the water diffusivity correlation is presented in Chapter III.

**Table I-2**

Diffusion coefficients.

Author(s)	Expression	
Fuller [48]	$D_m = 2.1 \cdot 10^{-7} \lambda_M \cdot \exp\left(-\frac{2436}{T}\right)$	(I-11)
Zawodzinski et al. [49]	$D_m = (6.707 \cdot 10^{-8} \lambda_M + 6.387 \cdot 10^{-7}) \cdot \exp\left(-\frac{2416}{T}\right)$	(I-12)
Motupally et al. [50]	$D_m = \begin{cases} 3.1 \cdot 10^{-7} \lambda_M [\exp(0.28 \lambda_M) - 1] \cdot \exp\left(-\frac{2346}{T}\right) & \text{if } 0 \leq \lambda_M \leq 3 \\ 4.17 \cdot 10^{-8} \lambda_M [1 + 161 \cdot \exp(-\lambda_M)] \cdot \exp\left(-\frac{2346}{T}\right) & \text{if } 3 \leq \lambda_M \leq 17 \end{cases}$	(I-13)

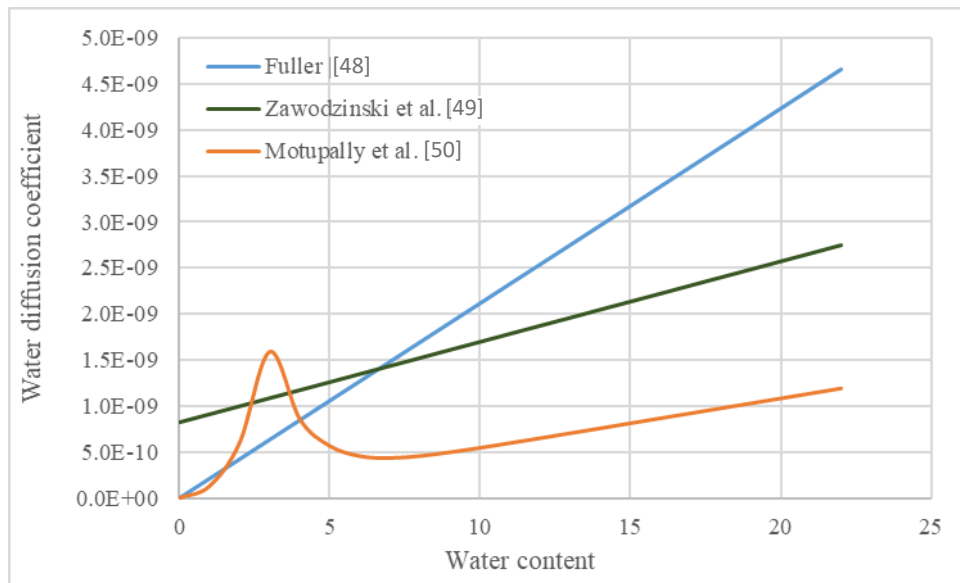


Fig. I-12. Water diffusion coefficients from Table I-2 versus water content.

### 3.2.2 Capillarity in Porous Layers

Liquid water transport results from the liquid pressure gradient, which is strongly influenced by interfacial tensions in porous media. This is called capillarity or capillary force originating from two distinct interaction phenomena on a microscopic scale. On the one hand, there is the interfacial tension between the liquid and gas, called surface tension, where the interface behaves like a membrane under tension. It depends mostly of the property of the liquid phase for a liquid–gas flow. On the other hand, there is the interfacial tension between the fluids and solid matrix, called wettability. Fluid/solid interfaces form a characteristic angle named contact angle (Fig. I-13) when the tensions are in equilibrium. This angle is measured by convention from the densest fluid, that is to say the liquid water in PEMFCs. It reflects the affinity of fluids and particularly of the liquid water with the solid matrix. If the contact angle is less than  $90^\circ$ , the material is considered hydrophilic and the liquid water as wetting. Conversely, the material is considered hydrophobic and the liquid water as non-wetting. Finally, there is a pressure discontinuity at the interface of the non-wetting and wetting phase when a mechanical equilibrium is reached. The capillary pressure  $P_c$  defines this pressure difference [51]:

$$P_c = P_{nw} - P_w \quad (\text{I-14})$$

where nw and w subscripts refer to the non-wetting and wetting phase, respectively. Capillary pressure is generally estimated by the following equation in PEM fuel cells [52]:

$$P_c = \sigma \cos(\theta) \left( \frac{\varepsilon}{K} \right)^{1/2} J(s) \quad (\text{I-15})$$

where the interfacial tensions are represented by the surface tension  $\sigma$  and the contact angle  $\theta$ .  $\varepsilon$  and  $K$  refer to porosity and permeability, respectively. These parameters are characteristic of the porous medium and presented in details in Chapter II.  $J(s)$  is the Leverett J-function [53], which is a dimensionless function depending only on liquid saturation (this notion is discussed at length in Chapter II-4.1.2). This empirical relationship, used primarily in petroleum engineering, was extended for both hydrophilic and hydrophobic porous materials in fuel cell [52][54]:

$$J(s) = \begin{cases} 1.417(1-s) - 2.120(1-s)^2 + 1.263(1-s)^3 & \text{for } \theta < 90^\circ \\ 1.417s - 2.120s^2 + 1.263s^3 & \text{for } \theta > 90^\circ \end{cases} \quad (\text{I-16})$$

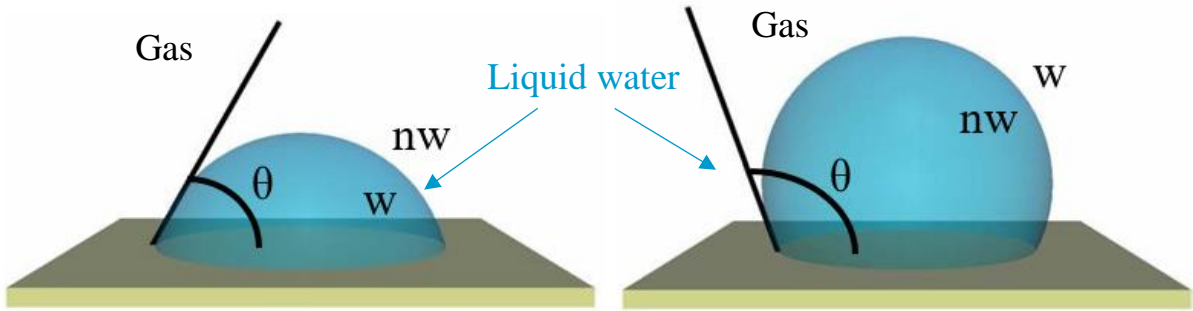


Fig. I-13. Liquid water: wetting (left) and non-wetting (right) – modified from [59].

Other capillary pressure saturation relations are proposed by [55]-[58]. The porous materials in PEM fuel cells must be as hydrophobic as possible ( $\theta > 90^\circ$ ) to reject water from the porous layers towards the channels. The capillary pressure is then written:

$$P_c = P_g - P_l \quad (\text{I-17})$$

In this configuration (hydrophobicity of the porous layers), the pressure of the liquid phase is higher than the gas phase pressure. The liquid phase is then drained from the porous layers towards the channels. Conversely (hydrophilicity of the porous layers), liquid water accumulates, which can cause the PEM fuel cell to flood. This notion is discussed at greater length in the section 3.3.2 of this chapter.

### 3.2.3 Convection Transport of Water in the Gas Channels

Liquid water is transported mainly by convection in the gas channels. On the one hand, water comes directly from the porous layers due to their hydrophobic nature and the various transport mechanisms seen previously. On the other hand, water can condense directly in the channels if temperature decreases. Zhang et al. [60] experimentally examined the distribution of liquid water in the GCs on the cathode side under standard operating conditions. They classified the two-phase flow in PEMFC gas channels as a mist flow at high gas velocities, steady corner flow at low gas velocities and low water production and annular film/slug flow at low gas velocities and high production of liquid water. Hussaini and Wang [61] visualized channel two-phase

flow by in situ visualization in an operating fuel cell. They found results close to the work of Zhang et al. [60] with droplet, film and slug flows (Fig. I-14). Flow patterns of liquid water remain difficult to observe experimentally. Finally, they are impacted by the water intrusion mechanisms from GDLs to gas channels. Many authors study water intrusion mechanisms [59][62]-[63].

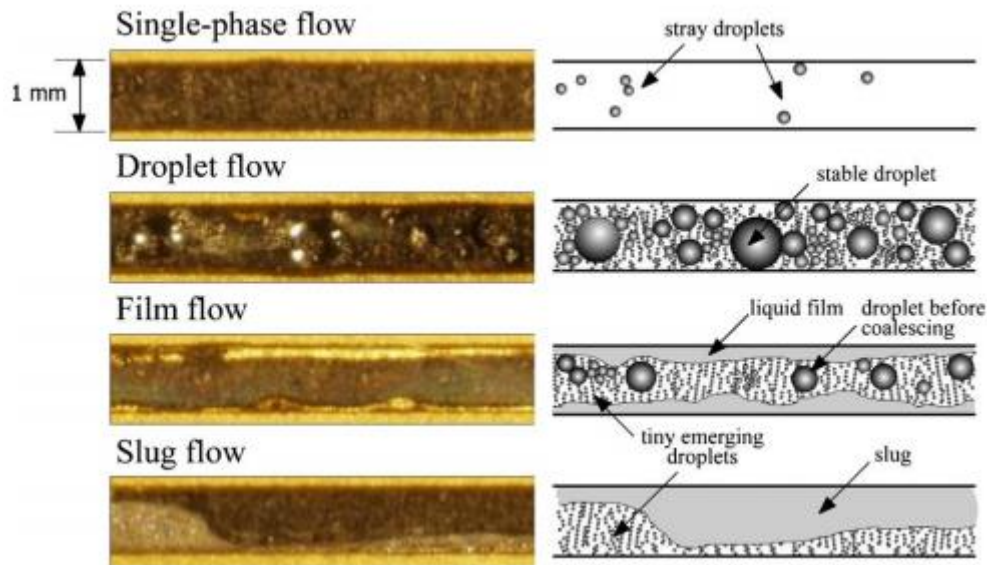


Fig. I-14. Magnified view of flow patterns in channels and their corresponding line illustrations showing the form and distribution of liquid water [61].

### 3.3 Effect of Water Management on PEM Fuel Cells Performance and Degradation

Water management is essential to optimize the performance of PEM fuel cells. On the one hand, it is crucial for maintaining good hydration of the membrane and thus its proton conductivity [41]. On the other hand, liquid water would cause mass transfer blockages in the catalytic and diffusion layers but also in the gas flow channels. The equilibrium between membrane drying and cell flooding is a difficult task for a proper water management, which can cause irreversible degradation [64].

#### 3.3.1 Membrane Dehydration

The membrane can dry out notably if the inlet reactant gases are low-humidified. The dehydration occurs particularly at the hydrogen inlet since the production of water at the cathode is not

sufficient to compensate (with back diffusion) the water lack in this area [65]. In addition, a poor water and temperature management may cause local membrane dehydration [66]. In the absence of water, protons cannot migrate through the ionomer. Therefore, the ionic conductivity drastically decreases [67], increasing the activation overpotential [68]-[69]. Moreover, the dehydration of the membrane herds to higher ionic resistances [41], which leads to potential losses and consequently to a power drop. Büchi and Srinivasan [70] measured the current density at constant potential (0.61 V) of a PEMFC during 1,200 hours of operation using unhumidified inlet gas. They observed a current density decrease from 170 to 130 mA/cm<sup>2</sup> during the test. Finally, hot spots cause irreversible degradation such as micro-cracks and pinholes in the membrane [71], which induces gas crossover and therefore a cell dysfunction with unwanted reactions.

### 3.3.2 Cell Water Flooding

As seen previously, water accumulates due to continuous production, pre-humidification and consumption of the reactant gases, which can cause the fuel cell to flood. Flooding can occur in all the layers at both the anode and cathode side particularly when the water and temperature are poorly managed. Flooding drastically reduces the gas transport in PEMFCs. First, it stops reactants from reaching the active layer by filling the GDL/MPL pores [72]. Accordingly, the cell potential drops immediately when there is an underfeeding until a starvation of hydrogen and oxygen preventing HOR and ORR [73]-[74]. Oxygen depletion can even cause a parasitic reaction at the cathode [64], which leads to a zero potential. Moreover, the gas channels can be flooded as well as porous media [64], which blocks gases from the flow channels to the GDLs. Eventually, flooding has other (irreversible) consequences such as a PEM fuel cell operation with strong heterogeneities or the chemical degradation of the catalysts [75]-[76].

Finally, Nandjou et al. [71] analyzed post-mortem PEM cells after 2,000 h durability tests in automotive conditions. They observed that the successive variations in water content (dehydration or high water concentration), representative of an automobile operation, causes significant degradations affecting both the performance and durability of the fuel cell.

#### 4. State of the Art of Numerical PEMFC Models

Numerical modeling appears to be a powerful tool in addition to experiments in fuel cells as well as in many other fields (aviation, medicine, chemistry, etc.). Indeed, experimental tests to locate and quantify liquid water, whether at the component level or the entire stack, can be complex to set up, expensive, time consuming and limited in resolution [77]. Accordingly, numerical models present some advantages as low simulation time and low computational cost. In addition, after validation, they can help to better understand physical phenomena in PEM fuel cells, which cannot or hardly be observed by experimentation. As discussed before, the physical phenomena within a cell are very complex due to two-phase flow with phase change, species transport with consumption and production, heat transfer, electrochemical reactions, etc. A fully 3D model taking into account all the physics, especially the complex multiphase fluid dynamic, seems necessary to represent correctly a PEM fuel cell operation. However, such a model has not yet been developed due to complex geometry needing high resolution meshing, coupling difficulties and still limited computing power. In consequence, large scale models adopt some assumptions and simplifications concerning the governing equations, the number of considered layers or the boundary conditions such as a single-phase flow or simplified geometry. Springer et al. [41] and Bernardi–Verbrugge [78] were the first to develop fuel cell models. Since, many computational heat and water transport models have been developed at different scales, from 1D to 3D, from one single component to entire cell, etc. Many reviews [79]-[82] established the state of the art of computational modeling in PEM fuel cells, which frequently discuss the models strengths and weaknesses.

Commercial models including fuel cell module have been developed these last years. Star CCD® was the first Computational Fluid Dynamics (CFD) software to implement a fuel cell module. ANSYS Fluent®, ANSYS CFX®, AVL FIRE® and COMSOL Multiphysics® are the most common CFD software including fuel cell module. Fink and Fouquet [83] developed a 3D model using the AVL FIRE® fuel cell module. They identified some shortcomings, especially in the membrane transport model. As a result, researchers commonly develop their own model.

According to the evolution and the current status of PEMFC models, there is a need of multiphase flow models in order to better understand the water management in PEM fuel cells [84]. Among the first research publications with respect to multiphase modelling were Wang and

Cheng [85]. Based on the multiphase mixture theory, Zhuge et al. [86] developed a three-dimensional gas/liquid two-phase flow model applied to a part region of the fuel cell. Results showed that the liquid water distribution is mostly in the cathode, and predicted cell performance decreases quickly at high current density due to the obstruction of liquid water to oxygen diffusion. Siegel [87] introduced a two-dimensional model inside the gas diffusion layer and demonstrated that the fluid temperature is overestimated by one-phase models if there is phase change. With a two-dimensional multicomponent mixture model in a porous cathode adjacent to a flow channel, Wang et al. [88] studied a threshold current density corresponding to first appearance of liquid water in order to evaluate the water distribution and transport at the membrane/cathode interface. A 2-D multicomponent transport model was developed by He et al. [89] to investigate the effects of the gas and liquid flow on the cathode performance. Phase change was also discussed by Wang et al. [90] and Basu et al. [91]. More recently, Bednarek and Tsotridis [92] presented the possible limitations and difficulties associated with PEM single fuel cell modelling. Anderson et al. [93] published a review of cell-scale multiphase flow modeling, including water management with a focus on phase-change and transport processes. Zhang and Jiao [94] also reviewed multiphase models for water and thermal management of PEM fuel cell.

Several transport phenomena models in different layers of PEM fuel cell and in different length scales according to the Knudsen number [51] are identified in Fig. I-15 [94]. The Finite Element Method (FEM) [95], widely used for numerically solving Partial Differential Equations (PDE) and Volume Of Fluid (VOF) method [96], which tracks the gas and liquid phase interface, are the most popular method in macroscopic scale to simulate the gas and liquid two-phase flow in channel and GDL [97]-[98]. At the mesoscopic scale, the Lattice Boltzmann Method (LBM) [99], based on streaming–collision process, appears to be an efficient method to simulate multiphase flow in complicated microstructures due to its numerical stability and versatility. For example, Molaeimanesh and Akbari [100] study the removal of liquid water from a PEMFC electrode with different PTFE distributions by lattice Boltzmann method. The Pore Network Modeling (PNM) creates a virtual representation of the porous medium to simulate fluid flow through it. This method is a powerful tool to study two-phase flow at the meso-scale in PEMFCs [62][101] with a low calculation time compared to Direct Numerical Simulation (DNS). Finally, the Molecular Dynamics (MD) [102] or Quantum Mechanics (QM) [103] methods are used to numerically analyze the transfer phenomena at the microcosmic scale such as proton transport

in PEM. In this study, PEMFC multiphysics including the complex two-phase flow are exclusively examined from a macroscopic point of view by using continuous models based on the finite element method. Here are the two main continuous models of two-phase flow in PEM fuel cells at the cell scale.

#### Homogeneous Equilibrium Model (HEM)

##### *Multiphase Mixture ( $M^2$ ) Model*

The Homogeneous Equilibrium Model (HEM), also called Multiphase Mixture ( $M^2$ ) model, considers the two-phase mixture as a pseudo-single-phase with physical properties weighted by the volume fraction of each phase. Therefore, it is necessary to properly define the properties of the two-phase mixture. Several mixture correlations can be found in the work of Lee and Mudawar [104] such as the mixture density and the mixture viscosity. Thereby, only one set of conservation equations can be applied to the two-phase mixture thus saving computational time. Mechanical and thermodynamic equilibrium are maintained as the name suggests. In addition, identical velocities are considered between the liquid and gas phases both moving at the mixture velocity, which is a significant simplification of the two-phase flow. Wang et al. [105][90] were the first to develop a PEM fuel cells model based on the  $M^2$  formalism. They introduced some correction factors to take into account the difference between phase velocities in the convective transport of the two-phase mixture. This model can be compared to a drift model, developed in the nuclear field, introducing a slip velocity. Nevertheless, it is difficult to find the right formulation of the correction factors / mixture constitutive laws.

#### Two-Fluid Model

The two-fluid (2-F) model, also called the Euler-Euler model, considers each phase individually by formulating conservation equations for both phases. The two-fluid model is complex since the transfer of mass, momentum and energy from one phase to another are treated. Therefore, it is necessary to find the appropriate closure laws, which are still widely discussed in the literature. In addition, the closure laws have a significant impact on the model convergence and the accuracy of the results, as we will see in Chapter IV. Finally, the two-fluid model can predict complex two-phase flows with thermofluid dynamic and non-equilibrium interactions between the phases compared to the 1-F/mixture models.

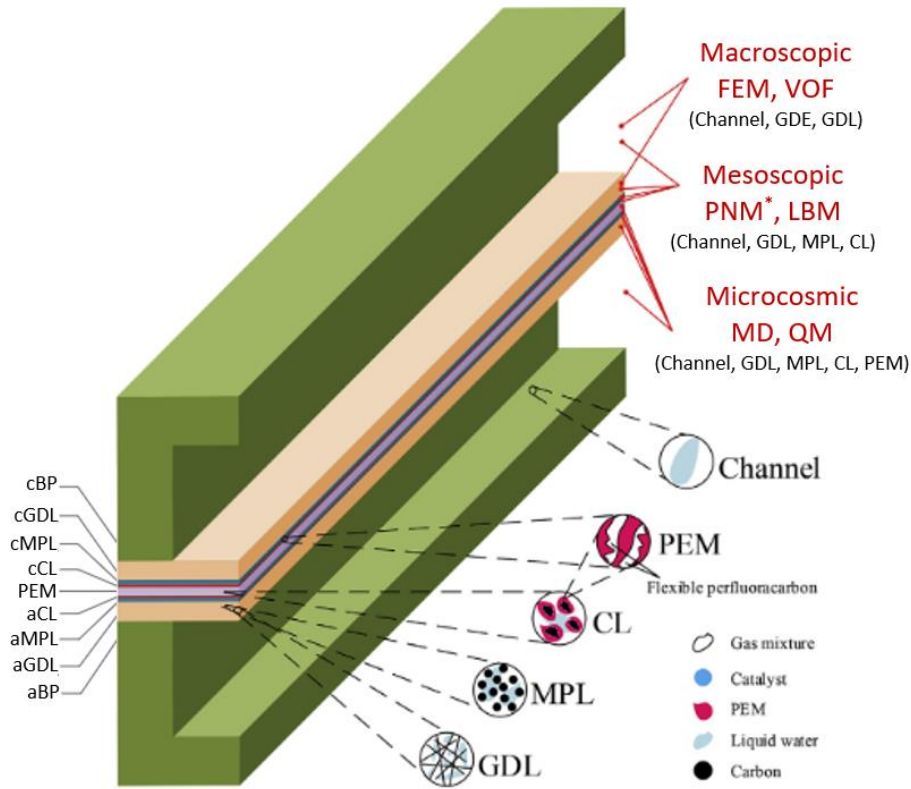


Fig. I-15. Schematic of different modeling scales in PEM fuel cell – modified from [94].  
\* not used in gas channels

## Conclusion

The current urgency to limit our CO<sub>2</sub> emissions is essential to envisage a sustainable future. From this perspective, hydrogen today appears to be a major energy vector for the storage of the electrical energy produced by non-polluting processes. Therefore, hydrogen is highly considered as a new clean fuel to decarbonize the transport sector by using fuel cells. Among the technologies envisaged, the Proton Exchange Membrane Fuel Cell (PEMFC) is the most suitable system for automobile operation because of its excellent dynamic, high power density and good electrical efficiency. Its operating principle and its various components have been detailed in this chapter. In addition, the fuel cell system and the objectives to be achieved for a large scale commercialization were briefly reviewed. Despite the growing interest in PEM fuel cells, increasing its durability remains the greatest challenge due to some irreversible degradations during its operation. Indeed, no proper management of water and temperature appears to be one of the main causes of degradation and performance drop.

The different water transport mechanisms were detailed in all the layers of the fuel cell. Finally, a state of the art of two-phase flow models is presented to use numerical simulation as a powerful tool in addition to experimental tests to better understand transport phenomena in PEM-FCs.

## **Chapter II**

# **MODEL FORMULATION OF THERMOFLUID MECHANICS IN PEM FUEL CELLS**

## Introduction

As presented above, a PEM fuel cell is a multilayers and multiphysics system. Electrochemical reactions, thermofluid dynamic flow and phase change occur simultaneously within a cell. All these processes are interdependent and affected by both the component design and material properties. Each parameter is dependent on at least two other parameters in PEM fuel cells [106]. It is therefore not possible to change one parameter without changing others. Accordingly, it is relevant to better understand the theoretical PEMFC physics still amply discussed in the literature. In this chapter, the theory of thermofluid mechanics in PEM fuel cells is examined with emphasis on the continuity equations of mass, species mass, momentum and energy starting with the local and instantaneous equations. The local volume-averaging method is then performed to obtain the macroscopic Navier-Stokes (N-S) equations in a porous medium. The equations are first described for a single-phase flow. Note that the gas channels are treated as porous media (Darcy's law) with a tortuosity and porosity equal to the unit. This approach has been used in several studies [90]. Heat and mass transfer in porous media using the method of volume-averaging have been detailed in the work of Whitaker [107], Carbonell and Whitaker [108] and Kaviany [51]. The chapter ends with the hydrodynamic equations of the two-phase flow by describing the equations for each phase. Two-phase flow have been presented by many authors such as Sha et al. [109], Faghri and Zhang [110], Delhaye [111], Ishii and Hibiki [112] and Morel [113].

### 1. Interest of Averaging

From an engineering point of view, it is necessary to obtain accurate properties on a large scale in order to size FCs and optimize their performance. The average method seems to be the most suitable method based on continuum mechanics and thermodynamics theory for obtaining macroscopic values of physical phenomena in large surface PEM fuel cells. In addition, models depend on the availability of experimental data, which are provided most of the time from a macroscopic point of view. Moreover, two-phase flow through a porous medium at the pore scale are still difficult:

- to observe with experimental tests. The methods used are more or less precise, often costly and performed in laboratory. Bazylak [114] reviewed the liquid water visualization methods especially in GDLs. The challenges and limitations of these methods are also discussed in her work.
- to calculate with numerical models. Indeed, Direct Numerical Simulation (DNS) must be used to simulate the transport phenomena in the real geometry of the pore network. In return, DNS requires substantial computational resources, a long calculation time and a refined mesh. Some models (PNM, LBM, etc.), as briefly discussed in the previous chapter, are well suited to the pore scale delivering valuable data to determine, for example, GDL effective transfer coefficients as a function of local properties [115]. However, these models are not adapted for a macroscopic scale (unit cell, stack, etc.).

For these reasons, the equations describing the physical processes in PEM fuel cells have to be averaged to obtain macroscopic properties. The averaged equations are then implemented in numerical models. However, applying the averaging operator greatly complicates the equations, especially when considering a two-phase flow through a porous medium with the appearance of many interfacial terms. In addition, these terms cannot be directly used as such in numerical models and must be adequately closed. Indeed, the conservation equations are not sufficient to determine all the variables. Closure laws have been the subject of much discussion in the literature for decades. Before introducing the equations, it is necessary to introduce some definitions and mathematical tools.

## 2. Porous Medium

### 2.1 Porosity

As discussed previously, several components of the cell are porous material, such as the gas diffusion and micro-porous layers. A porous medium is composed of a matrix and voids (or pores as the name suggests). Fig. II-1 represent a schematic of a porous medium. The porosity is defined as the ratio of the volume fraction occupied by the voids, which means the volume of the pores on the total volume (including the solid matrix and the volume of the pores):

$$\varepsilon \stackrel{\text{def}}{=} \frac{V_f}{V_s + V_f} = \frac{V_f}{V} \quad (\text{II-1})$$

where  $V_f$  is the fluid volume,  $V_s$ , the matrix volume and  $V$ , the total volume. Usually, the solid matrix is considered rigid in PEMFC; this approach is retained in this work. Therefore, the porosity characterizing the porous medium is assumed constant and does not depend on the pressure. Furthermore, the voids are instantly occupied by the fluid-phase, which imply that each pore is connected to other ones. Accordingly, the pore network is considered continuous. The volume fraction is so called effective porosity, called only porosity hereafter. A detailed description can be found in [51]. El-kharouf et al [116] measured the mean pore diameter for many commercial GDLs using a mercury porosimeter. The characterized GDLs in their work have pores between 0.5 and 10  $\mu\text{m}$  in radius (Table II-1).

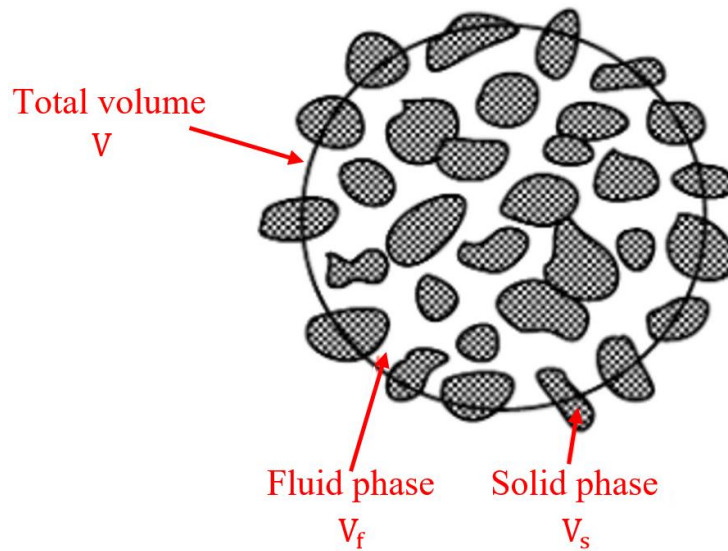


Fig. II-1. A schematic of a porous medium with a continuous fluid phase in PEMFC – modified from [117].

**Table II-1** [116]

Commercial GDL properties.

Material	Manufacturer materials' properties			Measured properties						
	Thickness ( $\mu\text{m}$ )	Area weight ( $\text{gm}^{-2}$ )	Bulk density ( $\text{gcm}^{-3}$ )	Real density ( $\text{gcm}^{-3}$ )	Bulk density ( $\text{gcm}^{-3}$ )	Surface roughness ( $\mu\text{m}$ )		Porosity %	Tortuosity	Mean pore diameter (nm)
						Sa	Sq			
1071HCB	356	123	0.35	1.816 $\pm$ 0.002	0.39	—	—	64.9	1.95	3401
P50	170	50	0.32	2.083 $\pm$ 0.004	0.36	14.7 $\pm$ 0.8	19.8 $\pm$ 0.5	48.7	3.01	993
P50T	180	62	0.34	2.151 $\pm$ 0.004	0.37	15.7 $\pm$ 0.6	19.4 $\pm$ 0.3	44.9	2.55	1528
GDS1120	210	79	0.40	2.125 $\pm$ 0.005	0.46	20.0 $\pm$ 3.0	25.0 $\pm$ 4.0	44.8	3.24	859
P75	230	75	0.33	2.083 $\pm$ 0.005	0.35	14.2 $\pm$ 0.9	20.0 $\pm$ 2.0	62.4	2.43	2074
P75T	255	88	0.33	2.087 $\pm$ 0.003	0.36	14.0 $\pm$ 1.0	18.0 $\pm$ 2.0	59.9	2.23	1227
GDS2120	260	101	0.40	2.131 $\pm$ 0.005	0.40	17.0 $\pm$ 2.0	23.0 $\pm$ 5.0	60.2	2.62	2998
TGP-H-030	110	—	0.40	2.071 $\pm$ 0.001	0.37	14.0 $\pm$ 1.0	18.1 $\pm$ 0.9	64.6	2.50	2625
TGP-H-060	190	—	0.44	2.002 $\pm$ 0.003	0.43	14.1 $\pm$ 0.2	19.1 $\pm$ 0.6	63.1	2.76	2631
TGP-H-090	280	—	0.44	2.019 $\pm$ 0.003	0.49	13.0 $\pm$ 0.5	17.9 $\pm$ 0.4	67.2	2.55	3324
TGP-H-120	370	—	0.45	1.985 $\pm$ 0.004	0.49	12.2 $\pm$ 0.5	17.3 $\pm$ 0.8	61.8	2.51	1717
C2	250	130	—	1.882 $\pm$ 0.002	0.57	14.6 $\pm$ 0.4	19.6 $\pm$ 0.9	49.2	4.51	658
C4	250	130	—	1.900 $\pm$ 0.002	0.49	14.0 $\pm$ 1.0	18.9 $\pm$ 0.6	61.0	4.26	158
I2 C6	250	135	—	1.867 $\pm$ 0.002	0.54	9.5 $\pm$ 0.4	12.7 $\pm$ 0.4	46.2	5.02	1148
I2 C8	230	135	—	1.934 $\pm$ 0.002	0.62	8.4 $\pm$ 0.6	11.3 $\pm$ 0.8	47.0	4.91	682
LT 1200N	185	75	0.41	2.053 $\pm$ 0.004	0.39	17.0 $\pm$ 2.0	22.0 $\pm$ 0.8	64.9	2.74	769
LT1200W	275	200	0.73	1.906 $\pm$ 0.002	0.50	—	—	31.8	2.74	1055
GDL 10 BC	420	135	—	1.945 $\pm$ 0.008	0.36	24.0 $\pm$ 2.0	31.0 $\pm$ 3.0	34.6	2.95	2919
GDL 24 BA	190	54	—	2.140 $\pm$ 0.010	0.28	13.4 $\pm$ 0.9	17.0 $\pm$ 2.0	73.9	1.40	2208
GDL 24 BC	235	100	—	2.010 $\pm$ 0.003	0.44	13.3 $\pm$ 0.1	18.3 $\pm$ 0.8	40.0	3.00	2450
GDL 25 BA	190	40	—	1.941 $\pm$ 0.002	0.21	22.0 $\pm$ 4.0	31.0 $\pm$ 3.0	66.2	1.45	1705
GDL 25 BC	235	86	—	2.009 $\pm$ 0.007	0.34	23.0 $\pm$ 4.0	32.0 $\pm$ 3.0	36.5	2.92	842
GDL 34 BC	315	140	—	1.987 $\pm$ 0.001	0.41	23.9 $\pm$ 0.9	30.8 $\pm$ 0.2	47.5	2.47	2197
GDL 34 DC	—	—	—	1.978 $\pm$ 0.004	0.48	25.0 $\pm$ 2.0	31.0 $\pm$ 3.0	40.8	2.62	1593
GDL 35 BA	300	54	—	2.022 $\pm$ 0.009	0.19	32.0 $\pm$ 3.0	43.0 $\pm$ 3.0	70.5	1.33	2469
GDL 35 BC	325	110	—	1.980 $\pm$ 0.007	0.31	36.0 $\pm$ 2.0	46.0 $\pm$ 5.0	52.6	1.94	1467
TCC-2660	260	80	0.31	1.793 $\pm$ 0.003	0.34	—	—	66.9	1.83	2291
TCC-3250	320	100	0.31	1.803 $\pm$ 0.002	0.36	—	—	71.0	2.32	1631

## 2.2 Representative Elementary Volume

The size and distribution of the pores are generally not uniform in porous materials in a PEM fuel cell as presented by Fig. II-1. In order to avoid describing precisely all the pores (and a direct simulation), it is then necessary to introduce the concept of the Representative Elementary Volume (REV) that considers each pore identically represented by an average diameter (or length) noted  $d$ . Therefore, the REV can be defined as the smallest volume with statistically significant local properties. This implies that the characteristic length of the REV noted  $l$  is much larger than the average characteristic length of a pore ( $l \gg d$ ) [107]. From another point of view, the local properties in the REV such as porosity, permeability or conductivity are not affected by the addition of pores. Furthermore, the characteristic length of the REV must be much smaller than the system dimension (unit cell, component) noted  $L$  ( $L \gg l$ ) to assume negligible variations in the elementary volume compared to the total volume. Fig. II-2 represents the multiscale aspects in porous media. Kaviany [51] well described the pore structure and REV for any porous medium.

Finally, the local and instantaneous equations – at the microscopic scale – are averaged over the REV to obtain the macroscopic properties. The local volume-averaging over the REV includes the local average at the pore scale when the difference between the pore volume and REV is satisfied ( $l \gg d$ ) [107]. Mathematically, this equality is written as follows:

$$\langle\langle\psi\rangle\rangle = \langle\psi\rangle \quad \text{if } l \gg d \quad (\text{II-2})$$

where  $\psi$  is any quantity. The simple average notation  $\langle \rangle$  is adopted in the rest of the document.

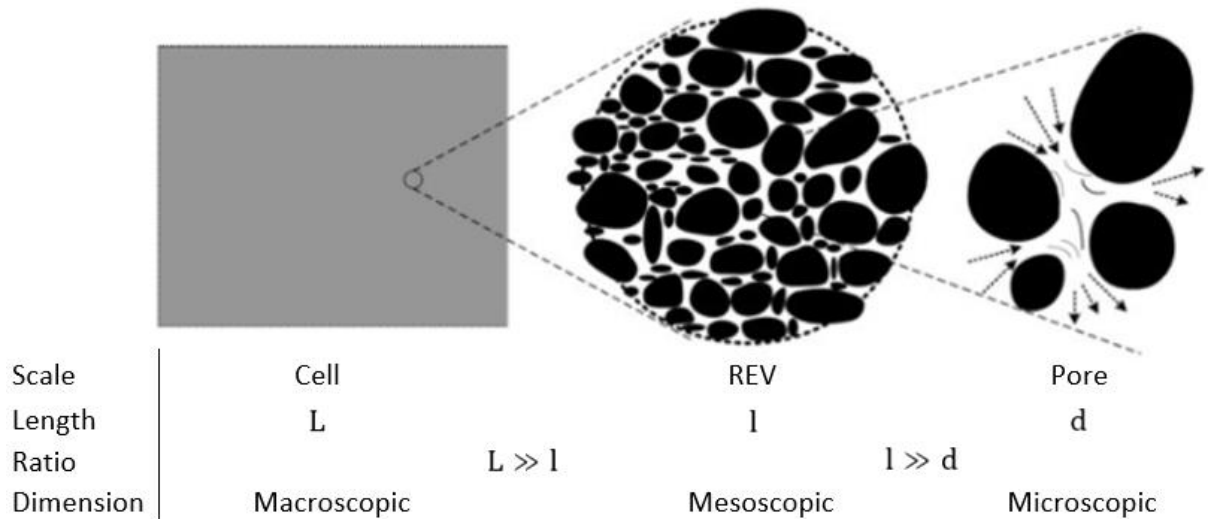


Fig. II-2. Schematic of the multiscale aspects in porous media – modified from [118].

### 3. Single-Phase Flow

In this section, the conservation equations are examined from the local instant formulation for a single-phase flow. The equations of mass, species mass, momentum and energy are detailed and averaged over the REV. The aim of averaging the equations for a single-phase flow is to become familiar with mathematical averaging tools before applying them to a two-phase flow for which the dynamic and non-equilibrium interaction between the liquid and gas phases are considered. In addition, some numerical models use the single-fluid formulation such as the one-fluid and mixture models. Before averaging the equations, we need some mathematical definitions and theorems.

### 3.1 Mathematical Averages

#### 3.1.1 Local Volume-Average

In order to formulate the macroscopic equations, the classical local volume-average is introduced. It is the integration of a local quantity over a chosen volume and can be mathematically defined as:

$$\langle \psi \rangle \stackrel{\text{def}}{=} \frac{1}{V} \int_V \psi \, dv \quad (\text{II-3})$$

#### 3.1.2 Local Volume-Average Associated to the Fluid-Phase

The local volume-average presented by Eq. (II-3) is applied to a fluid quantity through a porous media. Mathematically, we obtain:

$$\langle \psi_f \rangle \stackrel{\text{def}}{=} \frac{1}{V} \int_{V_f} \psi_f \, dv = \varepsilon \frac{1}{V_f} \int_{V_f} \psi_f \, dv \quad (\text{II-4})$$

where  $\psi_f$  represents any local quantity associated to the fluid-phase. This mathematical technique allows a change of scale from a microscopic to macroscopic dimension in a porous medium.

#### 3.1.3 Local Intrinsic-Average Associated with the Fluid-Phase

The solid matrix and therefore its associated volume is non-negligible in the porous components of the PEM fuel cell even if the porosity can reach more than 80% in GDL. Consequently, defining some fluid properties such as density or velocity from the local volume-average – applied to the total volume – seems inappropriate. The local intrinsic-average is then introduced, which is more representative of the phase considered, since it takes into account the phase volume and not the total volume. The intrinsic-average is also called phase-average in the literature. The local intrinsic-average associated to the fluid is defined by:

$$\langle \psi_f \rangle_f \stackrel{\text{def}}{=} \frac{1}{V_f} \int_{V_f} \psi_f \, dv = \frac{1}{\varepsilon V} \int_{V_f} \psi_f \, dv \quad (\text{II-5})$$

where the subscript  $f$  after the second bracket means that the average is defined on the volume occupied by the fluid phase. Therefore, the relation between the local volume and intrinsic averages is:

$$\langle \psi_f \rangle = \varepsilon \langle \psi_f \rangle_f \quad (\text{II-6})$$

This relationship is essential to express the local averaged equations through a porous media.

### 3.2 Theorems

In order to obtain the averaged equations, we need to interchange the averaging operator with the derivation operators. Indeed, the average of the gradient (or divergence) operator is not equal to the gradient (or divergence) of the average. The general form of the Reynolds transport theorem and the Green-Ostrogradski theorem are both used to demonstrate the relation between the volume-average of a gradient (or divergence) and the gradient (or divergence) of the volume-average. These theorems introduce the discontinuities at the solid-fluid interface. Demonstrations have been developed by Slattery [119]-[120] and Whitaker [107].

#### 3.2.1 Theorem of the Volume-Average of a Gradient

Finally, the theorem for the volume-average of a gradient is:

$$\langle \nabla \psi_f \rangle = \nabla \langle \psi_f \rangle + \frac{1}{V} \int_{A_{sf}} \psi_f \, \mathbf{n}_f \, da \quad (\text{II-7})$$

where  $A_{sf}$  is the solid-fluid interface area and  $\mathbf{n}_f$ , the unit vector perpendicular to  $A_{sf}$  pointing out the fluid phase. The last Right-Hand Side (RHS) term then represents the discontinuity on the solid-fluid interface area.

### 3.2.2 Theorem of the Volume-Average of a Divergence

Similarly, the theorem for the volume-average of a divergence is:

$$\langle \nabla \cdot \psi_f \rangle = \nabla \cdot \langle \psi_f \rangle + \frac{1}{V} \int_{A_{sf}} \psi_f \cdot \mathbf{n}_f \, da \quad (\text{II-8})$$

These two theorems are useful tools to average the continuity equations.

### 3.3 Local Volume-Averaged Mass Equation

The local continuity equation for mass in PEMFC considering a single-fluid flow is:

$$\frac{\partial \rho_f}{\partial t} + \nabla \cdot [\rho_f \underline{V}_f] = r_f \quad (\text{II-9})$$

where  $\rho_f$  is the fluid-phase density,  $\underline{V}_f$ , the fluid-phase velocity vector,  $r_f$ , the mass source of the fluid-phase induced by electrochemical reaction, i.e. both production and consumption. When volume averaged, this latter equation becomes:

$$\frac{\partial}{\partial t} \langle \rho_f \rangle + \nabla \cdot \langle \rho_f \underline{V}_f \rangle = \langle r_f \rangle \quad (\text{II-10})$$

As mentioned previously, the matrix volume is considered rigid, i.e. independent of time. The unsteady term in Eq. (II-10) is then obtained by:

$$\left\langle \frac{\partial \rho_f}{\partial t} \right\rangle = \frac{1}{V} \int_{V_f} \frac{\partial \rho_f}{\partial t} \, dv = \frac{\partial}{\partial t} \left( \frac{1}{V} \int_{V_f} \rho_f \, dv \right) = \frac{\partial}{\partial t} \langle \rho_f \rangle \quad (\text{II-11})$$

Moreover, the fluid velocity is assumed to be zero at the solid-fluid interface. By using the local averages relation (II-6), Eq. (II-10) becomes:

$$\frac{\partial}{\partial t} [\varepsilon \langle \rho_f \rangle_f] + \nabla \cdot [\varepsilon \langle \rho_f \underline{V}_f \rangle_f] = \varepsilon \langle r_f \rangle_f \quad (\text{II-12})$$

The demonstration can be found in Appendix A.

### 3.4 Favre Averaging

The term of the convective transport in Eq. (II-12) includes the average of a product. However, the average of a product is not equal to the product of the averages. Either the Reynolds decomposition or the Favre averaging is necessary to obtain the average product. The Reynolds average of a product is difficult to use since introducing fluctuating quantities. Favre therefore defined a new averaging operator – density-weighted – as following:

$$\overline{\overline{\psi}} \stackrel{\text{def}}{=} \frac{\langle \rho \psi \rangle}{\langle \rho \rangle} \quad (\text{II-13})$$

Where  $\overline{\overline{\psi}}$  denotes Favre (or density-weighted) averaging operator. The Favre average is a simple way to express the average of a product without explicitly separating the fluctuating quantity from the mean quantity. Favre's average therefore refers to the mass center and no longer to the volume center of the quantity considered. By using the Favre averaging, Eq. (II-12) becomes:

$$\frac{\partial}{\partial t} [\varepsilon \langle \rho_f \rangle_f] + \nabla \cdot [\varepsilon \langle \rho_f \rangle_f \overline{\overline{\mathbf{V}_f}}] = S_f \quad (\text{II-14})$$

where  $\overline{\overline{\mathbf{V}_f}}$  is the Favre-averaged fluid velocity vector. The source term by electro-chemical reaction in its local volume-averaged form defined by  $S_f$  is preferred:

$$S_f = \varepsilon \langle r_f \rangle_f \quad (\text{II-15})$$

### 3.5 Local Volume-Averaged Species Mass Conservation Equation

In any PEM fuel cells, electrochemical reactions take place simultaneously on both sides of the MEA. It is then necessary to describe the mass transfers by electrochemical reactions in gases for a single phase first. The gas mass transport is examined for multicomponent gas mixtures, namely hydrogen and water vapor at the anode side and oxygen, nitrogen and water vapor at the cathode side as air is generally used instead of pure oxygen in PEMFC. The local mass conservation equation of the  $j$ -specie ( $j$ : H<sub>2</sub>, O<sub>2</sub> and H<sub>2</sub>O) in the fluid-phase is expressed by:

$$\frac{\partial}{\partial t} [\rho_f Y_{jf}] + \nabla \cdot [\rho_f Y_{jf} \underline{V}_{jf}] = r_{jf} \quad j = 1, N_f \quad (\text{II-16})$$

where  $N_f$  is the number of species,  $Y_{jf}$ , the mass fraction of the  $j$ -specie,  $\underline{V}_{jf}$ , the velocity vector of the  $j$ -specie in the fluid-phase and  $r_{jf}$ , the mass source of the  $j$ -specie by electrochemical reaction (production or consumption). The double subscript  $jf$  is adopted to signify that the  $j$ -specie is present in the fluid phase. This information is redundant because only a single-phase is considered in this section but it will be important for a two-phase flow where water can be present in both liquid and gas phases. The equation of the species mass conservation is solved for  $N_f - 1$  species at both side since the mixture density is calculated from the continuity equation. For example, the density of the nitrogen is deduced by difference of the mixture density and the densities of the oxygen and water vapor. All gases are considered as perfect. In addition, the velocity of the  $j$ -specie in the fluid-phase,  $\underline{V}_{jf}$ , can be different from the fluid-phase velocity,  $\underline{V}_f$ , which classically leads to the introduction of a diffusive flux  $j_{jf}$ :

$$j_{jf} \stackrel{\text{def}}{=} \rho_f Y_{jf} (\underline{V}_{jf} - \underline{V}_f) \quad (\text{II-17})$$

The local species mass conservation equation (II-16) can be rewritten as:

$$\frac{\partial}{\partial t} [\rho_f Y_{jf}] + \nabla \cdot [\rho_f Y_{jf} \underline{V}_{jf}] = -\nabla \cdot j_{jf} + r_{jf} \quad (\text{II-18})$$

when volume averaged by introducing the Fick's law to represent the diffusion flux, Eq. (II-18) becomes:

$$\frac{\partial}{\partial t} \langle \rho_{jf} \rangle + \nabla \cdot \langle \rho_{jf} \underline{V}_f \rangle = \nabla \cdot [D_{mj} \nabla \langle \rho_{jf} \rangle] + \langle r_{jf} \rangle + S_{jf}^{\text{sf}} \quad (\text{II-19})$$

where  $\rho_{jf}$  is the density of the  $j$ -specie in the fluid-phase ( $\rho_{jf} = \rho_f Y_{jf}$ ),  $D_{mj}$ , the mass diffusion coefficient of the  $j$ -specie diffusing into the other species and  $S_{jf}^{\text{sf}}$ , the sorption term. Sorption is an interface phenomenon as indicated by the superscript  $\text{sf}$  (solid-fluid interface). For a single-fluid through a porous medium, the physical adherence of the gas mixture onto the solid matrix surface is called adsorption and the reverse process desorption. The sorption phenomenon is neglected by the one-fluid and two-fluid models in Chapter III and Chapter IV. As for the mass

balance, the same assumptions are made for this equation (rigid matrix and zero fluid velocity at the solid-fluid interface). Furthermore, the negligible variations of the mass diffusion coefficient of the  $j$ -specie over the averaging volume is assumed. Finally, the local volume-averaged species mass conservation equation leads to:

$$\frac{\partial}{\partial t} [\varepsilon \langle \rho_{jf} \rangle_f] + \nabla \cdot [\varepsilon \langle \rho_{jf} \rangle_f \underline{\underline{V}}_f] = \nabla \cdot [D_{mj} \nabla [\varepsilon \langle \rho_{jf} \rangle_f]] + S_{jf} + S_{jf}^{sf} \quad (\text{II-20})$$

where  $S_{jf}$  is the volume-averaged source term of the  $j$ -specie by electrochemical reaction:

$$S_{jf} = \varepsilon \langle r_{jf} \rangle_f \quad (\text{II-21})$$

The demonstration can be found in Appendix B.

### 3.6 Local Volume-Averaged Momentum Equation

The local momentum conservation is expressed by considering the following equation:

$$\frac{\partial}{\partial t} [\rho_f \underline{\underline{V}}_f] + \nabla \cdot [\rho_f \underline{\underline{V}}_f \underline{\underline{V}}_f] = \nabla \cdot \underline{\underline{T}}_f + \rho_f \underline{\underline{g}} \quad (\text{II-22})$$

where  $\underline{\underline{g}}$  is the gravitational acceleration vector and  $\underline{\underline{T}}_f$ , the stress tensor defined by:

$$\underline{\underline{T}}_f = \underline{\underline{\tau}}_f - p_f \underline{\underline{I}} \quad (\text{II-23})$$

where  $\underline{\underline{\tau}}_f$  is the viscous stress tensor,  $p_f$ , the fluid-phase pressure and  $\underline{\underline{I}}$ , the identity tensor. Now substituting in Eq. (II-22) for  $\underline{\underline{T}}_f$  using Eq. (II-23), the following local momentum equation is obtained:

$$\frac{\partial}{\partial t} [\rho_f \underline{\underline{V}}_f] + \nabla \cdot [\rho_f \underline{\underline{V}}_f \underline{\underline{V}}_f] = -\nabla p_f + \nabla \cdot \underline{\underline{\tau}}_f + \rho_f \underline{\underline{g}} \quad (\text{II-24})$$

Accumulation of momentum with time is described by the transient term while the second term represents the convection momentum flux. The first two RHS terms of the equation are the

effects of the pressure and viscous stress on momentum, respectively and the third term expresses the gravitational force, which is negligible when considering only gas. When volume averaged, Eq. (II-24) becomes:

$$\frac{\partial}{\partial t} \langle \rho_f \underline{V}_f \rangle + \nabla \cdot \langle \rho_f \underline{V}_f \underline{V}_f \rangle = -\nabla \langle p_f \rangle + \nabla \cdot \langle \tau_f \rangle + \langle \rho_f \rangle \mathbf{g} - \langle d \rangle^{sf} \quad (\text{II-25})$$

where  $\langle d \rangle^{sf}$  is an average term due to the pressure and viscous forces at the solid-fluid interface. This term is complex to understand physically, which makes it even more difficult to find a coherent closure law. A suggestion can be found in [119]. The demonstration can be found in Appendix C. The following constitutive law classically represents the viscous stress tensor:

$$\tau_f = 2\mu_f D_f - \frac{2}{3}\mu_f \nabla \cdot \underline{V}_f \mathbf{I} = \mu_f (\nabla \underline{V}_f + \nabla^T \underline{V}_f) - \frac{2}{3}\mu_f \nabla \cdot \underline{V}_f \mathbf{I} \quad (\text{II-26})$$

where  $\mu_f$  is the fluid-phase dynamic viscosity and  $D_f$ , the fluid-phase rate of strain tensor. The last and the penultimate terms represent the shear and the compression rates – expansion or contraction –, respectively. By substituting Eq. (II-26) for  $\tau_f$  in Eq. (II-25), we have:

$$\begin{aligned} \frac{\partial}{\partial t} \langle \rho_f \underline{V}_f \rangle + \nabla \cdot \langle \rho_f \underline{V}_f \underline{V}_f \rangle \\ = -\nabla \langle p_f \rangle + \nabla \cdot [\mu_f (\nabla \langle \underline{V}_f \rangle + \nabla^T \langle \underline{V}_f \rangle)] - \frac{2}{3} \nabla [\mu_f \nabla \cdot \langle \underline{V}_f \rangle] + \langle \rho_f \rangle \mathbf{g} \\ - \langle d \rangle^{sf} \end{aligned} \quad (\text{II-27})$$

Reynolds' decomposition is needed to determine the average convective term, which cannot be expressed with only the Favre average. The local fluid velocity by applying Reynolds' decomposition including the Favre averaging is:

$$\underline{V}_f = \overline{\underline{V}_f}^f + \underline{V}_f'' \quad (\text{II-28})$$

where  $\underline{V}_f''$  is the fluid-phase fluctuating velocity. By applying the Favre averaging to the product of the fluid-phase velocities:

$$\overline{\underline{V}_f \underline{V}_f}^f = \overline{\underline{V}_f}^f \overline{\underline{V}_f}^f + \overline{\underline{V}_f'' \underline{V}_f''}^f \quad (\text{II-29})$$

where the Favre average of the fluctuating velocity is zero ( $\overline{\underline{V}_f''}^f = 0$ ) since the fluctuating part is defined as the quantity deviation from the Favre average. However, the Favre average of a product of fluctuating quantities is not zero ( $\overline{\underline{V}_f'' \underline{V}_f''}^f \neq 0$ ). Moreover, the Favre average verifies the following property: the average of a product of averaged quantities is the product of these quantities. The mathematical formulation leads to:

$$\overline{\overline{\underline{V}_f}^f \overline{\underline{V}_f}^f}^f = \overline{\underline{V}_f}^f \overline{\underline{V}_f}^f \quad (\text{II-30})$$

By using Eqs. (II-28) and (II-29), Eq. (II-27) becomes:

$$\begin{aligned} \frac{\partial}{\partial t} \left[ \varepsilon \langle \rho_f \rangle_f \overline{\underline{V}_f}^f \right] + \nabla \cdot \left[ \varepsilon \langle \rho_f \rangle_f \overline{\underline{V}_f}^f \overline{\underline{V}_f}^f \right] + \nabla \cdot \left[ \varepsilon \langle \rho_f \rangle_f \overline{\underline{V}_f'' \underline{V}_f''}^f \right] \\ = -\nabla [\varepsilon \langle p_f \rangle_f] + \nabla \cdot \left[ \varepsilon \mu_f \left( \nabla \overline{\underline{V}_f}^f + \nabla^T \overline{\underline{V}_f}^f \right) \right] - \frac{2}{3} \nabla \left[ \mu_f \nabla \cdot \overline{\underline{V}_f}^f \right] \\ + \varepsilon \langle \rho_f \rangle_f g - \langle d \rangle^{sf} \end{aligned} \quad (\text{II-31})$$

The momentum equation is relatively complex even for a single-fluid flow with the appearance of deviation and parietal terms when the local volume-average is applied.

### 3.7 Darcy's Law

Momentum equation is generally reduced to Darcy's law in porous media, which was first experimentally determined by Darcy [121]. This law has since been theoretically refined from the N-S momentum equation by Whitaker [122] for a single-phase flow by considering a Stokes flow where viscous forces are dominant over inertial forces. Furthermore, the dilatation is neglected and the fluid-velocity gradient is assumed symmetrical ( $\nabla \langle \underline{V}_f \rangle = \nabla^T \langle \underline{V}_f \rangle$ ). The theoretical development using transformation tensor<sup>6</sup> leads to the local intrinsic-average Darcy's law:

<sup>6</sup> Transformation tensor is a closure method to relate the fluctuating quantities (at the microscopic scale) to the averaged quantities.

$$\overline{\underline{V}}_f = -\frac{K}{\varepsilon \mu_f} (\nabla \langle p_f \rangle_f - \langle \rho_f \rangle_f \mathbf{g}) \quad (\text{II-32})$$

where  $K$  is the absolute permeability tensor. The permeability is the measure of the flow conductance of the porous matrix, i.e. its ability to allow fluids to pass through it. It is a key parameter in the fluids mechanic through a porous medium. The permeability, defined on the total volume, is dependent on the geometry, the porosity and the size of the pores. Many authors have studied permeability, which is most often obtained empirically. Phillips et al. [123] and Taira and Liu [124] used in-situ measurements to obtain the permeability in GDLs. Gostick et al. [125] found strongly anisotropic properties for several commercial GDLs by measuring in three perpendicular directions. Note that the Darcy's law is affected by a  $1/\varepsilon$  factor compared to its classic formulation. Indeed, the Darcy's law is traditionally presented in the form of the local volume-average velocity:

$$\langle \underline{V}_f \rangle = -\frac{K}{\mu_f} (\nabla \langle p_f \rangle_f - \langle \rho_f \rangle_f \mathbf{g}) \quad (\text{II-33})$$

Finally, Darcy's law represents linear losses when the gravitational force is neglected due to microscopic viscous shear stresses. As only gas is considered, the gravitational force is neglected in the one-fluid model (see Chapter III).

### 3.8 Local Volume-Averaged Energy Conservation Equation

The local continuity equation for energy in PEMFC considering a single-fluid flow is:

$$\frac{\partial}{\partial t} [\rho_f c_{p_f} T_f] + \nabla \cdot [\rho_f c_{p_f} \underline{V}_f T_f] = -\nabla \cdot \mathbf{Q}_f \quad (\text{II-34})$$

where  $T_f$  is the fluid-phase temperature,  $\mathbf{Q}_f$ , the fluid-phase thermal diffusive flux. When volume averaged by introducing the Fick's law to represent the diffusion flux, Eq. (II-34) becomes:

$$\frac{\partial}{\partial t} [\varepsilon \langle \rho_f \rangle_f c_{p_f} \overline{\overline{T}}_f] + \nabla \cdot [\varepsilon \langle \rho_f \rangle_f c_{p_f} \overline{\underline{V}}_f \overline{\overline{T}}_f] = \nabla \cdot [k_f^{\text{eff}} \nabla \overline{\overline{T}}_f] \quad (\text{II-35})$$

where  $k_f^{\text{eff}}$  is the effective fluid-phase thermal conductivity. The demonstration can be found in

[51].

## 4. Two-Phase Flow

The importance of water management and its transport within PEM fuel cells was previously discussed. As a reminder, liquid water can be formed since the gases can become saturated by water vapor production and reactants consumption by the electrochemical reactions. Consequently, water condenses. In addition, significant water transport mechanisms occur between the anode and cathode as presented in Chapter I. Therefore, a two-phase flow must be considered in both side, characterized by the presence of two distinct phases, which are the liquid water and gas mixture. When compared to a single-phase flow, the liquid-gas interface must be carefully examined for a two-phase flow. Indeed, there are wall exchange at the solid-liquid interface as well as at the solid-gas interface (sorption phenomena) but also fluid-fluid exchanges occur on the liquid-gas interface, due to thermal and mechanical non-equilibrium between the fluid phases. In this section, the local averaged continuity equations for a two-phase flow through a porous media are described. Before averaging the equations, some more definitions and theorems are needed.

### 4.1.1 Multiphase Medium

For a two-phase flow in PEM fuel cells, the fluid volume is the volume occupied by both the liquid and gas phase:

$$V_f \stackrel{\text{def}}{=} \sum_{k \neq s} V_k \quad (\text{II-36})$$

where  $V_k$  is the volume associated to the k-phase; the k subscript referring to the liquid or gas phase.

### 4.1.2 k-Phase Volume Fraction

The volume fraction  $\alpha_k$  occupied by the k-phase is the volume of the k-phase divided by the total fluid volume:

$$\alpha_k \stackrel{\text{def}}{=} \frac{V_k}{\sum_{k \neq s} V_k} = \frac{V_k}{V_f} = \frac{V_k}{\varepsilon V} \quad (\text{II-37})$$

The liquid volume fraction is called saturation in the rest of this work. The sum of the k-phase volume fractions is equal to 1:

$$\sum_{k \neq s} \alpha_k = 1 \quad (\text{II-38})$$

## 4.2 Topological Equations

### 4.2.1 Phase Indicator Function

In order to obtain the averaged equations for a multiphase flow, it is necessary to introduce the Phase Indicator Function (PIF), which is an important function for the averaging theorems first introduced by Gray and Lee [126]. This function takes a value of unity in the k-phase and zero in all other phases:

$$\chi_k \equiv \begin{cases} 1 & \text{in the } k - \text{ phase} \\ 0 & \text{otherwise} \end{cases} \quad (\text{II-39})$$

Gray and Lee [126] derived this function to obtain:

$$\nabla \chi_k = -n_k \delta_I \quad (\text{II-40})$$

where  $n_k$  is the unit normal vector pointing out of the interfaces between the k-phase and the other phases and  $\delta_I$ , the Dirac delta function analyzed and generalized by Lighthill [127].

### 4.2.2 Reynolds Transport Theorem

The following topological – local and instantaneous – equation is necessary to demonstrate the limit form of Leibniz's rule, also called Reynolds' transport theorem:

$$\frac{\partial \chi_k}{\partial t} + \underline{V}_I \cdot \nabla \chi_k = 0 \quad (\text{II-41})$$

where  $\underline{V}_I$  is the microscopic velocity vector of the k-phase interface, which is different from the k-phase velocity. Finally, by using Eqs. (II-39) and (II-40), the Reynolds transport theorem becomes:

$$\langle \chi_k \frac{\partial \psi_k}{\partial t} \rangle = \frac{\partial}{\partial t} \langle \chi_k \psi_k \rangle - \frac{1}{V} \int_{A_{Ik}} \psi_k \underline{V}_I \cdot \mathbf{n}_k \, da \quad (\text{II-42})$$

where  $\psi_k$  represents any quantity associated to the k-phase. Compared to a single-phase fluid, relating the average of the time derivative to the time derivative of the average for a multiphase flow forms an interfacial term between the k-phase and the other fluid phase as a surface integral. Only the interfacial term between the fluid phases is considered since the microscopic k-phase velocities are assumed to be zero at the solid surface. Details can be found in [126].

### 4.3 Mathematical Averages

#### 4.3.1 Local Volume-Average Associated with the k-Phase

The local volume-average associated to the k-phase is defined by:

$$\langle \chi_k \psi_k \rangle \stackrel{\text{def}}{=} \frac{1}{V} \int_V \chi_k \psi_k \, dv = \frac{1}{V} \int_{V_k} \psi_k \, dv \quad (\text{II-43})$$

#### 4.3.2 Local Intrinsic-Average Associated with the k-Phase

The local intrinsic-average associated to the fluid is expressed by:

$$\langle \psi_k \rangle_k \stackrel{\text{def}}{=} \frac{1}{V_k} \int_{V_k} \psi_k \, dv = \frac{1}{\alpha_k V_f} \int_{V_k} \psi_k \, dv = \frac{1}{\varepsilon \alpha_k V} \int_{V_k} \psi_k \, dv \quad (\text{II-44})$$

Similar to a single-fluid, the local intrinsic-average of the k-phase consider the k-phase volume and not the total volume as indicated by the k subscript after the second bracket. The relation

between the local volume-average and the local intrinsic-average is:

$$\langle \chi_k \psi_k \rangle = \varepsilon \alpha_k \langle \psi_k \rangle_k \quad (\text{II-45})$$

where the matrix and other phase volume are taken into account by the porosity and the k-phase volume fraction respectively.

#### 4.4 Theorems

##### 4.4.1 Theorem of the Volume-Average of a Gradient

The relation between the volume-average of a gradient and the gradient of the volume-average in order to obtain the averaged equations for a two-phase flow is:

$$\langle \chi_k \nabla \psi_k \rangle = \nabla \langle \chi_k \psi_k \rangle + \frac{1}{V} \int_{A_{Ik}} \psi_k n_k da \quad (\text{II-46})$$

where  $A_{Ik}$  is the interface area between the k-phase and the others phases. The last RHS term represents the discontinuity on the interface area  $A_{Ik}$ , i.e. at the interface liquid-gas but also at the liquid-solid and gas-solid interfaces.

##### 4.4.2 Theorem of the Volume-Average of a Divergence

Similarly, the relation between the volume-average of a divergence and the divergence of the volume-average is needed:

$$\langle \chi_k \nabla \cdot \psi_k \rangle = \nabla \cdot \langle \chi_k \psi_k \rangle + \frac{1}{V} \int_{A_{Ik}} \psi_k \cdot n_k da \quad (\text{II-47})$$

#### 4.5 Local Volume-Averaged Mass Equation

The local continuity equation for the k-phase is given by:

$$\frac{\partial \rho_k}{\partial t} + \nabla \cdot (\rho_k \underline{V}_k) = r_k \quad (\text{II-48})$$

where  $\rho_k$  is the k-phase density,  $\underline{V}_k$ , the k-phase velocity vector and  $r_k$ , the mass source of the k-phase by chemical reaction, i.e. production and consumption. When multiplied by  $\chi_k$  and volume averaged, it becomes:

$$\frac{\partial}{\partial t} \langle \chi_k \rho_k \rangle + \nabla \cdot \langle \chi_k \rho_k \underline{V}_k \rangle = \langle \chi_k r_k \rangle + \Gamma_k^{\text{lk}} \quad (\text{II-49})$$

By defining the mass transfer due to phase change – evaporation or condensation– as following:

$$\Gamma_k^{\text{lk}} = \frac{1}{V} \int_{A_{\text{lk}}} \dot{m}_k \, da = \frac{1}{V} \int_{A_{\text{lk}}} \rho_k (\underline{V}_l - \underline{V}_k) \cdot \underline{n}_k \, da \quad (\text{II-50})$$

where  $\dot{m}_k$  is the mass gain of k-phase per unit interfacial surface. The term is defined so that what one phase gains is lost by the other. By intrinsic and Favre averaging, Eq. (II-49) becomes:

$$\frac{\partial}{\partial t} [\varepsilon \alpha_k \langle \rho_k \rangle_k] + \nabla \cdot [\varepsilon \alpha_k \langle \rho_k \rangle_k \overline{\underline{V}_k^k}] = S_k + \Gamma_k^{\text{lk}} \quad (\text{II-51})$$

where  $S_k$  is the volume-averaged source term by electrochemical reaction:

$$S_k = \varepsilon \alpha_k \langle r_k \rangle_k \quad (\text{II-52})$$

#### 4.6 Local Volume-Averaged Species Mass Conservation Equation

The local species mass conservation equation is:

$$\frac{\partial}{\partial t} [\rho_k Y_{jk}] + \nabla \cdot [\rho_k Y_{jk} \underline{V}_{jk}] = r_{jk} \quad j = 1, N_k \quad (\text{II-53})$$

where the  $jk$  subscript indicates the  $j$ -specie in the  $k$ -phase.  $N_k$  is the number of species in the  $k$ -phase,  $Y_{jk}$ , the mass fraction of the  $j$ -specie in the  $k$ -phase,  $\underline{V}_{jk}$ , the velocity vector of the  $j$ -specie in the  $k$ -phase and  $r_{jk}$ , the mass source of the  $j$ -specie in the  $k$ -phase by electrochemical reaction – production or consumption. As for a single-phase flow, a diffusive flux is introduced to take into account for the difference between the  $j$ -specie and  $k$ -phase velocities:

$$j_{jk} \stackrel{\text{def}}{=} \rho_k Y_{jk} (\underline{V}_{jk} - \underline{V}_k) \quad (\text{II-54})$$

The local mass conservation equation becomes:

$$\frac{\partial}{\partial t} [\rho_k Y_{jk}] + \nabla \cdot [\rho_k Y_{jk} \underline{V}_k] = -\nabla \cdot j_{jk} + r_{jk} \quad (\text{II-55})$$

When volume averaged, Eq. (II-55) is written:

$$\frac{\partial}{\partial t} \langle \chi_k \rho_{jk} \rangle + \nabla \cdot \langle \chi_k \rho_{jk} \underline{V}_k \rangle = \nabla \cdot [D_{m_j} \nabla \langle \chi_k \rho_{jk} \rangle] + S_{jk} + \Gamma_{jk}^{\text{Ik}} + S_{jk}^{\text{Ik}} \quad (\text{II-56})$$

where  $S_{jk}$  is the volume-averaged source term of the  $j$ -specie in the  $k$ -phase by electrochemical reaction,  $\Gamma_{jk}^{\text{Ik}}$ , the mass transfer due to phase change and  $S_{jk}^{\text{Ik}}$ , the sorption phenomenon. With intrinsic and Favre averaging, Eq. (II-56) becomes:

$$\begin{aligned} \frac{\partial}{\partial t} [\varepsilon \alpha_k \langle \rho_{jk} \rangle_k] + \nabla \cdot [\varepsilon \alpha_k \langle \rho_{jk} \rangle_k \overline{\underline{V}}_k] \\ = \nabla \cdot [D_{m_j} \nabla (\varepsilon \alpha_k \langle \rho_{jk} \rangle_k)] + S_{jk} + \Gamma_{jk}^{\text{Ik}} + S_{jk}^{\text{Ik}} \end{aligned} \quad (\text{II-57})$$

#### 4.7 Local Volume-Averaged Momentum Equation

The local momentum equation for a two-phase flow is:

$$\frac{\partial}{\partial t} [\rho_k \underline{V}_k] + \nabla \cdot [\rho_k \underline{V}_k \underline{V}_k] = -\nabla p_k + \nabla \cdot \tau_k + \rho_k \mathbf{g} \quad (\text{II-58})$$

where  $\tau_k$  is the viscous stress tensor and  $p_k$ , the  $k$ -phase pressure. When volume averaged, the

momentum equation becomes:

$$\begin{aligned}
 \frac{\partial}{\partial t} \langle \chi_k \rho_k \underline{V}_k \rangle + \nabla \cdot \langle \chi_k \rho_k \underline{V}_k \underline{V}_k \rangle \\
 = -\nabla \langle \chi_k p_k \rangle - \frac{1}{V} \int_{A_{Ik}} p_k \mathbf{n}_k \, da + \nabla \cdot \langle \chi_k \boldsymbol{\tau}_k \rangle + \frac{1}{V} \int_{A_{Ik}} \boldsymbol{\tau}_k \cdot \mathbf{n}_k \, da \\
 + \langle \chi_k \rho_k \mathbf{g} \rangle + \Gamma_k^{\text{Ik}} \underline{V}_\Gamma
 \end{aligned} \quad (\text{II-59})$$

With

$$\Gamma_k^{\text{Ik}} \underline{V}_\Gamma = \frac{1}{V} \int_{A_{Ik}} \dot{m}_k \underline{V}_k \, da = \frac{1}{V} \int_{A_{I,k}} \rho_k \underline{V}_k \underline{V}_I \cdot \mathbf{n}_k \, da - \frac{1}{V} \int_{A_{Ik}} \rho_k \underline{V}_k \underline{V}_k \cdot \mathbf{n}_k \, da \quad (\text{II-60})$$

where  $\underline{V}_\Gamma$  is the average velocity vector weighted by the phase change, which is common to both phases so that the momentum transfer between the phases does not create or destroy momentum in the fluid mixture. Finally,  $\Gamma_k^{\text{Ik}} \underline{V}_\Gamma$  represents a momentum exchange between the fluid phases when there is evaporation or condensation. The following constitutive law for the viscous stress tensor is introduced:

$$\boldsymbol{\tau}_k = 2\mu_k D_k - \frac{2}{3}\mu_k \nabla \cdot \underline{V}_k \mathbf{I} = \mu_k (\nabla \underline{V}_k + \nabla^T \underline{V}_k) - \frac{2}{3}\mu_k \nabla \cdot \underline{V}_k \mathbf{I} \quad (\text{II-61})$$

where  $\mu_k$  is the k-phase dynamic viscosity and  $D_k$ , the k-phase strain tensor. Similar to a single-phase flow,  $\mu_k (\nabla \underline{V}_k + \nabla^T \underline{V}_k)$  represents the shear rate and  $-\frac{2}{3}\mu_k \nabla \cdot \underline{V}_k \mathbf{I}$ , the compression rate (expansion or contraction). The compression rate is zero for the liquid phase, assumed incompressible. The volume-averaged momentum equation becomes:

$$\begin{aligned}
 & \frac{\partial}{\partial t} \langle \chi_k \rho_k \underline{V}_k \rangle + \nabla \cdot \langle \chi_k \rho_k \underline{V}_k \underline{V}_k \rangle \\
 &= -\nabla \langle \chi_k p_k \rangle - \frac{1}{V} \int_{A_{Ik}} p_k n_k da + \nabla \cdot [\mu_k (\chi_k \nabla \langle \underline{V}_k \rangle + \chi_k \nabla^T \langle \underline{V}_k \rangle)] \\
 &+ \frac{\mu_k}{V} \int_{A_{Ik}} (\nabla \underline{V}_k + \nabla^T \underline{V}_k) \cdot n_k da + \nabla \cdot \left( \frac{\mu_k}{V} \int_{A_{Ik}} (\underline{V}_k n_k + n_k \underline{V}_k) da \right) \quad (\text{II-62}) \\
 &- \frac{2}{3} \nabla [\mu_k \chi_k \nabla \cdot \langle \underline{V}_k \rangle] - \frac{2}{3} \left( \mu_k \int_{A_{Ik}} \nabla \underline{V}_k \cdot n_k da \right) \\
 &- \frac{2}{3} \nabla \left( \frac{\mu_k}{V} \int_{A_{Ik}} \underline{V}_k \cdot n_k da \right) + \langle \chi_k \rho_k g \rangle + \Gamma_k^{Ik} \underline{V}_\Gamma
 \end{aligned}$$

with intrinsic and Favre averages, Eq. (II-62) can be rewritten:

$$\begin{aligned}
 & \frac{\partial}{\partial t} [\varepsilon \alpha_k \langle \rho_k \rangle_k \overline{\underline{V}_k^k}] + \nabla \cdot [\varepsilon \alpha_k \langle \rho_k \rangle_k \overline{\underline{V}_k^k} \overline{\underline{V}_k^k}] + \nabla \cdot [\varepsilon \alpha_k \langle \rho_k \rangle_k \overline{\underline{V}_k^k} \underline{V}_k^{\prime\prime k}] \\
 &= -\nabla [\varepsilon \alpha_k \langle p_k \rangle_k] - \frac{1}{V} \int_{A_{Ik}} p_k n_k da + \nabla \\
 &\cdot [\mu_k \varepsilon \alpha_k (\nabla \overline{\underline{V}_k^k} + \nabla^T \overline{\underline{V}_k^k})] + \frac{\mu_k}{V} \int_{A_{Ik}} (\nabla \underline{V}_k + \nabla^T \underline{V}_k) \cdot n_k da + \nabla \\
 &\cdot \left( \frac{\mu_k}{V} \int_{A_{Ik}} (\underline{V}_k n_k + n_k \underline{V}_k) da \right) - \frac{2}{3} \nabla [\mu_k \varepsilon \alpha_k \nabla \cdot \overline{\underline{V}_k^k}] \\
 &- \frac{2}{3} \left( \mu_k \int_{A_{Ik}} \nabla \underline{V}_k \cdot n_k da \right) - \frac{2}{3} \nabla \left( \frac{\mu_k}{V} \int_{A_{Ik}} \underline{V}_k \cdot n_k da \right) + \varepsilon \alpha_k \langle \rho_k \rangle_k g \\
 &+ \Gamma_k^{Ik} \underline{V}_\Gamma \quad (\text{II-63})
 \end{aligned}$$

where  $\underline{V}_k^{\prime\prime}$  is the k-phase fluctuating velocity vector and  $\overline{\quad}^k$ , the Favre averaging as explained in the single-phase flow section but applied to the k-phase. The Reynolds' decomposition is used in Eq. (II-63) to replace the average of the product by the product of the averages:

$$\underline{V}_k = \overline{\underline{V}_k^k} + \underline{V}_k^{\prime\prime} \quad (\text{II-64})$$

$$\overline{\underline{V}_k \underline{V}_k}^k = \overline{\underline{V}_k}^k \overline{\underline{V}_k}^k + \overline{\underline{V}_k'' \underline{V}_k''}^k \quad (\text{II-65})$$

with  $\overline{\underline{V}_k''}^k = 0$  by definition. Finally, the local intrinsic momentum equation is complex due to the numerous terms of exchange between the fluid phases. It is difficult to understand correctly the phase transfer mechanisms described by its terms, which makes it all the more difficult to find the adequate closure laws. It should also be noted that these terms are frequently sources of numerical instabilities. For more details, Slattery [128], Whitaker [122][129], Gray [130], Bear and Bensabat [131], Hassanizadeh and Gray [132]-[133], and Gray and Hassanizadeh [134] examined the volume averaging of the continuity equations for a two-phase flow through a porous media. It is therefore necessary to simplify this equation by introducing the extension of Darcy's law for a two-phase flow.

#### 4.8 The Extended Two-Phase Darcy's Law

As for a single-phase, a Stokes flow, a negligible dilation and a symmetric gradient of the  $k$ -phase velocity ( $\nabla \langle \underline{V}_k \rangle = \nabla^T \langle \underline{V}_k \rangle$ ) are assumed in the local intrinsic-average momentum equation in order to demonstrate the extended two-phase Darcy's law. Furthermore, Whitaker [122][129] introduced transformation tensors and vectors to express the fluctuating quantities as a function of the average quantities. This approach has been discussed at length in [51]. This method remains arbitrary but allows to « theoretically » obtain the extended two-phase Darcy's law:

$$\overline{\underline{V}_k}^k = -\frac{K K_{rk}}{\varepsilon \alpha_k \mu_k} [\nabla \langle p_k \rangle_k - \langle \rho_k \rangle_k \mathbf{g}] \quad (\text{II-66})$$

where  $K$  is the absolute permeability already discussed in the single-phase flow section and  $K_{rk}$ , the relative permeability of the  $k$ -phase. The relative permeabilities represent the phase distributions and their influence on each other. This parameter alone expresses most of the exchange terms at the liquid-gas interface present in the local intrinsic-average momentum equation. From another point of view, the effect of the microscopic shear stress (both pressure and viscous effect), the interfacial drag at  $A_{lk}$  and the Marangoni effect are all included in the relative permeabilities. Therefore, it can be expected that  $K_{rk}$  depends on the viscosity, density and

velocity ratios because of significant difference between the liquid and gas phase quantities. However, it is difficult to adequately express the relative permeability since it is affected by many parameters. Muskat and Meres [135] were the first to discuss the relative permeability. They introduce a simplifying relation to a saturation dependence only. This empirical model is still widely discussed and used today:

$$K_{rk} = \alpha_k^{n_k} \quad (\text{II-67})$$

where  $n_k$  is a key parameter, which generally takes values between 2 and 5. A value of 3 for this exponent is commonly used. Relative permeability has been studied at length by Brooks and Corey [136]. They proposed a theoretical model depending on saturation and compared it with experimental measurements. However, their models are not necessarily suitable for a PEM fuel cell. More recently, Hussaini and Wang [137] measure air and water relative permeabilities as a function of saturation for several commercial GDL materials. They establish new saturation-dependent correlations for in-plane relative permeability of water and air. Finally,  $n_k$  parameter has an important influence on the phase velocities and therefore significantly impact the liquid water distribution. A sensitivity study to this coefficient is presented in Appendix G:  $n_k$  Coefficient Sensitivity Study (from 2 to 5). The gravitational force is neglected in the two-fluid model (see Chapter IV).

## Conclusion

As a complex multilayers and multiphysics system, the theoretical physics in PEMFCs are still widely studied. Indeed, all the processes such as electrochemical reactions, thermofluid dynamic flow and phase change are strongly coupled and dependent on the operating conditions, the component design and material properties. Therefore, the theory of thermofluid mechanics in PEM fuel cells was examined in this chapter. The continuity equations of mass, species mass, momentum and energy were reviewed from the local and instantaneous equations for a single-phase and two-phase flow. The local volume-averaging method over the Representative Elementary Volume was applied to upscale the conservation equations in porous media. In addition, Darcy's law was introduced as a reduced formulation of the momentum equation for the porous layers as well as the gas channels by considering a tortuosity and porosity equal to the unit.

**Chapter III**  
**ONE-FLUID MODEL**

## Introduction

In this chapter, the one-fluid (1-F) PEMFC model is presented considering a single-phase flow. The transport equations, detailed in Chapter III, are coupled to a semi-empirical electrochemical model. The cooling circuit is also represented by the model. The pseudo-3D (P3D) approach is applied by considering each cell component as a plane layer. The model was previously developed and validated for temperatures and current density by comparison with Current Scan Lin S++ measurements [138]. In this study, a particular condensation model is implemented, which calculates the amount of condensed water vapor, to numerically investigate the liquid water distribution in the different cell components. The condensation model is confronted with a classical phase-separated flow model [139] in order to examine its validity range. The model has been implemented in the commercial COMSOL Multiphysics® software for all the cell layers of a large surface PEM fuel cell. The geometry of the stack is presented in this chapter. In addition, a sensitivity study is performed to analyze some important parameters in the modeling of water transport mechanisms detailed in Chapter I. Finally, the numerical water distribution is examined and discussed at the cell and rib/channel scales by comparison with liquid water neutron imaging. The experimental method is detailed in Appendix E.

### 1. Pseudo-3D Formulation

As discussed previously, PEM fuel cells are multiphysics and multi-component systems with strong interdependencies on temperature, current density and water content. On one hand, a 3D model seems required to represent all the interactions between the components. On the other hand, full 3D models still require too much computational resources and time, especially when the operation of a large area FC must be simulated. The 3D models developed are therefore limited to reduced cell geometries such as a single straight channel or considered more or less significant assumptions like isothermal process or single-phase transport. The pseudo-3D approach is then used in the model in order to simulate a large surface cell while keeping the real design of the bipolar plates with a reasonable computing time.

## 2. Principle

Each component of a cell in any PEMFCs has a very small thickness, usually between 5 and 400  $\mu\text{m}$ , compared to its length and width. The aspect ratio between the thickness and other dimensions is then low ( $1 \cdot 10^{-5} - 1 \cdot 10^{-2}$ ) for the majority of components in PEM fuel cells. Therefore, it seems appropriate to consider each component as a plane layer (Fig. III-1). Consequently, each layer is accurately in-plane discretized to obtain the 2D conservation equations where non-classical source terms appear to represent the flux exchanges between the adjacent components. Finally, the model considers the cell as a multilayered system and becomes the pseudo-3D model by introducing the in-plane variables, which are averaged values along the component thickness.

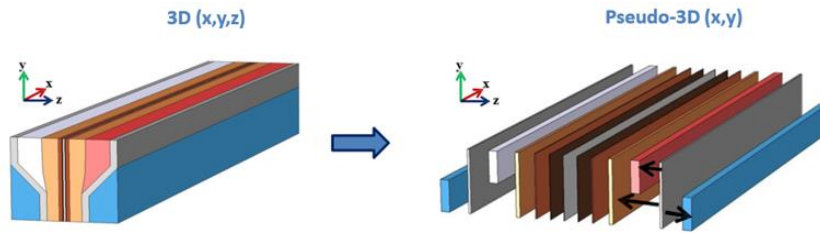


Fig. III-1. From full 3D to pseudo-3D model – from [37].

### 2.1 Integration Development

The conservation equations are integrated along the component thickness to obtain the P3D formulation for a single-phase flow. The integration of the mass equation leads to:

$$\int_0^e \left( \frac{\partial}{\partial t} [\varepsilon \langle \rho_f \rangle_f] \right) dz + \int_0^e \left( \nabla_{3D} \cdot [\varepsilon \langle \rho_f \rangle_f \overline{\mathbf{V}}_f^f] \right) dz = \int_0^e S_f dz \quad (\text{III-1})$$

where  $e$  is the component thickness. The differential operator  $\nabla_{3D}$  and the fluid-velocity vector  $\overline{\mathbf{V}}_f^f$  are decomposed into the three-dimensional Cartesian coordinate system to obtain:

$$\int_0^e \left( \frac{\partial}{\partial t} [\varepsilon \langle \rho_f \rangle_f] \right) dz + \int_0^e \left( \frac{\partial}{\partial x} [\varepsilon \langle \rho_f \rangle_f \overline{u}_f^f] + \frac{\partial}{\partial y} [\varepsilon \langle \rho_f \rangle_f \overline{v}_f^f] + \frac{\partial}{\partial z} [\varepsilon \langle \rho_f \rangle_f \overline{w}_f^f] \right) dz = S_f e \quad (\text{III-2})$$

where  $\overline{\overline{u}}_f^f$ ,  $\overline{\overline{v}}_f^f$  and  $\overline{\overline{w}}_f^f$  are the Favre-average fluid-phase velocity according to x, y, and z directions, respectively. The electrochemical source term  $S_f$  is considered constant over the thickness. Furthermore, the integrals are swapped with the differential operators. Finally, each term is divided by the component thickness leading to:

$$\begin{aligned} \frac{\partial}{\partial t} \left( \frac{1}{e} \int_0^e [\varepsilon \langle \rho_f \rangle_f] dz \right) + \frac{\partial}{\partial x} \left( \frac{1}{e} \int_0^e [\varepsilon \langle \rho_f \rangle_f \overline{\overline{u}}_f^f] dz \right) + \frac{\partial}{\partial y} \left( \frac{1}{e} \int_0^e [\varepsilon \langle \rho_f \rangle_f \overline{\overline{v}}_f^f] dz \right) \\ + \frac{1}{e} \left[ \varepsilon \langle \rho_f \rangle_f \overline{\overline{w}}_f^f \right]_0^e = S_f \end{aligned} \quad (\text{III-3})$$

As a reminder, the porosity is assumed constant over the entire volume. Under this assumption, we have:

$$\frac{1}{e} \int_0^e [\varepsilon \langle \rho_f \rangle_f] dz = \varepsilon \frac{1}{e} \int_0^e \langle \rho_f \rangle_f dz \quad (\text{III-4})$$

$$\frac{1}{e} \int_0^e [\varepsilon \langle \rho_f \rangle_f \overline{\overline{u}}_f^f] dz = \varepsilon \frac{1}{e} \int_0^e \langle \rho_f \rangle_f \overline{\overline{u}}_f^f dz \quad (\text{III-5})$$

$$\frac{1}{e} \int_0^e [\varepsilon \langle \rho_f \rangle_f \overline{\overline{v}}_f^f] dz = \varepsilon \frac{1}{e} \int_0^e \langle \rho_f \rangle_f \overline{\overline{v}}_f^f dz \quad (\text{III-6})$$

where the local thickness-average  $\frac{1}{e} \int_0^e \psi dz$  can be recognized. Considering a small thickness, the average of a product is equal to the product of the averages since the fluid-density and velocities according to x and y directions are considered constant over the thickness. In other words, the in-plane fluid-velocity, also called filter velocity, is assumed uniform, which means the through-plane fluctuating velocity is zero by neglecting the through-plane profile effects. Finally, the pseudo-3D description for the mass equation is expressed by:

$$\frac{\partial}{\partial t} [\varepsilon \langle \rho_f \rangle_{f,e}] + \nabla_{2D} \cdot [\varepsilon \langle \rho_f \rangle_{f,e} \overline{\overline{\mathbf{v}}}_{f,e}^f] + \frac{J_{\text{conv}}^+}{e} + \frac{J_{\text{conv}}^-}{e} = S_f \quad (\text{III-7})$$

where the e subscript refers to an in-plane variable,  $\overline{\underline{V}}_{f,e}^f = \overline{\underline{u}}_f^f \underline{e}_x + \overline{\underline{v}}_f^f \underline{e}_y$ , the in-plane fluid-velocity with  $\underline{e}_x$  and  $\underline{e}_y$ , the unit vectors of the x and y axes, respectively.  $J_{\text{conv}}^+$  and  $J_{\text{conv}}^-$  are the convective mass-fluxes across the interfaces of the different components described by:

$$\frac{J_{\text{conv}}^+}{e} = \frac{1}{e} \varepsilon \langle \rho_f \rangle_f \overline{\underline{w}}_f^f \Big|_e \quad (\text{III-8})$$

$$\frac{J_{\text{conv}}^-}{e} = -\frac{1}{e} \varepsilon \langle \rho_f \rangle_f \overline{\underline{w}}_f^f \Big|_0 \quad (\text{III-9})$$

The same development is applied to the species (III-10) and energy (III-11) conservation equations:

$$\begin{aligned} \frac{\partial}{\partial t} [\varepsilon \langle \rho_{jf} \rangle_{f,e}] + \nabla_{2D} \cdot [\varepsilon \langle \rho_{if} \rangle_{f,e} \overline{\underline{V}}_{f,e}^f] + \frac{J_{\text{conv},j}^+}{e} + \frac{J_{\text{conv},j}^-}{e} \\ = \nabla_{2D} \cdot [D_{mj} \nabla_{2D} (\varepsilon \langle \rho_{if} \rangle_{f,e})] + \frac{J_{\text{diff},j}^+}{e} + \frac{J_{\text{diff},j}^-}{e} + S_{jf} \end{aligned} \quad (\text{III-10})$$

$$\begin{aligned} \frac{\partial}{\partial t} [\varepsilon \langle \rho_f \rangle_{f,e} c_{pf} \overline{\underline{T}}_{f,e}^f] + \nabla_{2D} \cdot [\varepsilon \langle \rho_f \rangle_{f,e} c_{pf} \overline{\underline{V}}_{f,e}^f \overline{\underline{T}}_{f,e}^f] + \frac{J_{\text{conv},T}^+}{e} + \frac{J_{\text{conv},T}^-}{e} \\ = \nabla \cdot [k_f^{\text{eff}} \nabla_{2D} (\varepsilon \overline{\underline{T}}_{f,e}^f)] + \frac{J_{\text{diff},T}^+}{e} + \frac{J_{\text{diff},T}^-}{e} \end{aligned} \quad (\text{III-11})$$

where the same assumptions are retained for these equations as for the mass balance. Other assumptions are needed in the pseudo-3D writing of species and energy equations. The variations of the mass diffusion coefficient and thermal conductivity  $D_{mj}$  and  $k_f^{\text{eff}}$  are assumed negligible over the volume in the same way as the variation of the temperature over thickness. Similar to the convective mass-fluxes across the interfaces of the different components,  $J_{\text{diff},j}^+$ ,  $J_{\text{diff},j}^-$  and  $J_{\text{diff},T}^+$ ,  $J_{\text{diff},T}^-$  represent the through-plane diffusive mass-fluxes of the j-specie and through-plane thermal-fluxes when the diffusion transport is described by the P3D formulation. More details can be found in [37][138] and Appendix I.

## 2.2 Advantages and Limitations

The pseudo-3D model predicts the distributions of current density, species concentrations, water content and temperature in all the components of the cell with a lower computation time compared to a full 3D model, while representing the real flow-field design. Rizvandi and Yezilyurt [140] developed both full 3D and P3D models in order to compare the Degrees of Freedom (DOF), CPU time, and the required RAM. They concluded that the P3D model is about 40 times faster than the full 3D model, while keeping consistent results. From a numerical point of view, the P3D model is identical to a full 3D model with only one mesh element in its thickness. Nevertheless, some z-information are lost with the P3D model by considering constant variables over the thickness. Other models are needed to capture all the heterogeneities over the three dimensions such as the pore network model, which is not suitable at the scale of a large area cell as discussed in Chapter I.

## 3. One-Fluid Equations

This section presents the P3D transport and electrochemical equations implemented in COMSOL Multiphysics®. In addition, the source terms are detailed for all the layers including the mathematical formulation of the water transport mechanisms through the membrane already introduced in Chapter I. Finally, the condensation model is presented to investigate the thickness of liquid water in each component of the cell.

### 3.1 Geometrical Domain

#### 3.1.1 Gas Channels and Gas Diffusion Electrodes

The conservation equations for mass (III-7) and species (III-10) for a single-phase flow with the P3D formulation are solved on both the anode and cathode side in the gas channels and gas diffusion electrodes (GCs-GDEs). Gas diffusion electrodes consist of the gas diffusion, microporous and catalyst layers (GDL-MPL-CL) to form a single porous medium on each side. The momentum equation is reduced to Darcy's law in the GCs and GDEs. Unlike fluid dynamics solved by considering a single porous medium on each side, the energy equation (III-11) is calculated in GCs and reduced to the conduction heat transfer equation in all porous layers, i.e. considering GDLs, MPLs and CLs. The reference geometry of the pseudo-3D model is presented in Fig. III-4. The physical and geometric values implemented in the one-fluid model are presented in Appendix H.

The mass diffusion coefficient of the  $j$ -specie in (III-10) is generally modified by the Bruggeman correlation to obtain the effective mass diffusion coefficient in order to consider tortuous materials in fuel cells:

$$D_{m_j}^{\text{eff}} = \frac{D_{m_g}}{\tau^n} \quad (\text{III-12})$$

where  $\tau$  is the tortuosity (dimensionless) and  $n$ , the Bruggeman factor (equal to 1.5 in the model). The tortuosity, also called tortuosity factor, represents the geometric complexity of a porous medium. It is usually defined as the ratio between the average length of the curved paths followed by a fluid in a porous medium over a straight path. Ghanbarian et al. [141] reviewed tortuosity in porous media in detail.

### 3.1.2 Cooling Circuit

A classical continuity (III-13) and the semi-heuristic (III-14) equations respectively describe the mass and momentum transport in the cooling water (CW) channels:

$$\nabla_{2D} \cdot \underline{V}_{cw} = 0 \quad (\text{III-13})$$

$$\begin{aligned} \rho_{cw} \frac{\partial}{\partial t} \underline{V}_{cw} + \rho_{cw} (\underline{V}_{cw} \cdot \nabla_{2D}) \underline{V}_{cw} \\ = -\nabla_{2D} p_{cw} + \nabla_{2D} \cdot [\mu_{cw} (\nabla_{2D} \underline{V}_{cw} + \nabla_{2D}^T \underline{V}_{cw})] - \frac{\mu_{cw}}{K} \underline{V}_{cw} \\ - \frac{1}{K_2} \|\underline{V}_{cw}\| \underline{V}_{cw} + \rho_{cw} \mathbf{g} \end{aligned} \quad (\text{III-14})$$

where  $cw$  denotes the cooling water, which is considered incompressible,  $\underline{V}_{cw}$ , the CW velocity vector and  $K_2$ , the Forchheimer correction tensor. This equation is based on the works of Brinkman, [142], Wooding [143] and Whitaker [122], which is not rigorously demonstrated. This is the semi-heuristic volume-averaged equation to describe the complex flows in the cooling circuit. Indeed, the vacant space between the anode/cathode polar plates forms the cooling circuit in the F-type flow design (Fig. III-4b), which can therefore present chaotic flow zones, clearly identified in [37]. For this reason, additional terms are present in the momentum equation to take into account all complex flow phenomena in a semi-empirical way. The first 3 terms

in Eq. (III-14) respectively represent the inertial unsteady term, macroscopic inertial forces and pressure gradient as already discussed in Chapter II. The second RHS term, also called Brinkman's term, expresses the macroscopic viscous stress. The third RHS term is Darcy's law to represent the linear losses because of microscopic viscous shear stresses. The Forchheimer term (quadratic expression) takes into account the non-linear losses due to the consecutive section changes in the cooling circuit. Indeed, a loss of inertial pressure is caused by the acceleration and deceleration of the cooling fluid as it flows along non-regular pattern. Finally, the last term corresponds to the gravitational force. All the governing equations are summarized in Table III-1.

**Table III-1**

Governing equations

Component	Conservation equation	General form		
GCs	Mass	$\frac{\partial}{\partial t} \langle \rho_f \rangle_{f,e} + \nabla_{2D} \cdot \left[ \langle \rho_f \rangle_{f,e} \overline{\mathbf{V}}_{f,e}^f \right] + \frac{J_{\text{conv}}^+}{e_{\text{GC}}} + \frac{J_{\text{conv}}^-}{e_{\text{GC}}} = S_f$	(A)	
	Momentum	$\overline{\mathbf{V}}_{f,e}^f = -\frac{K_{\text{GC}}}{\mu_f} \nabla_{2D} \langle p_f \rangle_{f,e}$	(B)	
	Species	$\frac{\partial}{\partial t} \langle \rho_{jf} \rangle_{f,e} + \nabla_{2D} \cdot \left[ \langle \rho_{jf} \rangle_{f,e} \overline{\mathbf{V}}_{f,e}^f \right] + \frac{J_{\text{conv},j}^+}{e_{\text{GC}}} + \frac{J_{\text{conv},j}^-}{e_{\text{GC}}} = \nabla_{2D} \cdot \left[ D_{m_j}^{\text{eff}} \nabla_{2D} \langle \rho_{jf} \rangle_{f,e} \right] + \frac{J_{\text{diff},j}^+}{e_{\text{GC}}} + \frac{J_{\text{diff},j}^-}{e_{\text{GC}}}$	(C)	
	Energy	$\frac{\partial}{\partial t} \left[ \langle \rho_f \rangle_{f,e} c_{p_f} \overline{T}_{f,e}^f \right] + \nabla_{2D} \cdot \left[ \langle \rho_f \rangle_{f,e} c_{p_f} \overline{\mathbf{V}}_{f,e}^f \overline{T}_{f,e}^f \right] = \nabla \cdot \left[ k_f^{\text{eff}} \nabla_{2D} \left( \overline{T}_{f,e}^f \right) \right] + \frac{J_{\text{diff},T}^+}{e_{\text{GC}}} + \frac{J_{\text{diff},T}^-}{e_{\text{GC}}}$	(D)	
GDEs	Mass	$\frac{\partial}{\partial t} \left[ \varepsilon_{\text{GDE}} \langle \rho_f \rangle_{f,e} \right] + \nabla_{2D} \cdot \left[ \varepsilon_{\text{GDE}} \langle \rho_f \rangle_{f,e} \overline{\mathbf{V}}_{f,e}^f \right] + \frac{J_{\text{conv}}^+}{e_{\text{GDE}}} + \frac{J_{\text{conv}}^-}{e_{\text{GDE}}} = S_f$	(E)	
	Momentum	$\overline{\mathbf{V}}_{f,e}^f = -\frac{K_{\text{GDE}}}{\varepsilon_{\text{GDE}} \mu_f} \nabla_{2D} \langle p_f \rangle_{f,e}$	(F)	
	Species	$\frac{\partial}{\partial t} \left[ \varepsilon_{\text{GDE}} \langle \rho_{jf} \rangle_{f,e} \right] + \nabla_{2D} \cdot \left[ \varepsilon_{\text{GDE}} \langle \rho_{jf} \rangle_{f,e} \overline{\mathbf{V}}_{f,e}^f \right] + \frac{J_{\text{conv},j}^+}{e_{\text{GDE}}} + \frac{J_{\text{conv},j}^-}{e_{\text{GDE}}} = \nabla_{2D} \cdot \left[ D_{m_j}^{\text{eff}} \nabla_{2D} \left( \varepsilon_{\text{GDE}} \langle \rho_{jf} \rangle_{f,e} \right) \right] + \frac{J_{\text{diff},j}^+}{e_{\text{GDE}}} + \frac{J_{\text{diff},j}^-}{e_{\text{GDE}}} + S_{jf}$	(G)	
	Energy	GDLs	$\frac{\partial}{\partial t} \left[ (1 - \varepsilon_{\text{GDL}}) \rho_{\text{GDL}} c_{p_{\text{GDL}}} \overline{T}_{\text{GDL},e}^{\text{GDL}} \right] - \nabla \cdot \left[ k_{\text{GDL}} \nabla_{2D} \left( (1 - \varepsilon_{\text{GDL}}) \overline{T}_{\text{GDL},e}^{\text{GDL}} \right) \right] = \frac{J_{\text{diff},T}^+}{e_{\text{GDL}}} + \frac{J_{\text{diff},T}^-}{e_{\text{GDL}}} + Q_T$	(H)
		MPLs	$\frac{\partial}{\partial t} \left[ (1 - \varepsilon_{\text{MPL}}) \rho_{\text{MPL}} c_{p_{\text{MPL}}} \overline{T}_{\text{MPL},e}^{\text{MPL}} \right] - \nabla \cdot \left[ k_{\text{MPL}} \nabla_{2D} \left( (1 - \varepsilon_{\text{MPL}}) \overline{T}_{\text{MPL},e}^{\text{MPL}} \right) \right] = \frac{J_{\text{diff},T}^+}{e_{\text{MPL}}} + \frac{J_{\text{diff},T}^-}{e_{\text{MPL}}} + Q_T$	(I)
		CLs	$\frac{\partial}{\partial t} \left[ (1 - \varepsilon_{\text{CL}}) \rho_{\text{CL}} c_{p_{\text{CL}}} \overline{T}_{\text{CL},e}^{\text{CL}} \right] - \nabla \cdot \left[ k_{\text{CL}} \nabla_{2D} \left( (1 - \varepsilon_{\text{CL}}) \overline{T}_{\text{CL},e}^{\text{CL}} \right) \right] = \frac{J_{\text{diff},T}^+}{e_{\text{CL}}} + \frac{J_{\text{diff},T}^-}{e_{\text{CL}}} + Q_T + S_T$	(J)
CW channels	Mass	$\nabla_{2D} \cdot \langle \mathbf{V}_{\text{CW}} \rangle_{f,e} = 0$	(K)	
	Momentum	$\rho_{\text{CW}} \frac{\partial}{\partial t} \langle \mathbf{V}_{\text{CW}} \rangle_{f,e} + \rho_{\text{CW}} (\langle \mathbf{V}_{\text{CW}} \rangle_{f,e} \cdot \nabla_{2D}) \langle \mathbf{V}_{\text{CW}} \rangle_{f,e} = -\nabla_{2D} p_{\text{CW}} + \nabla_{2D} \cdot \left[ \mu_{\text{CW}} (\nabla_{2D} \langle \mathbf{V}_{\text{CW}} \rangle_{f,e} + \nabla_{2D}^T \langle \mathbf{V}_{\text{CW}} \rangle_{f,e}) \right] + \frac{\mu_{\text{CW}}}{K} \langle \mathbf{V}_{\text{CW}} \rangle_{f,e} + \frac{1}{K_2} \ \langle \mathbf{V}_{\text{CW}} \rangle_{f,e}\  \langle \mathbf{V}_{\text{CW}} \rangle_{f,e} + \rho_{\text{CW}} \mathbf{g}$	(L)	
	Energy	$\rho_{\text{CW}} c_{p_{\text{CW}}} \frac{\partial \langle T_{\text{CW}} \rangle_{f,e}}{\partial t} + \nabla_{2D} \cdot \left[ \rho_{\text{CW}} c_{p_{\text{CW}}} \langle \mathbf{V}_{\text{CW}} \rangle_{f,e} \langle T_{\text{CW}} \rangle_{f,e} \right] = \nabla \cdot \left[ k_{\text{CW}}^{\text{eff}} \nabla_{2D} \langle T_{\text{CW}} \rangle_{f,e} \right] + \frac{J_{\text{diff},T}^+}{e_{\text{CW}}} + \frac{J_{\text{diff},T}^-}{e_{\text{CW}}}$	(M)	

### 3.2 Electrochemical Model

The transport equations are coupled to a classical electrochemical model to obtain the current density  $i$ . A uniform cell potential  $U_{\text{cell}}$  is assumed along the cell surface, described by the following equation:

$$U_{\text{cell}} = E_{\text{rev}} + \eta + \eta_{\text{ohm}} \quad (\text{III-15})$$

where  $E_{\text{rev}}$  is the reversible potential,  $\eta$ , the overpotential (both activation and diffusion) and  $\eta_{\text{ohm}}$ , the ohmic losses.

#### 3.2.1 Reversible Potential

The well-known Nernst equation is used to obtain the reversible potential expressed as follows:

$$E_{\text{rev}} = a_1 + a_2 T + a_3 T \ln(P_{\text{O}_2}) + 2a_3 T [\ln(P_{\text{H}_2}) - \ln(P_{\text{H}_2\text{O}})] \quad (\text{III-16})$$

where  $a_i$  are physical parameters detailed in Table III-2 according to the Gibbs free energy  $G_0$  and entropy  $S_0$  variations at standard temperature and pressure. In addition,  $R$  refers to the universal gas constant and  $F$ , the Faraday constant in the expressions of  $a_i$ . Finally, the Nernst reversible potential only depends on temperature  $T$  and partial pressures  $P_j$  ( $j: \text{O}_2, \text{H}_2, \text{H}_2\text{O}$ ). Barbir [23] explained fuel cell chemistry and thermodynamics in details.

**Table III-2**

Physical parameters

Parameter	Expression	Value	Unit
$a_1$	$\frac{\Delta H_0}{2F}$	1.4824	[V]
$a_2$	$\frac{\Delta S_0}{2F}$	$-1.593 \cdot 10^{-3}$	[V/K]
$a_3$	$\frac{R}{4F}$	$2.154 \cdot 10^{-5}$	[V/K]

### 3.2.2 Overpotential

A semi-empirical formulation is adopted to describe the overpotential, which is function of temperature, current density and partial pressures:

$$\eta = \beta_1 + \beta_2 T + \beta_3 T \ln(i) + \beta_4 T \ln(P_{O_2}) + \beta_5 T \ln(P_{H_2O}) + \beta_6 T \ln(P_{H_2}) \quad (\text{III-17})$$

where  $\beta_i$  are empirical coefficients dependent on the thermodynamics and kinetics of the electrochemical reactions.  $\beta_i$  parameters were calibrated on a 5 cm<sup>2</sup> active area laboratory cell for different polarization curves recorded where the partial pressures, the temperature and the humidity in the cell varied [138]. They are listed in Table III-3.

**Table III-3** [138]

Empirical coefficients

Coefficient	Value	Unit
$\beta_1$	-0.75384	[V]
$\beta_2$	$3.39 \cdot 10^{-4}$	[V/K]
$\beta_3$	$-7.84 \cdot 10^{-5}$	[V/K]
$\beta_4$	$1.298 \cdot 10^{-4}$	[V/K]
$\beta_5$	0	[V/K]
$\beta_6$	$5.13 \cdot 10^{-5}$	[V/K]

### 3.2.3 Cell Internal Resistance

The total cell internal resistance (density)  $R_T$  includes both ionic, electronic, and contact resistances denoted by the p (proton), e and c subscripts, respectively:

$$R_T = R_p + R_e + R_c \quad (\text{III-18})$$

Electronic resistance is negligible, even when non-metal current collectors are used [23]. Finally, the ohmic losses become:

$$\eta_{\text{ohm}} = -(R_p + R_c) i \quad (\text{III-19})$$

The contact resistance only depends on the materials characteristics. Nandjou [37] presented in detail the different contact resistances in the F-geometry FC by considering the real architecture of bipolar plates and welding points associated. The proton resistance of the membrane is obtained by the following equation:

$$R_p = \frac{e_M}{\sigma_M} \quad (\text{III-20})$$

where  $e_M$  is the membrane thickness and  $\sigma_M$ , the membrane proton conductivity, which, as discussed in Chapter I, strongly depends on the water content in the membrane. It is defined according to Springer's law [41]:

$$\sigma_M = (33.75 \lambda_M - 21.41) e^{1268/T} \quad (\text{III-21})$$

### 3.3 Source Terms

#### 3.3.1 Electrochemical Source Term

According to the Faraday's law, the reactants consumption and water production  $S_{\text{f}}$  are directly proportional to current density:

- at the cathode side

$$S_{\text{O}_2} = -\left(\frac{M_{\text{O}_2}}{4F} i\right) / e_{\text{comp}} \quad (\text{III-22})$$

$$S_{\text{H}_2\text{O}} = +\left(\frac{M_{\text{H}_2\text{O}}}{2F} i\right) / e_{\text{comp}} \quad (\text{III-23})$$

- at the anode side

$$S_{H_2} = - \left( \frac{M_{H_2}}{2F} i \right) / e_{\text{comp}} \quad (\text{III-24})$$

where  $M_j$  are the molar mass of the  $j$ -species ( $j$ :  $O_2$ ,  $H_2$ ,  $H_2O$ ). Negative and positive signs conventionally represent the consumption and production, respectively. The source term  $S_f$  in mass balance becomes:

- at the cathode side

$$S_f = S_{O_2} + S_{H_2O} \quad (\text{III-25})$$

- at the anode side

$$S_f = S_{H_2} \quad (\text{III-26})$$

where water is produced in vapor form by the electrochemical reaction.

### 3.3.2 Heat Source Term

The heat source term  $S_T$  in the energy transport equation in CLs, represent the heat released by the electrochemical reaction (as an exothermic process) by considering the total energy balance, which corresponds to the difference of the power by hydrogen combustion and electrical power produced:

$$S_T = \begin{cases} \left( \frac{\Delta H_0}{2F} - U_{\text{cell}} \right) i & \text{at the cathode side} \\ 0 & \text{at the anode side} \end{cases} \quad (\text{III-27})$$

where  $\Delta H_0$  is the enthalpy of formation of water in the operating conditions. All the entropy and electrochemical activation heats are located at the cathode catalyst layer/membrane interface in the model. As discussed at length, a phase change of water can take place in all the layers of the cell except in the cooling circuit and membrane. The enthalpy of reaction  $\Delta H_0$  can take two different values  $\Delta H_v$  and  $\Delta H_l$  (Eq. (III-28)) depending on the phase of the water produced, respectively vapor or liquid. As stated in Section 3.4, in this one-fluid model, water vapor is treated as an incondensable ideal gas. Its partial pressure  $P_{H_2O}$  can then reach a value

higher than the saturation pressure  $P_{\text{sat}}(T)$  (only temperature-dependent), which considers a thermodynamic equilibrium between vapor and liquid phase. A production of vapor is considered when the partial pressure of water is lower than the saturation pressure. Conversely, if the saturation pressure is reached or exceeded, water cannot be produced in vapor phase, and a production of liquid water is considered. Finally, the two values of the reaction enthalpy are:

$$\Delta H_0 = \begin{cases} \Delta H_v = 242 \text{ kJ mol}^{-1} & \text{if } P_{\text{H}_2\text{O}} < P_{\text{sat}}(T) \\ \Delta H_l = 285.8 \text{ kJ mol}^{-1} & \text{if } P_{\text{H}_2\text{O}} \geq P_{\text{sat}}(T) \end{cases} \quad (\text{III-28})$$

The heat released during the reaction can be significant, which is important to dimension the heat exchanger for an automobile application. Furthermore, the temperatures can be highly heterogeneous particularly when considering a large electrochemical surface area. For example, a maximum difference of  $14^\circ\text{C}$  (Fig. III-9) is reached for the F-type stack in low power (humid) operating conditions [144].

Moreover, heat by Joule effect  $Q_T$  is produced by the electrons and protons transport in the conductive components:

$$Q_T = \frac{i^2}{\sigma_{\text{comp}}} \quad (\text{III-29})$$

where  $\sigma_{\text{comp}}$  is the electric conductivity of the component.

### 3.4 Condensation Model

First, to avoid a complex multiphase model, a partial pressure of water is hypothetically calculated by the transport equations implemented in the one-fluid model. Indeed, the simulated water is considered as an incondensable perfect gas, which means both liquid and vapor phases are assimilated to water vapor, then considering a single-phase flow. With this assumption, the hypothetical water pressure can be higher than the saturation pressure. In this case,  $P_{\text{H}_2\text{O}} > P_{\text{sat}}(T)$ , it is assumed that water is produced in liquid phase. Accordingly, in order to evaluate the quantity of liquid water, the saturation is post-treated from the different pressures calculated by the model according to the following expression:

$$\begin{cases} s = 0 & \text{if } P_{\text{H}_2\text{O}} \leq P_{\text{sat}}(T) \\ s = \frac{P_{\text{H}_2\text{O}} - P_{\text{sat}}(T)}{P - P_{\text{sat}}(T)} & \text{if } P_{\text{H}_2\text{O}} > P_{\text{sat}}(T) \end{cases} \quad (\text{III-30})$$

where  $P$  is the total pressure of the gas mixture, i.e. the sum of the partial pressures namely dihydrogen and water vapor at the anode and dioxygen, dinitrogen and water vapor at the cathode. The demonstration of Eq. (III-30) can be found in Appendix D. Therefore, the thickness of liquid water in a component is post-processed in the numerical results by multiplying the porosity  $\varepsilon_{\text{comp}}$ , thickness  $e_{\text{comp}}$  and saturation  $s_{\text{comp}}$  of that component. The liquid thicknesses in each component are summed to calculate the thickness of liquid water  $e_{\text{l,cell}}$  in one cell:

$$e_{\text{l,cell}} = \sum \varepsilon_{\text{comp}} e_{\text{comp}} s_{\text{comp}} \quad (\text{III-31})$$

where the comp subscript refers to any component of the cell. The amount of liquid water is assumed negligible in the membrane. As a reminder, the porosity is equal to one in the gas channels. Finally, the total liquid water thickness in the stack is obtained by multiplying the thickness of liquid water in one cell with the number of cells. Each cell is then considered identical, which means that the endplates behavior is neglected.

## 4. One-Fluid and Phase-Separated Models Analysis

In this section, the one-fluid model is compared to a classical phase-separated model [139] in order to examine in which configuration the results obtained by both models would be identical. The saturations and pressure drops obtained by the two models are compared. A detailed sensitivity study to some key criteria for the two-phase flow modeling is presented in Section 4.2.

### 4.1 Models Comparison

The empirical model proposed by Lockhart-Martinelli (L-M) [139] represents both the liquid phase with a velocity noted  $V_{\text{l},1}$  and gas phase with a velocity  $V_{\text{g},1}$ . The saturation  $s_1$  calculated by this model is none other than the volume fraction of the liquid phase presented in Chapter III. As discussed previously, the one-fluid model considers a single gas mixture moving at the velocity  $V_{\text{g},2}$ . The velocity of the condensed water vapor  $V_{\text{vap},2}$  is then equal to the mixture

velocity since the flow is considered homogeneous ( $V_{g,2} = V_{\text{vap}_c,2}$ ). The saturation described by Eq. (III-30) is denoted  $s_2$  for the one-fluid model. Now consider a flow of moist air in a single channel without phase change and identical gas flow rates for both models. The volume velocities are written as follows:

$$V_{g,1} = \frac{\dot{m}_g}{\rho_g A_c (1 - s_1)} \quad (\text{III-32})$$

$$V_{g,2} = \frac{\dot{m}_g}{\rho_g A_c (1 - s_2)} \quad (\text{III-33})$$

$$V_{l,1} = \frac{\dot{m}_l}{\rho_l A_c s_1} \quad (\text{III-34})$$

$$V_{\text{vap}_c,2} = \frac{\dot{m}_{\text{vap}_c}}{\rho_{\text{vap}_c} A_c s_2} \quad (\text{III-35})$$

where g, l and  $\text{vap}_c$ , subscripts denote the gas, liquid and condensed vapor, respectively while 1 and 2 subscripts refer to L-M and one-fluid models.  $\dot{m}$  is the mass flow rate,  $A_c$ , the channel section and  $s$ , the saturation. Eventually, the liquid and condensed vapor flow rates are assumed to be identical.

#### 4.1.1 Equal Saturations between the Two Models

Considering same saturation for both models ( $s_1 = s_2 = s$ ), the gas velocities are equal ( $V_{g,1} = V_{g,2} = V_g$ ). Therefore, the ratio  $S$  of the gas velocity to the liquid velocity can be deduced according to the previous descriptions:

$$S = \frac{V_g}{V_{l,1}} = \frac{V_{\text{vap}_c,2}}{V_{l,1}} = \frac{\rho_l}{\rho_{\text{vap}_c}} \quad (\text{III-36})$$

According to Eq. (III-36), the one-fluid model shows good agreement with the phase-separated model for a velocity ratio, also called slip ratio, equal to the liquid/gas density ratio ( $\rho_l/\rho_{\text{vap}_c}$ ).

For example, the density ratio is 1055 under operating conditions of 1.5 bars and 80 °C. Therefore, the flow of the liquid phase can be considered stagnant or quasi stagnant because about 1000 times ( $\rho_l/\rho_{vap_c}$ ) less rapid than the gas flow. In addition, such a slip ratio value is higher than more classical correlation, which can be found in the literature. For example, Chisholm [145] obtains a velocity ratio of 27.7 under the same operating conditions (1.5 bars and 80 °C) by introducing the following formulation:

$$S_{Chi} = \sqrt{1 - x \left( 1 - \frac{\rho_l}{\rho_g} \right)} \quad (III-37)$$

where x is the gas quality described by:

$$x = \frac{\dot{m}_g}{\dot{m}_g + \dot{m}_l} \quad (III-38)$$

The flow in PEM fuel cells is conducted in gas channels with small section and specific geometry (the channels can be wavy, with possible bends, etc.) while the Chisholm model is based on a simple annular flow in a larger hydraulic diameter channel. Moreover, mass transfers occur at the interface of GC and GDL due to water transport mechanisms. All these reasons may explain higher velocity ratio in PEM fuel cells compared to Chisholm description.

#### 4.1.2 Equal Pressure Drops between the Two Models

Another comparison is carried out considering identical pressure losses of the liquid phase for the L-M model and the condensed vapor for the one-fluid model.

##### ➤ Phase-Separated Pressure Drop Model

The L-M model relates the pressure drop of the two-phase  $\Delta P_1$  as a function of that of the gas phase  $\Delta P_g$  introducing an empirical two-phase multiplier  $\phi_g$ :

$$\Delta P_1 = \phi_g^2 \Delta P_g \quad (\text{III-39})$$

where  $\Delta P_g$  is formulated when the gas phase flows alone in the channel by the expression:

$$\Delta P_g = 32\mu_g \frac{\dot{m}_g}{\rho_g A_c} \frac{l}{d_c^2} \quad (\text{III-40})$$

where  $l$  is the channel length and  $d_c$ , the hydraulic diameter. The two-phase multiplier first introduced by L-M for a laminar flow is expressed by:

$$\phi_g^2 = 1 + CX + X^2 \quad (\text{III-41})$$

where  $C$  is a parameter depending on the flow regime and  $X$ , the Martinelli parameter. The square Martinelli parameter is the pressure drop ratio between the liquid and gas phase:

$$X^2 = \left( \frac{dP}{dz} \right)_l / \left( \frac{dP}{dz} \right)_g \quad (\text{III-42})$$

The pressure drop can be replaced to obtain the following relation:

$$X^2 = \frac{\mu_l \dot{m}_l}{\rho_l} \frac{\rho_g}{\mu_g \dot{m}_g} = \frac{\mu_l}{\mu_g} \frac{V_l}{V_g} \frac{s_1}{1 - s_1} \quad (\text{III-43})$$

Finally, the saturation of the phase-separated model is deduced according to the Martinelli parameter:

$$s_1 = \left( 1 + \frac{\mu_g}{\mu_l} \frac{V_g}{V_l} \frac{1}{X^2} \right)^{-1} \quad (\text{III-44})$$

➤ One-Fluid Pressure Drop Model

The pressure drop for the one-fluid model  $\Delta P_2$  is expressed as follows:

$$\Delta P_2 = 32\mu_2 \frac{\dot{m}_g + \dot{m}_l}{\rho_2 A_c} \frac{l}{d_c^2} \quad (\text{III-45})$$

where  $\mu_2$  is the moist air dynamic viscosity proposed by Wilke [146] in the numerical model.  $\mu_2$  is both dependent on the saturation and the viscosities of the gas and liquid phases. Other formulations can be found in the literature [147]-[149].  $\rho_2$  is the moist air density defined as an homogeneous property:

$$\rho_2 = \rho_{\text{vapc}} s_2 + \rho_g (1 - s_2) \quad (\text{III-46})$$

### ➤ Relation between Saturation Models

As mentioned, we consider equivalent pressure drops between the models  $\Delta P_1 = \Delta P_2$  in order to obtain a relation between the saturations:

$$s_1 = \left( 1 + 4 S \frac{\mu_l}{\mu_g} \left[ -C + \sqrt{C^2 - 4 \left( 1 - \frac{\mu_l}{\mu_g} \frac{1}{1 - s_2} \right)} \right]^{-2} \right)^{-1} \quad (\text{III-47})$$

This equation is developed in Appendix F.

## 4.2 Sensitivity Analysis

In this section, the C parameter and velocity ratio S are both studied to investigate their impact on the saturations relationship described by Eq. (III-47). Accordingly, we can find the best fit of these parameters to match the one-fluid model to the phase-separated model.

### 4.2.1 Sensitivity Analysis to C Parameter

The hydraulic diameter of a channel does not exceed 1 mm for most bipolar plates in PEM fuel cells. Even for high current density and stoichiometry, the Reynolds number is low ( $< 2000$ ) to always consider both gas and liquid flows as laminar (or stagnant). Many formulations (dependent on the flow regime) of the C coefficient have been studied in the literature. For laminar flows for both phases, L-M recommend  $C = 5$  while Chisholm [145] proposes  $C = 2.5$ . Mishima

and Hibiki [150], Zhang et al. [151], Li and Wu [152] suggest an equation for the  $C$  parameter dependent on dimensionless numbers. Muzychka and Awad [153] reference other formulations. Kim and Mudawar [154] reviewed a lot of this parameter for channels with different sizes and a large panel of fluids. Fig. III-2 presents the evolution of  $s_1$  as a function of  $s_2$  with different values of  $C$  when  $S$  is fixed to 1055, i.e. the value of the density ratio ( $\rho_l/\rho_{vap,c}$ ) under operating conditions of 1.5 bars and 80 °C. The formulations of the  $C$  parameter selected for this analysis are the closest to the conditions in a PEM fuel cell (micro-channels and air/water flow).

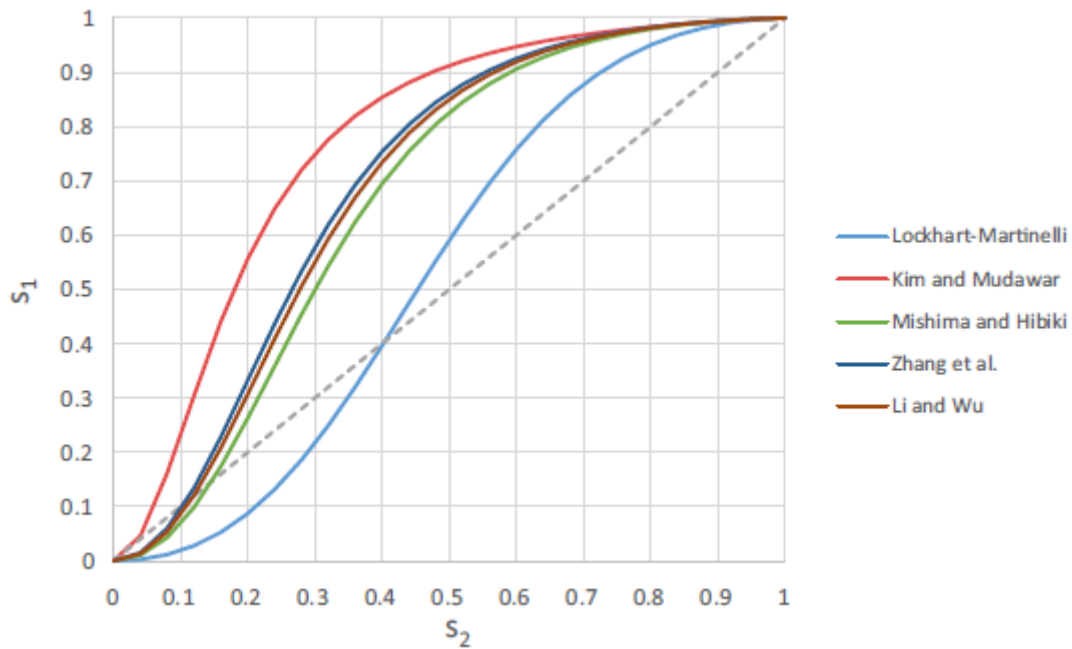


Fig. III-2. Relation between the saturations  $s_1$  and  $s_2$  with different formulation of  $C$  parameter and  $S$  equal to 1055 – the dashed curve represents the exact equality of the saturations of the two models.

The value of 5 for the  $C$  parameter (blue curve in Fig. III-2) proposed by L-M gives the best agreement between the two models over the entire liquid saturation range (from 0 to 1). However, as pointed out by Kim and Mudawar [154], this value is too high to correctly represent the two-phase flow for low saturation corresponding to usual saturation in PEM fuel cell operation, which is generally less than 0.2. Good results can be observed for the other correlations at low saturation, particularly for the formulation of Kim and Mudawar [154] when  $s < 0.05$  (Fig. III-2). Finally, this parameter has a significant impact on the two-phase formulation.

#### 4.2.2 Sensitivity Analysis to the Velocity Ratio

In this section, the saturations are plotted for different velocity ratios by first considering the Kim and Mudawar [154] correlation Fig. III-3a and then fixing the C parameter to a value of 2 (Fig. III-3b). The lower the velocity ratio, the more the one-fluid model overestimates the amount of liquid water compared to the phase-separated model. For example, for a small velocity ratio  $S = 10$  (dark green curve in Fig. III-3), the saturation obtained with the one-fluid model is more than 3 times higher than that of the phase-separated model, regardless of the correlation, for lower saturations to 0.2. For the ratio equal to 1000 (red curve in Fig. III-3), corresponding approximately to the ratio of the density of liquid water to that of vapor as mentioned previously, a good agreement between models is observed at low saturation. Finally, the closest correspondence is obtained for the Kim and Mudawar [154] correlation and ratio  $S = 100$  (orange curve in Fig. III-3a) if the entire range of liquid saturation is considered (from 0 to 1).

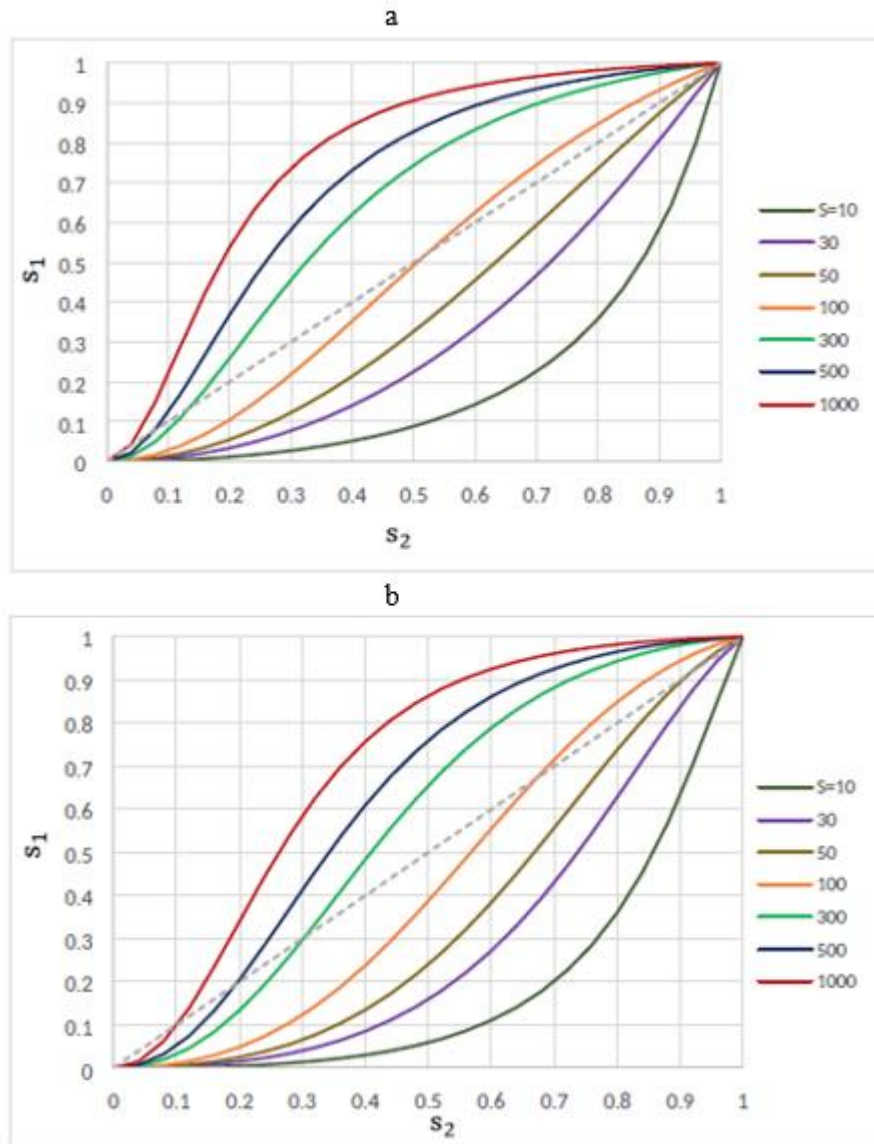


Fig. III-3. Relation between the saturations  $s_1$  and  $s_2$  with different value of the velocities ratio for (a)  $C$  parameter proposed by Kim and Mudawar [154] and (b)  $C = 2$  – the dashed curve represents the exact equality of the saturations of the two models.

Ultimately, the phase-separated model was considered as reference to compare it to one-fluid model although it should first be validated by comparison with experimental tests in PEMFC operating conditions. Therefore, the previous analyzes validate the 1-F model with its particular two-phase approach for small saturations when the velocity ratio is equal to the density ratio. However, the validity domain of the model cannot be clearly defined, specifically when higher saturations are considered.

## 5. Stack Design

The design and composition of the stack (Fig. III-4) have been extensively described in [37]. Briefly, a dedicated stack composed of 5 cells with an active surface of  $220 \text{ cm}^2$  has been build. It is made of stamped stainless steel bipolar plates with parallel serpentine channels (Fig. III-4) and low neutron absorption gilded aluminum end-plates. It comprises home-made MEA composed of  $25 \text{ }\mu\text{m}$  thick reinforced perfluorosulfonic acid membrane, commercial Pt based catalyst layer with anode and cathode loading of  $0.1$  and  $0.4 \text{ mg/cm}^2$  respectively, Sigracet® 24BC from SGL Group™ as gas diffusion layer and a  $45 \text{ }\mu\text{m}$  thick micro-porous layer on both sides. Heavy water is used as coolant because of its low neutron absorption. The geometrical parameters are listed in Table III-4. This design has been extensively studied during the past decade. It used here in order to compare the results of the model with previous simulations and experiments. The process of the neutron imaging in order to measure the water content in PEMFCs is detailed in Appendix E.

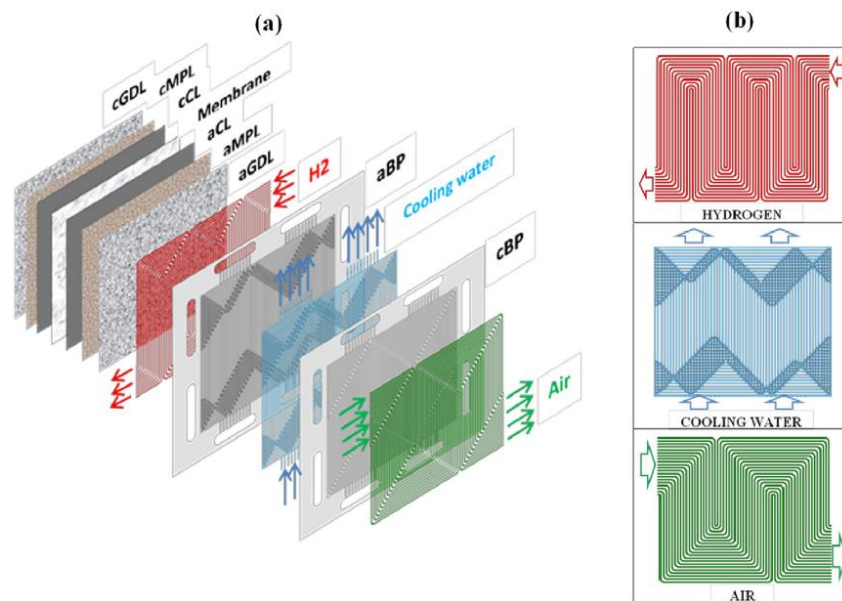


Fig. III-4. (a) The reference geometry of the pseudo-3D model consists of 9 solid domains: one membrane, two catalyst layers (aCL and cCL), two micro-porous layers (aMPL and cMPL), two gas diffusion layers (aGDL and cGDL), two half-bipolar plates (aBP and cBP) – (b) Presentation of the flow fields: hydrogen, cooling water and air [37].

**Table III-4**  
Geometrical parameters

Component thickness		Value [ $\mu\text{m}$ ]
Bipolar Plate		200
Gas Channel depth	Anode	400
	Cathode	400
Gas Diffusion Layer	Anode	250
	Cathode	250
Micro-Porous Layer	Anode	40
	Cathode	40
Catalyst Layer	Anode	5
	Cathode	10
Membrane		25

## 6. Numerical Procedure

The governing equations are discretized by the finite element method. The model is solved by a commercial solver: COMSOL Multiphysics 5.4. The mesh is about  $1.10^5$  elements (Fig. III-5). The calculation time is about 1h 20 min on an Intel Core i7-7820HQ 2.90 GHz – RAM 32 GB to obtain a relative error of  $10^{-4}$ . Direct solvers are used with a MUMPS (MULTifrontal Massively Parallel Sparse direct Solver) for all physics except for fluid dynamics in the cooling circuit where the PARDISO (PARallel sparse DIrect SOLver) solver is recommended. All calculations are stationary with five successive steps using results from the previous step. The first step is to calculate the conservation equations of mass and species as well as Darcy's law in GCs and GDEs without calculating the current. The second step is similar to the first but including the calculation of the current by coupling the conservation equations to the electrochemical model. Fluid dynamics (conservation equations for mass and momentum) in the cooling circuit are solved in the third step. The heat equations in all the layers are next calculated in the 4th step. Finally, the equations of the second step are solved again to get the results that are compared to experimental tests.

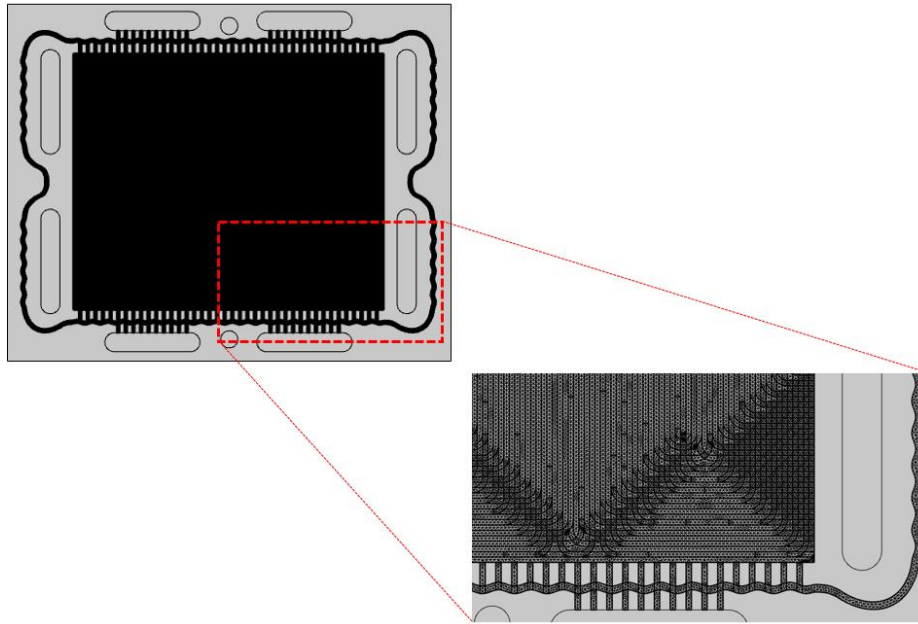


Fig. III-5. Mesh model based on free triangle elements ( $\sim 1.10^5$ ).

## 7. Results and Discussion

The numerical thermal and electrochemical results of the 1-F model were validated in a previous work by comparison with local temperature and current densities measurements [138]. The heterogeneous distributions are well captured in a large range of operating conditions [144]. In this section, the simulated results are compared to liquid water measurements in order to investigate the accuracy and quantitative predictability of the two-phase flow formulation of the 1-F model. Two different operating conditions were compared: at low power, called humid conditions and at high power, called dry conditions. Some correlations of key parameters in the mechanisms of water transport through the membrane are first analyzed.

### 7.1 Sensitivity Analysis to Water Transport Coefficients

As discussed in Chapter I, the modeling of water transport through the membrane is strongly impacted by the electro-osmotic drag and molecular diffusion coefficients. The impact of these coefficients on the distribution and quantity of liquid water is examined by implementing different formulations of these coefficients in the model.

### 7.1.1 Sensitivity Analysis to EO Drag Coefficients

The total liquid water thickness (averaged) for a stack of five cells is plotted (Fig. III-6) along the indicated reference cut line at 50% of the cell (Fig. E-1 in Appendix E) in low power operating conditions (Table III-5) for different EO drag coefficients  $a_{EO}$  (Table I-1) when the membrane diffusion coefficient  $D_M$  (Table I-2) proposed by Motupally [50] is used. The general pattern of the total liquid water thickness is not impacted by any of the EO drag correlations (Fig. III-6). However, the amplitude of the total thickness can significantly vary. Indeed, there is a thickness difference of up to 0.14 mm maximum between the EO drag correlations proposed by Zawodzinski [44] (blue curve in Fig. III-6) and Meier [43] (yellow curve), which corresponds to 19% of the maximum liquid water thickness. The Zawodzinski [44] correlation is retained for the rest of this work, which is closest to the thickness of liquid water measured during the tests (black curve). In addition, this correlation is simple to implement in the code for  $\lambda_M < 14$ . The oscillations in Fig. III-6 represent the alternation of channels and ribs along the cut line. The thickness of liquid water has been averaged in Fig. III-6 (by 3.6 mm step) due to the large number of channels and ribs, which would make the graph illegible considering all the channel/rib heterogeneities.

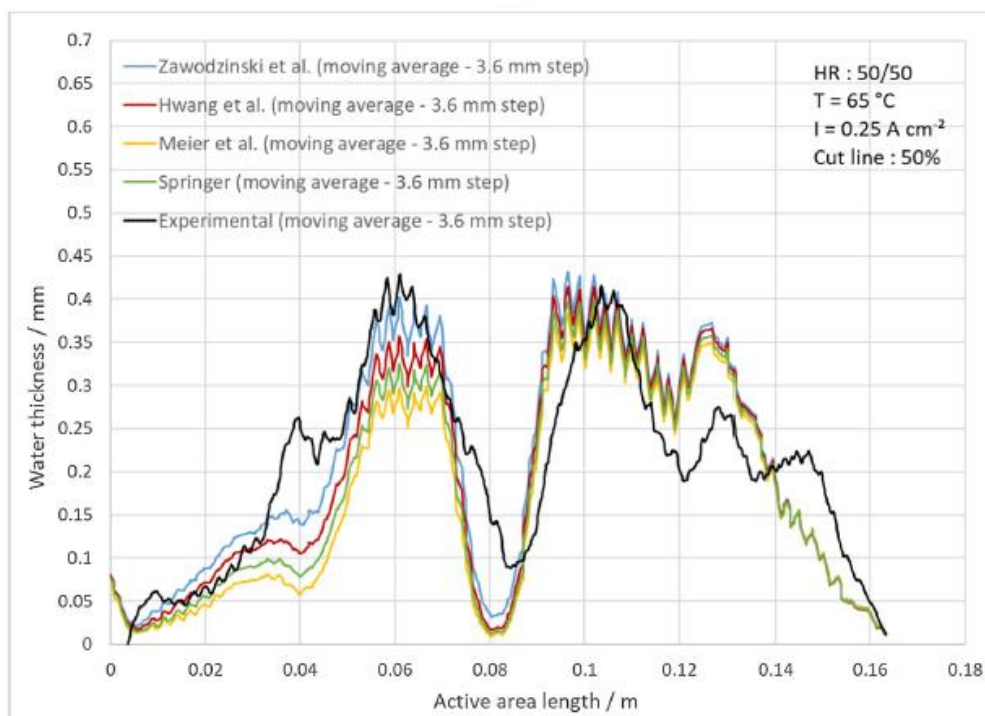


Fig. III-6. Water thickness for the 5 cells of the stack simulated at the indicated 50% cut line in the operating conditions presented in Table III-5 according to different formulations of the electro-osmotic drag coefficient  $a_{EO}$ .

### 7.1.2 Sensitivity Analysis to Membrane Diffusion Coefficients

Similar to the EO drag coefficient, the total liquid water thickness is plotted (Fig. III-7) for different membrane diffusion coefficients  $D_m$  (Table I-2) when the EO drag coefficient  $a_{EO}$  (Table I-1) proposed by Zawodzinski [44] is used. None of the formulations affects the profile of the liquid water distribution conversely to its quantity. Indeed, the maximum difference of the total liquid water thickness reaches 0.17 mm, corresponding to 24% of the maximum thickness between the Fuller [48] (green curve in Fig. III-7) and Motupally [50] (orange curve) formulation. We will keep the Motupally [50] correlation for the rest of the study, which gets the numerical liquid water thickness closest to the measurements (black curve).

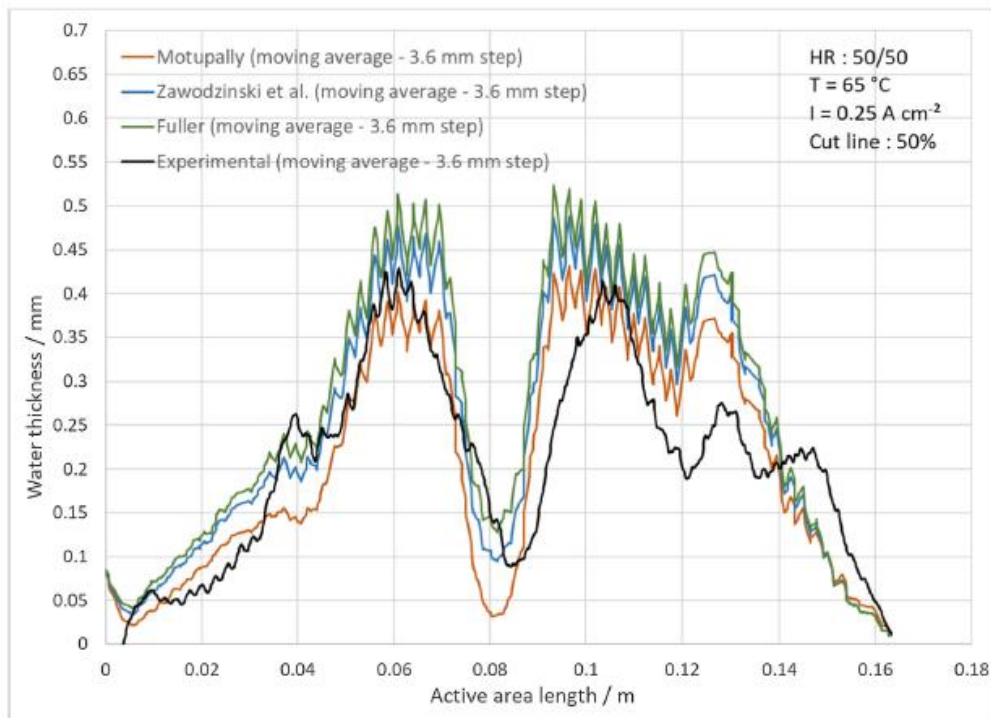


Fig. III-7. Water thickness for the 5 cells of the stack simulated at the indicated 50% cut line in the operating conditions presented in Table III-5 according to different formulations of the membrane diffusion coefficient  $D_m$ .

Despite a general trend, there may be large variations of the liquid water distribution according to different transport coefficients. The electro-osmotic drag and membrane diffusion coefficients turn out to be key elements in the complex modeling of the water transport through the membrane. A dedicated study should be conducted to analyze in detail these mechanisms in PEM fuel cells.

## 7.2 Low Power Operating Conditions

The total thickness of liquid water obtained with the numerical model is compared to measurements by neutron imaging for a stack of five cells in low power operating conditions first (Table III-5) at two different current densities.

**Table III-5**

Constant operating parameters.		
Experimental parameters		Setpoint
Inlet pressure reactant gases /bar		1.5
Temperature /°C		65
Stoichiometry coefficient	Hydrogen	1.5
	Air	2
Relative humidity (%)	Hydrogen	50
	Air	50

### 7.2.1 Low Current Density

The model is able to quantify the liquid water and precisely predict its location on the scale of the stack (Fig. III-8) at low current density (0.25 A/cm<sup>2</sup>). The numerical results (Fig. III-8b) are very close to those measured (Fig. III-8a) despite the two-phase approach used. In addition, the liquid water accumulates in colder areas in accordance with the numerical temperature maps shown in Fig. III-9. More information regarding heat management in fuel cells can be found in the works of Nandjou [37]. The average thickness of liquid water in the stack is 0.3 mm. Furthermore, the liquid water is less present at both the hydrogen and air inlet (upper right and left areas respectively in Fig. III-8) due to a relative humidity of 50% for the inlet gases.

However, liquid water is slightly underestimated by the model at the anode and cathode outlet (lower left and right zones respectively in Fig. III-8). Finally, the real design of the bipolar plates is well captured by the simulation by correctly representing the rib/channel patterns.

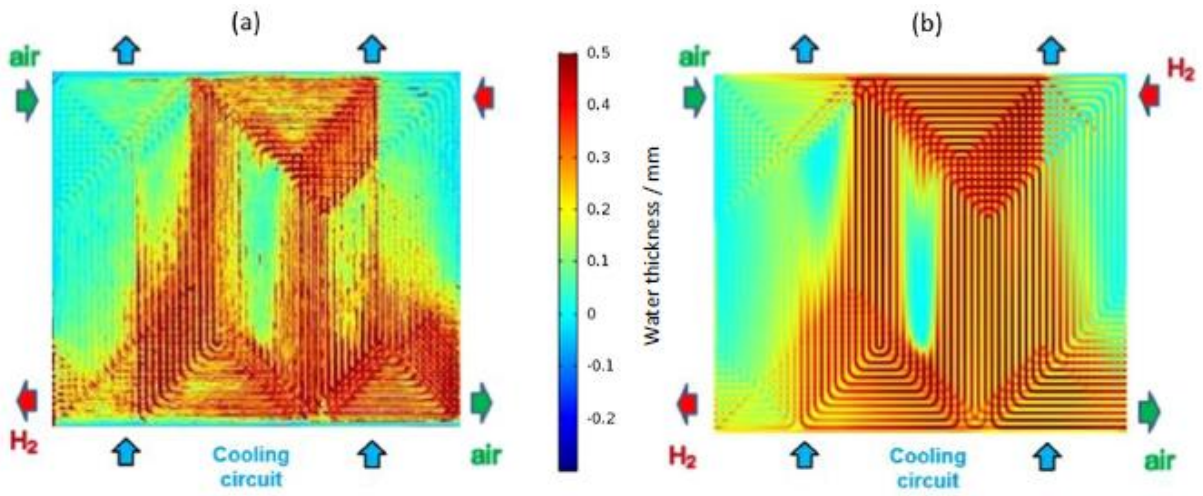


Fig. III-8. (a) measured and (b) simulated total water thickness for five cells in humid conditions at a low current.

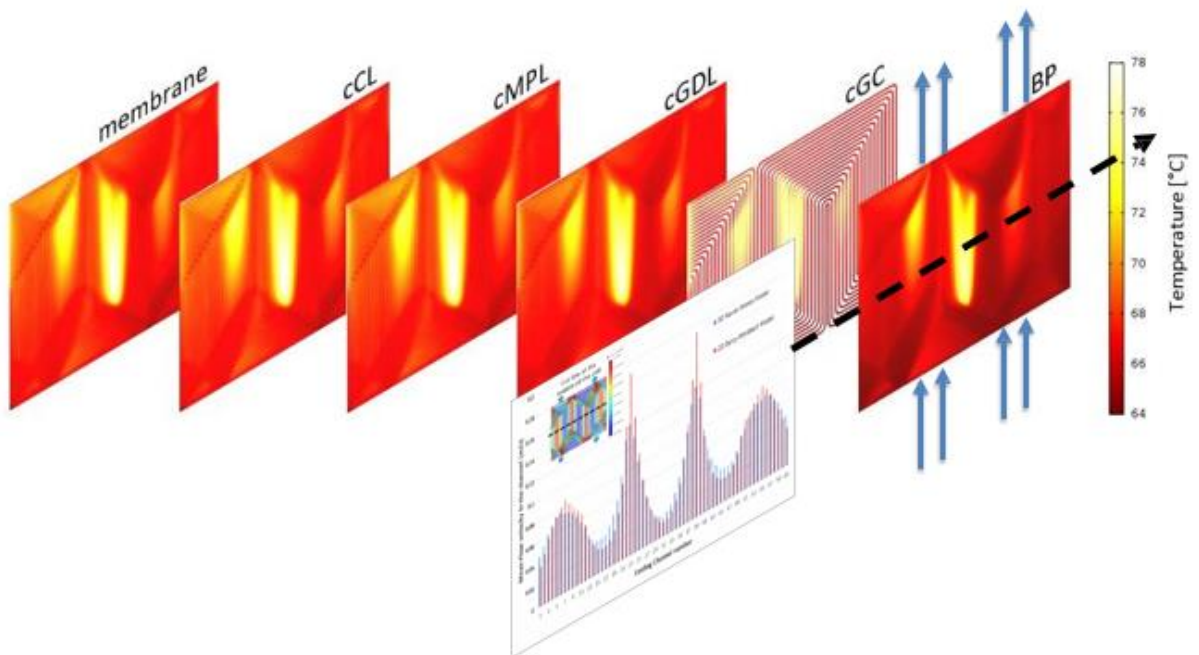


Fig. III-9. Numerical temperature maps in the cathode compartment and membrane.

### 7.2.2 High Current Density

Fig. III-10 presents the distribution of liquid water measured and obtained numerically on the left and right mappings respectively in the figure for a higher current density ( $1 \text{ A/cm}^2$ ). The other operating conditions are identical to the case of lower current density. The model satisfactorily locates the liquid water without being able to quantify it. Indeed, the numerical results overestimate the quantity of water at the hydrogen outlet and underestimate it at the air outlet (lower left and right zones respectively in Fig. III-10).

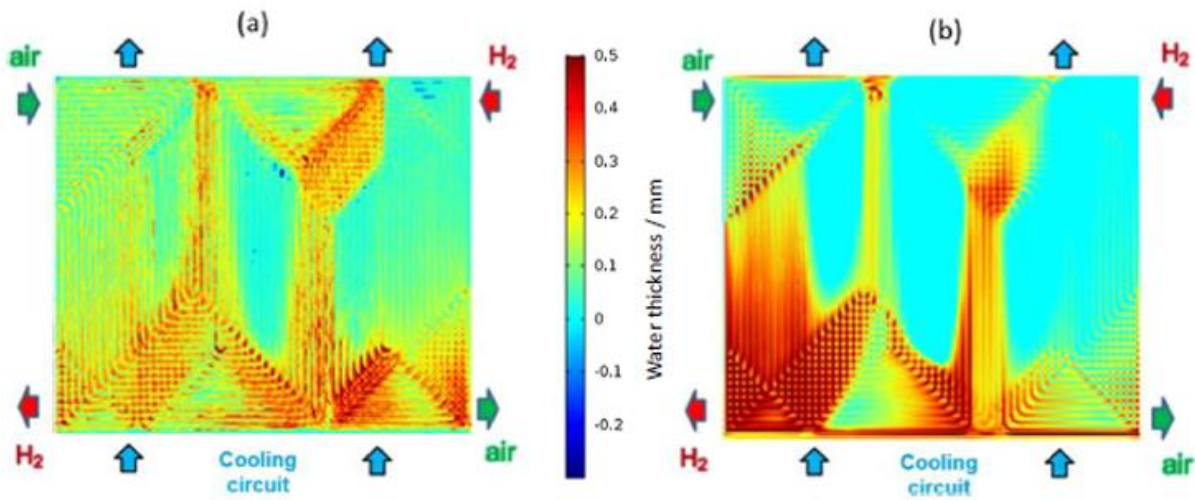


Fig. III-10. (a) measured and (b) simulated total water thickness for 5 cells for a high current density in humid conditions.

### 7.2.3 Liquid Water Thickness along the Reference Cut Line

A cut is made at 50% of the cell width (Fig. E-1 in Appendix E), perpendicular to the cooling circuit in order to compare the measured and numerical liquid water thickness (Fig. III-11). The 1D plot at the different reference cut lines allows to better illustrate the differences in water content distribution in order to identify the main sources of water content heterogeneities. The model is able to accurately predict water areas in comparison with neutron imaging. As a reminder, the oscillations over the line plots are related to the channel/rib heterogeneities.

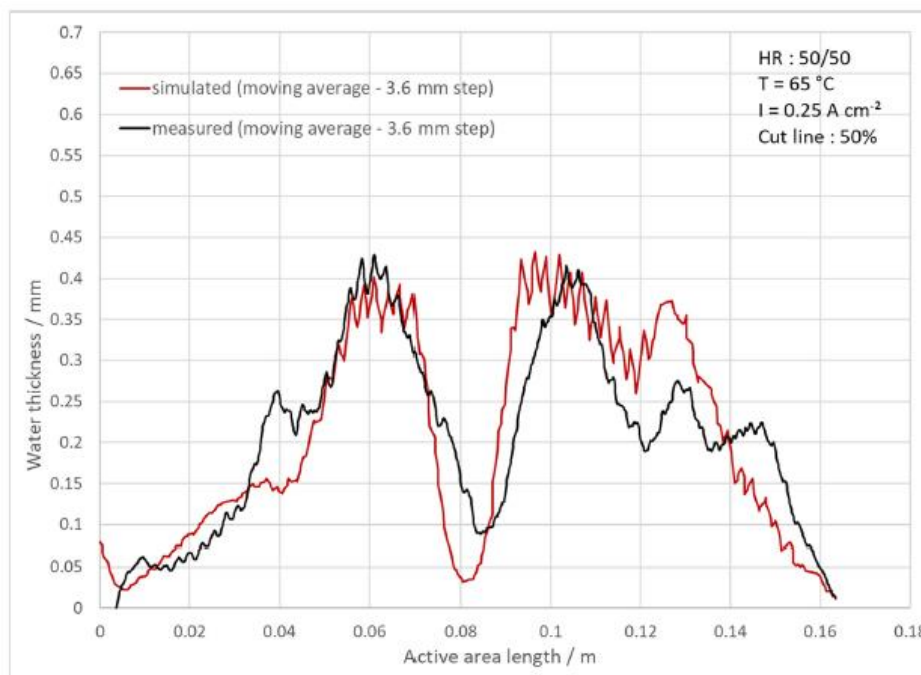


Fig. III-11. Water thickness measured (black line) and simulated (red line) at the indicated 50% cut line in the operating conditions presented in the Table III-5 for a current density of  $0.25 \text{ A cm}^{-2}$ .

### 7.3 Analysis of Results at the Local Level

In accordance with the good results obtained by the model for a low current density in humid conditions, the distribution of liquid water is studied in each layer (Fig. III-12). Its transport mechanisms are then analyzed (Fig. III-13). Finally, the liquid water is observed at the rib/channel scale taking into account the real flow-field designs.

#### 7.3.1 Water Distribution over the Cell Surface in Each Layer

The thickness of the liquid water and saturation are presented in the different layers (anode/cathode GCs and GDEs) of a cell in Fig. III-12 for the same operating conditions as before. Both hydrogen and air inlet dry the anode and cathode GDEs because of the low Relative Humidity (RH) of the gas flows (50% for both side at the inlet). Liquid water increases from the air inlet to the outlet since the water production and oxygen reduction reactions occur at the cathode side. The water is also driven from the anode to the cathode by the electro-osmotic flux. In addition, lower water saturation is observed in some areas because of hot spot (Fig. III-9) induced by water cooling as mentioned in Nandjou et al. [138][144].

The model provides valuable information both in terms of the location of the water and the layer to be observed. As a reminder, these data are difficult to obtain by experimental tests, in particular at the rib/channel scale. The measures also take a long time to set up and carry out. Numerical models therefore appear to be useful tools in understanding phenomena while saving time. Finally, a large number of operating conditions can be simply tested with the model.

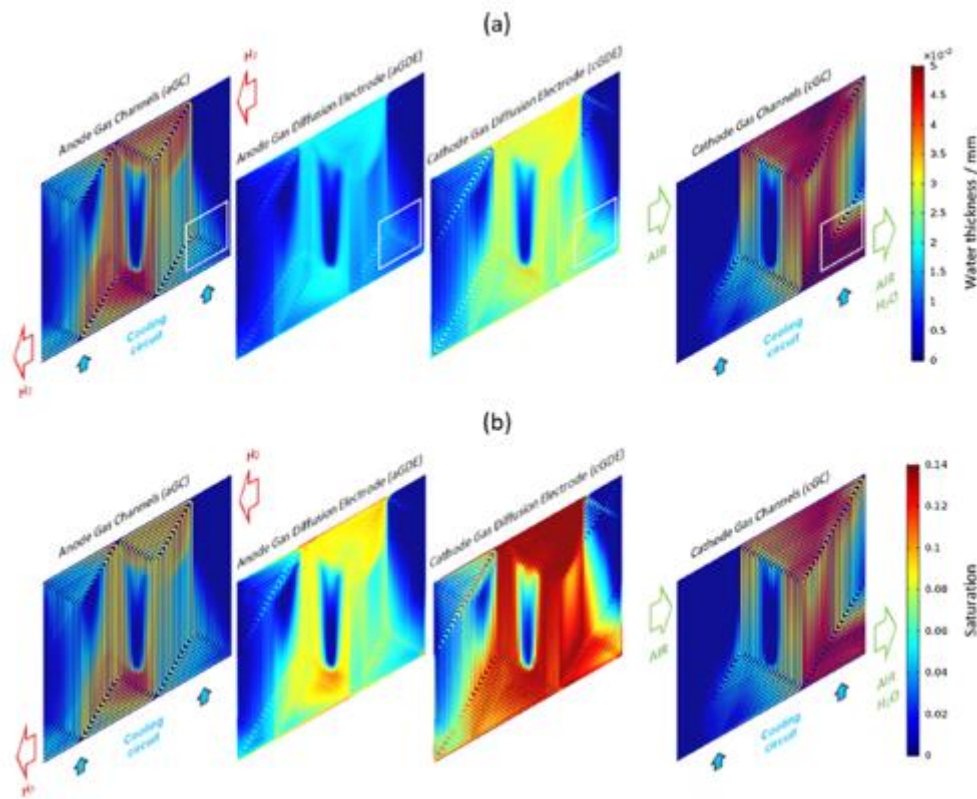


Fig. III-12. (a) Water thickness and (b) saturation distribution in the anode and cathode gas channels and gas diffusion electrode, in the operating conditions presented in Table III-5 for a current density of  $0.25 \text{ A cm}^{-2}$ . The white boxes represent the zooms for the rib/channel analysis.

### 7.3.2 Numerical Water Transport through the Membrane

The numerical water fluxes through the membrane is presented in Fig. III-13, which are the result of the average between the electro-osmotic drag (Fig. III-13a) and molecular diffusion (Fig. III-13b). The total flux can be seen in Fig. III-13c. In this figure, the positive values represent the flux from the anode to the cathode while the negative values represent the opposite flux. Therefore, the electro-osmotic flux only drives the water from the anode to the cathode whereas the diffusive flux can proceed in both directions according to the concentration of water in the cell. Moreover, the anode GDE is dried close to the hydrogen inlet due to an important

diffusive flux (Fig. III-13b) because of a rather low relative humidity (50%) for the moist hydrogen at the inlet. This diffusion also induces a local drying of the cathode GDE in the same region. In our case, the diffusive flux exclusively drives the water from the cathode to the anode (only negative values in Fig. III-13b) to compensate for the electro-osmotic drag. From a general point of view, the liquid water is more present in the cathode compartment where the water is produced (Fig. III-12).

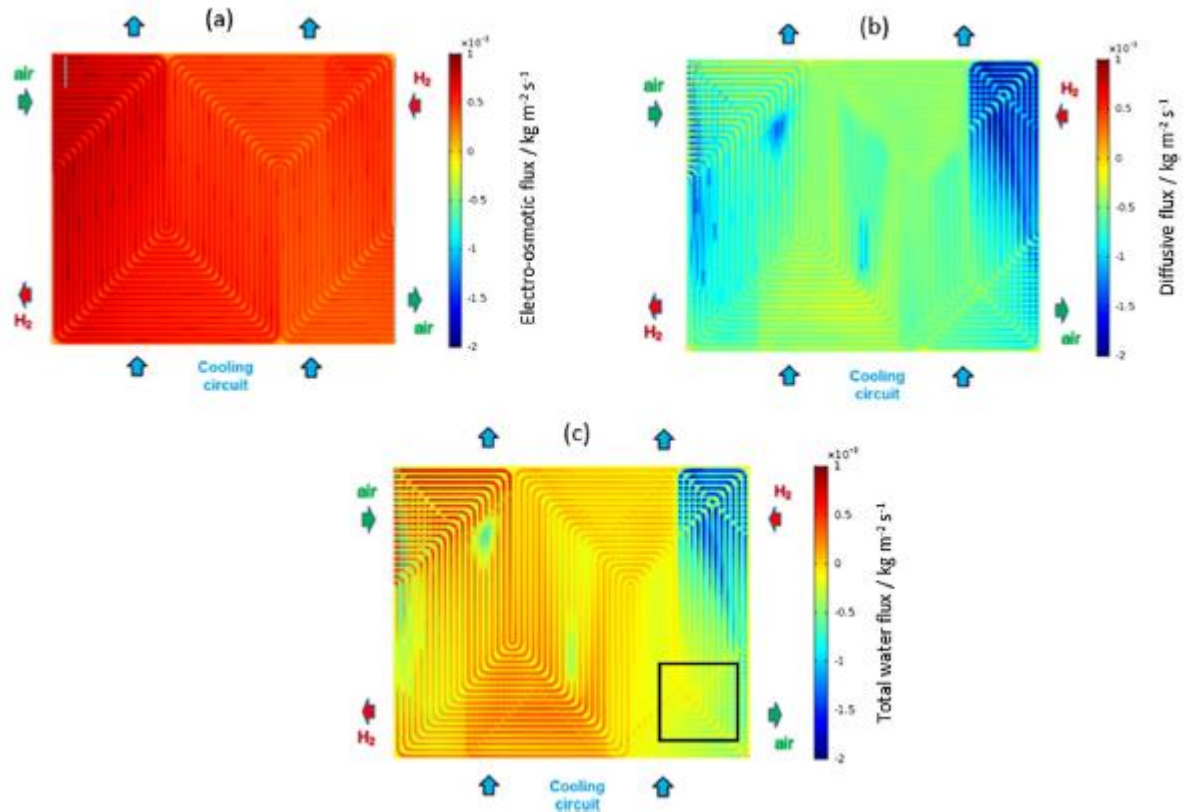


Fig. III-13. Water fluxes through the membrane: (a) Electro-osmotic flux - (b) Diffusive flux - (c) Total water flux (Electro-osmotic flux + Diffusion). The black box represent the zoom for the rib/channel analysis.

### 7.3.3 Water Distribution at Rib/Channel Scale

The saturation is plotted along the indicated reference cut line at 25% of the cell (Fig. E-1 in Appendix E), perpendicularly to the cooling water mainstream that corresponds to the air outlet (from  $x$  (active area length) = 12 to  $x$  = 16.3 cm) in Fig. III-14. It is observed at the rib/channel scale in the anode/cathode GCs and GDEs in order to study the water distribution and spatial

heterogeneities. The saturation is considered positive at the anode side (fatter red curves in Fig. III-14ab) and negative at the cathode side (fatter blue curves) represented by the scale on the left. The right scale represents the real flow-field design where the bipolar plate pattern is illustrated with channels in white and ribs in gray.

In Fig. III-14a, the liquid water is concentrated inside the gas channels at both the anode and cathode side, which is an expected result since we specifically plot the amount of water in the GC. Furthermore, there is no water or very little from  $x$  (active area length) = 15.3 to  $x$  = 16.3 cm on the anode side corresponding to the end of the air outlet. In the GDE (Fig. III-14b) on both sides, the liquid water accumulates preferentially under the rib. The region underneath the rib in the GDLs is globally colder than the region under the channel as observed by Straubhaar et al. [155], which may explain a higher condensation in this area. Liquid water is still found in the cathode GDE close to the outlet (from  $x$  = 14.1 to the end in Fig. III-14b) where oscillations can be observed along/under a single rib in front of several anode ribs and channels. Therefore, the rib/channel pattern on the anode side directly affects the amount of liquid water on the cathode side.

Fig. III-14c represents the total water flux, which is also impacted by the design of the cell. Indeed, the flux is strongly oscillating at the air outlet, where a succession of gas channels and rib on the anode side face a single rib on the cathode side. The flux is less important under the rib considering the anode pattern. Finally, the total flux is negative, i.e. that the liquid water moves from the cathode to the anode by diffusion due to a higher liquid water concentration on the cathode side.

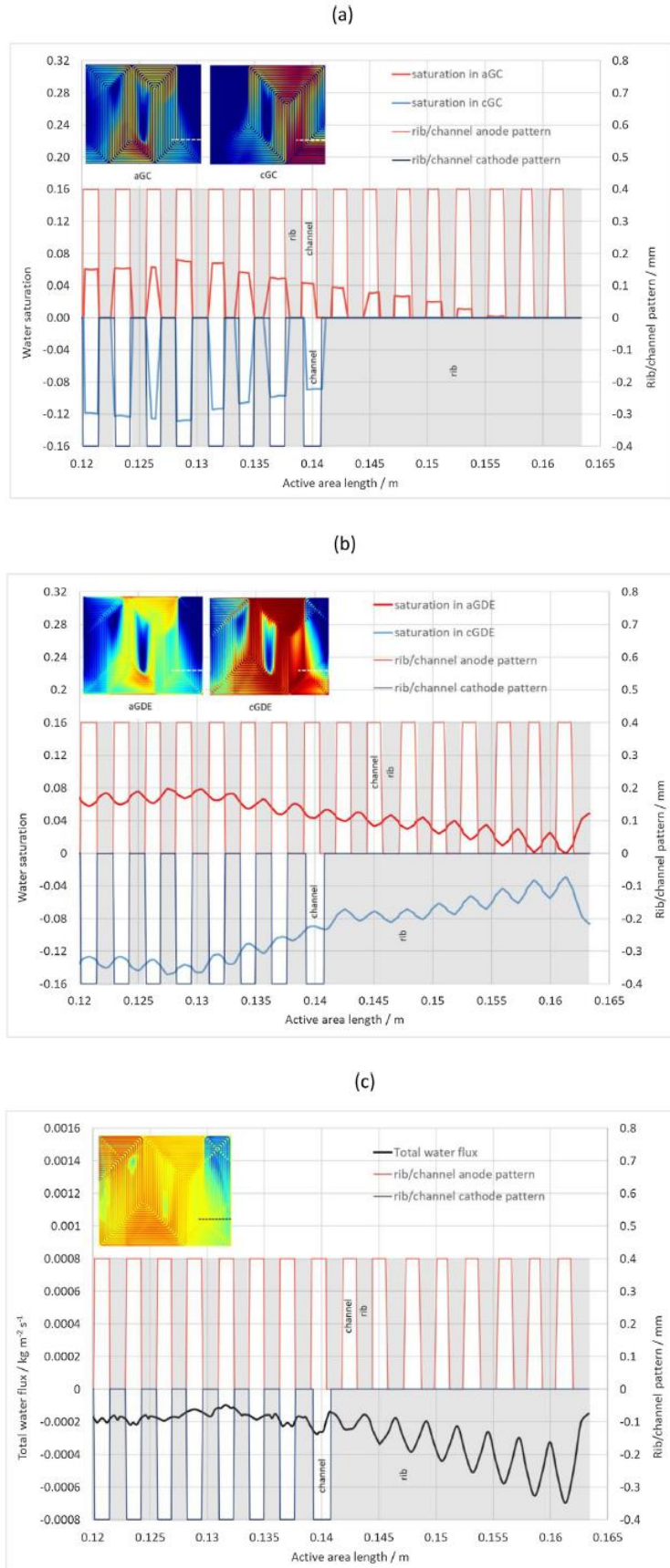


Fig. III-14. Water thickness: (a) at the air outlet in GC – (b) at the air outlet in GDE – (c) Total water flux for humid conditions at  $0.25 \text{ A cm}^{-2}$  at the indicated 25% cut line (Appendix E).

## 7.4 High Power Operating Conditions

In this section, the distribution and quantity of liquid water is compared between experimental and numerical results for the same five cells stack for operating conditions at higher temperature, i.e. 80 °C while keeping the other conditions (pressure, stoichiometry and relative humidity) than for the humid case (Table III-5) at a low current density (0.25 A/cm<sup>2</sup>). This study corresponds to more realistic temperature operation in a higher power automotive application (generally between 80 and 95 °C). Fig. III-15 represent the liquid water mappings for drier operating conditions mentioned for experimental (Fig. III-15a) and simulated (Fig. III-15b) results. At the whole cartography scale, it can be stated that the model can predict the liquid water distribution. Nevertheless, the water content obtained with the model is underestimated, especially at the air outlet.

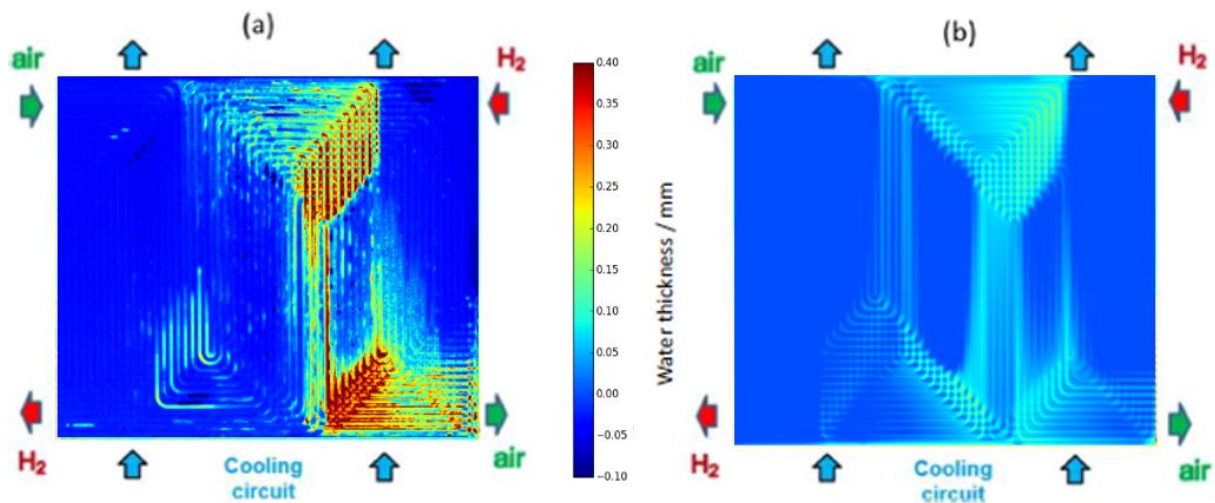


Fig. III-15. (a) measured and (b) simulated water thickness mappings in drier operating conditions – temperature of 80°C.

Even drier conditions were tested, i.e. at higher temperature and current density and lower relative humidity for the inlet gases. The model is then no longer able to quantify or locate the liquid water in the stack. For these reasons, a two-phase model, called Euler–Euler, describing the equations for each phase (presented in Chapter II) was developed. The two-phase model is the subject of the next chapter.

## Conclusion

In this chapter, a pseudo-3D multiphysics model based on a previous work [138] was developed to predict the temperature and water distributions on a large area PEMFC. The model has been first validated for temperature and current density distributions [138]. In this study, a condensation model was implemented in the commercial software COMSOL Multiphysics® to investigate the liquid water distribution. The numerical results were compared to experimental tests by neutron imaging in order to validate the two-phase flow model. Two current densities under humid operating conditions (low temperature) were simulated to analyze the liquid water heterogeneities. The model is less accurate for higher current density for which there is less liquid water. Nonetheless, the model is able to accurately locate and quantify the liquid water in the cell at lower current density. In addition, the distribution is highly dependent on the local temperature, which is directly related to the design of the cooling circuit also confirmed in [138]. Once the model was validated for these conditions, the liquid water distribution over the cell surface was studied in each layer in order to understand the water transport mechanisms through the membrane. It appears that the liquid water further accumulates in the cold zones and near the air outlet. Moreover, a sensitivity analysis was performed on the electro-osmotic drag and membrane diffusion coefficients. Despite a similar general distribution, there may be large variations of the liquid water quantity in the stack according to different transport coefficients. These coefficients appears to be key elements in the complex modeling of the water transport through the membrane. Furthermore, a study was conducted at the rib/channel scale at low density current. It shows that the liquid water takes place preferentially under the rib, which confirms the results of Straubhaar et al. [155]. The BPs design plays also an important role on the water distribution by impacting the water transport at a local scale. However, the one-fluid model largely underestimates the amount of liquid water for a high power (dry) operating conditions. Therefore, a two-fluid flow model describing the conservation equations for both liquid and gas phases seems required to simulate higher power operating conditions in an automobile application.

**Chapter IV**  
**TWO-FLUID MODEL**

## Introduction

The two-phase flow equations (Chapter II-4) are implemented in COMSOL Multiphysics® using the pseudo-3D formulation. A new flow-field design, described in this chapter, with higher performance than the F-geometry described in Chapter III-4, is simulated. Numerical two-fluid model simulation results are confronted to neutron imaging tests for two different automotive operating conditions and compared to the results obtained with the one-fluid model. In addition, the liquid water distribution and thickness are analyzed in each layer. Finally, some numerical difficulties encountered in the two-phase complex modeling are discussed.

### 1. Pseudo-3D Formulation

Similarly to the one-fluid equations, the conservation equations are integrated along the component thickness to obtain the P3D formulation for a two-phase flow. The integration of the mass equation leads to:

$$\int_0^e \left( \frac{\partial}{\partial t} [\varepsilon \alpha_k \langle \rho_k \rangle_k] \right) dz + \int_0^e \left( \nabla_{3D} \cdot [\varepsilon \alpha_k \langle \rho_k \rangle_k \underline{\overline{V}}_k^k] \right) dz = \int_0^e S_k dz + \int_0^e \Gamma_k^{lk} dz \quad (IV-1)$$

The differential operator  $\nabla_{3D}$  and the fluid-velocity vector  $\underline{\overline{V}}_k^k$  are decomposed into the three-dimensional Cartesian coordinate system to obtain:

$$\begin{aligned} \int_0^e \left( \frac{\partial}{\partial t} [\varepsilon \alpha_k \langle \rho_k \rangle_k] \right) dz \\ + \int_0^e \left( \frac{\partial}{\partial x} [\varepsilon \alpha_k \langle \rho_k \rangle_k \overline{u}_k^k] + \frac{\partial}{\partial y} [\varepsilon \alpha_k \langle \rho_k \rangle_k \overline{v}_k^k] \right. \\ \left. + \frac{\partial}{\partial z} [\varepsilon \alpha_k \langle \rho_k \rangle_k \overline{w}_k^k] \right) dz = S_k e + \Gamma_k^{lk} e \end{aligned} \quad (IV-2)$$

where  $\overline{u}_k^k$ ,  $\overline{v}_k^k$  and  $\overline{w}_k^k$  are the Favre-average phase-phase velocity according to x, y, and z directions, respectively. The electrochemical  $S_k$  and phase change  $\Gamma_k^{lk}$  source terms are considered constant over the thickness. Furthermore, the integrals are swapped with the differential operators. Finally, each term is divided by the component thickness leading to:

$$\begin{aligned} \frac{\partial}{\partial t} \left( \frac{1}{e} \int_0^e [\varepsilon \alpha_k \langle \rho_k \rangle_k] dz \right) + \frac{\partial}{\partial x} \left( \frac{1}{e} \int_0^e [\varepsilon \alpha_k \langle \rho_k \rangle_k \overline{u}_k^k] dz \right) \\ + \frac{\partial}{\partial y} \left( \frac{1}{e} \int_0^e [\varepsilon \alpha_k \langle \rho_k \rangle_k \overline{v}_k^k] dz \right) + \frac{1}{e} [\varepsilon \alpha_k \langle \rho_k \rangle_k \overline{w}_k^k]_0^e = S_k + \Gamma_k^{lk} \end{aligned} \quad (\text{IV-3})$$

As a reminder, the porosity is assumed constant over the entire volume. Under this assumption, we have:

$$\frac{1}{e} \int_0^e [\varepsilon \alpha_k \langle \rho_k \rangle_k] dz = \varepsilon \frac{1}{e} \int_0^e \alpha_k \langle \rho_k \rangle_k dz \quad (\text{IV-4})$$

$$\frac{1}{e} \int_0^e [\varepsilon \alpha_k \langle \rho_k \rangle_k \overline{u}_k^k] dz = \varepsilon \frac{1}{e} \int_0^e \alpha_k \langle \rho_k \rangle_k \overline{u}_k^k dz \quad (\text{IV-5})$$

$$\frac{1}{e} \int_0^e [\varepsilon \alpha_k \langle \rho_k \rangle_k \overline{v}_k^k] dz = \varepsilon \frac{1}{e} \int_0^e \alpha_k \langle \rho_k \rangle_k \overline{v}_k^k dz \quad (\text{IV-6})$$

where the local thickness-average  $\frac{1}{e} \int_0^e \psi dz$  can be recognized. Considering a small thickness, the average of a product is equal to the product of the averages since the k-phase density and k-phase velocities according to x and y directions are considered constant over the thickness. Finally, the pseudo-3D description for the mass equation is expressed by:

$$\frac{\partial}{\partial t} [\varepsilon \alpha_k \langle \rho_k \rangle_k] + \nabla_{2D} \cdot [\varepsilon \alpha_k \langle \rho_k \rangle_k \overline{\underline{V}}_{k,e}^k] + \frac{J_{\text{conv}}^+}{e} + \frac{J_{\text{conv}}^-}{e} = S_k + \Gamma_k^{lk} \quad (\text{IV-7})$$

$\overline{\underline{V}}_{k,e}^k = \overline{u}_k^k \underline{e}_x + \overline{v}_k^k \underline{e}_y$  being the in-plane k-phase velocity.  $J_{\text{conv}}^+$  and  $J_{\text{conv}}^-$  are the convective mass-fluxes across the interfaces of the different components described by:

$$\frac{J_{\text{conv}}^+}{e} = \frac{1}{e} \varepsilon \alpha_k \langle \rho_k \rangle_k \overline{w}_k^k \Big|_e \quad (\text{IV-8})$$

$$\frac{J_{\text{conv}}^-}{e} = -\frac{1}{e} \varepsilon \alpha_k \langle \rho_f \rangle_f \overline{w}_k^k \Big|_0 \quad (\text{IV-9})$$

The same development is applied to the species (IV-10) conservation equation:

$$\begin{aligned} \frac{\partial}{\partial t} [\varepsilon \alpha_k \langle \rho_{jk} \rangle_{k,e}] + \nabla_{2D} \cdot [\varepsilon \alpha_k \langle \rho_{jk} \rangle_{k,e} \overline{\underline{\underline{V}}}_{k,e}^k] + \frac{J_{conv,j}^+}{e} + \frac{J_{conv,j}^-}{e} \\ = \nabla_{2D} \cdot [D_{m_j} \nabla_{2D} (\varepsilon \alpha_k \langle \rho_{jk} \rangle_{k,e})] + \frac{J_{diff,j}^+}{e} + \frac{J_{diff,j}^-}{e} + S_{jk} + \Gamma_{jk}^{Ik} \end{aligned} \quad (IV-10)$$

where the same assumptions are retained for these equations as for the mass balance. Other assumptions are needed in the pseudo-3D writing of species conservation equation. The variations of the mass diffusion coefficient  $D_{m_j}$  is assumed negligible over the volume. Similar to the convective mass-fluxes across the interfaces of the different components,  $J_{diff,j}^+$ ,  $J_{diff,j}^-$  represent the through-plane diffusive mass-fluxes of the  $j$ -specie.

## 2. Two-Fluid Equations

### 2.1 Model Presentation

The equations implemented in the two-fluid model are listed in Table IV-1 by considering the gas channels as porous media to reduce the momentum equation to the extended two-phase Darcy's law. The energy equation in the gas channels is described by the homogeneous approach briefly presented in Chapter I. Indeed, a single temperature of the fluid mixture is calculated by the model. This approach was chosen due to lack of experimental proof and to avoid a long computation time by solving an energy equation for each phase. Eventually, it is difficult to implement the complex two-phase energy theory for which it would be necessary to find coherent closure laws for the thermal non-equilibrium terms. The energy balance for each phase are summed to obtain one energy equation of the fluid mixture:

$$\begin{aligned} \frac{\partial}{\partial t} [(\alpha_l \langle \rho_l \rangle_{l,e} c_{p_l} + \alpha_g \langle \rho_g \rangle_{g,e} c_{p_g}) \overline{\underline{\underline{T}}}_{f,e}^f] + \nabla_{2D} \\ \cdot [(\alpha_l \langle \rho_l \rangle_{l,e} c_{p_l} \overline{\underline{\underline{V}}}_{l,e}^l + \alpha_g \langle \rho_g \rangle_{g,e} c_{p_g} \overline{\underline{\underline{V}}}_{g,e}^g) \overline{\underline{\underline{T}}}_{f,e}^f] \\ = \nabla \cdot [k_f^{eff} \nabla_{2D} (\overline{\underline{\underline{T}}}_{f,e}^f)] + \frac{J_{diff,T}^+}{e_{GC}} + \frac{J_{diff,T}^-}{e_{GC}} \end{aligned} \quad (IV-11)$$

where  $\overline{\underline{\underline{T}}}_{f,e}^f$  refers to the in-plane temperature of the fluid mixture and  $k_f^{eff}$ , the effective thermal conductivity of the fluid mixture given:

$$k_f^{\text{eff}} = \alpha_l k_l^{\text{eff}} + \alpha_g k_g^{\text{eff}} \quad (\text{IV-12})$$

where  $k_l^{\text{eff}}$  and  $k_g^{\text{eff}}$  denote the effective liquid and gas thermal conductivity, respectively. Thermal non-equilibrium between the fluid phases is therefore not represented in Eq. (IV-11). Indeed, what one phase thermally gains is lost by the other, which means that the non-equilibrium between phases compensate each other when the thermal equations of the liquid and gas phase are added to form the homogeneous thermal equation. The electrochemical model implemented in the two-fluid model is similar to the one in the 1-F model.

## 2.2 Source Terms

The source terms of water production and reactants consumption by electrochemical reactions are the same as in the one-fluid model but applied to the gas phase only. Consequently, the water production is considered in vapor form:

- at the cathode side

$$S_{k=g} = S_{\text{O}_2} + S_{\text{H}_2\text{O}} \quad (\text{IV-13})$$

- at the anode side

$$S_{k=g} = S_{\text{H}_2} \quad (\text{IV-14})$$

- on both sides

$$S_{k=l} = 0 \quad (\text{IV-15})$$

The heat source terms have already been described in Chapter III and reused here. It is now necessary to define closure laws concerning the mass transfer between the liquid and gas phases. Phase change in macro-average modeling, namely  $S_{\text{cond}}$  for the condensation and  $S_{\text{evap}}$  for the evaporation, can be represented by assuming the mass transfer to be driven by the difference between the vapor partial and saturation pressures, as implemented in COMSOL Multiphysics [156]:

$$\begin{cases} S_{\text{cond}} = H_{\text{cond}} (P_{\text{H}_2\text{O}} - P_{\text{sat}}(T)) & \text{if } P_{\text{H}_2\text{O}} > P_{\text{sat}}(T) \\ S_{\text{evap}} = H_{\text{evap}} (P_{\text{sat}}(T) - P_{\text{H}_2\text{O}}) & \text{if } P_{\text{H}_2\text{O}} < P_{\text{sat}}(T) \text{ and } \alpha_1 > 0 \end{cases} \quad (\text{IV-16})$$

where  $H_{\text{cond}}$  and  $H_{\text{evap}}$  are the evaporation and condensation rates, respectively, which both take the value of 1 s/m<sup>2</sup> corresponding to rather high rates. This value is arbitrarily selected to remain close to the equilibrium with a limited impact on the calculation time. Finally, the phase change is implemented such as one phase immediately wins the mass lost by the other one:

$$\begin{cases} \Gamma_1^{\text{II}} = S_{\text{cond}} - S_{\text{evap}} \\ \Gamma_g^{\text{Ig}} = S_{\text{evap}} - S_{\text{cond}} \end{cases} \quad (\text{IV-17})$$

**Table IV-1**

Governing equations

Component	Conservation equation	General form		
GCs	Mass	$\frac{\partial}{\partial t} [\alpha_k \langle \rho_k \rangle_k] + \nabla_{2D} \cdot [\alpha_k \langle \rho_k \rangle_k \overline{\underline{V}}_{k,e}^k] + \frac{J_{conv}^+}{e_{GC}} + \frac{J_{conv}^-}{e_{GC}} = S_k + \Gamma_k^{lk}$	(A)	
	Momentum	$\overline{\underline{V}}_{k,e}^k = -\frac{K_{GC} K_{rk}}{\alpha_k \mu_k} \nabla \langle p_k \rangle_k$	(B)	
	Species	$\frac{\partial}{\partial t} [\alpha_k \langle \rho_{jk} \rangle_{k,e}] + \nabla_{2D} \cdot [\alpha_k \langle \rho_{jk} \rangle_{k,e} \overline{\underline{V}}_{k,e}^k] + \frac{J_{conv,j}^+}{e_{GC}} + \frac{J_{conv,j}^-}{e_{GC}} = \nabla_{2D} \cdot [D_{m_j} \nabla_{2D} (\alpha_k \langle \rho_{jk} \rangle_{k,e})] + \frac{J_{diff,j}^+}{e_{GC}} + \frac{J_{diff,j}^-}{e_{GC}} + S_{jk} + \Gamma_{jk}^{lk}$	(C)	
	Energy	$\frac{\partial}{\partial t} [(\alpha_l \langle \rho_l \rangle_{l,e} c_{pl} + \alpha_g \langle \rho_g \rangle_{g,e} c_{pg}) \overline{\underline{T}}_{f,e}^f] + \nabla_{2D} \cdot [(\alpha_l \langle \rho_l \rangle_{l,e} c_{pl} \overline{\underline{V}}_{l,e}^l + \alpha_g \langle \rho_g \rangle_{g,e} c_{pg} \overline{\underline{V}}_{g,e}^g) \overline{\underline{T}}_{f,e}^f] = \nabla \cdot [k_f^{eff} \nabla_{2D} (\overline{\underline{T}}_{f,e}^f)] + \frac{J_{diff,T}^+}{e_{GC}} + \frac{J_{diff,T}^-}{e_{GC}}$	(D)	
GDEs	Mass	$\frac{\partial}{\partial t} [\varepsilon_{GDE} \alpha_k \langle \rho_k \rangle_k] + \nabla_{2D} \cdot [\varepsilon_{GDE} \alpha_k \langle \rho_k \rangle_k \overline{\underline{V}}_{k,e}^k] + \frac{J_{conv}^+}{e_{GDE}} + \frac{J_{conv}^-}{e_{GDE}} = S_k + \Gamma_k^{lk}$	(E)	
	Momentum	$\overline{\underline{V}}_{k,e}^k = -\frac{K_{GDE} K_{rk}}{\varepsilon_{GDE} \alpha_k \mu_k} \nabla \langle p_k \rangle_k$	(F)	
	Species	$\frac{\partial}{\partial t} [\varepsilon_{GDE} \alpha_k \langle \rho_{jk} \rangle_{k,e}] + \nabla_{2D} \cdot [\varepsilon_{GDE} \alpha_k \langle \rho_{jk} \rangle_{k,e} \overline{\underline{V}}_{k,e}^k] + \frac{J_{conv,j}^+}{e_{GDE}} + \frac{J_{conv,j}^-}{e_{GDE}} = \nabla_{2D} \cdot [D_{m_j} \nabla_{2D} (\varepsilon_{GDE} \alpha_k \langle \rho_{jk} \rangle_{k,e})] + \frac{J_{diff,j}^+}{e_{GDE}} + \frac{J_{diff,j}^-}{e_{GDE}} + S_{jk} + \Gamma_{jk}^{lk}$	(G)	
	Energy	GDLs	$\frac{\partial}{\partial t} [(1 - \varepsilon_{GDL}) \rho_{GDL} c_{pGDL} \overline{\underline{T}}_{GDL,e}^{GDL}] - \nabla \cdot [k_{GDL} \nabla_{2D} ((1 - \varepsilon_{GDL}) \overline{\underline{T}}_{GDL,e}^{GDL})] = \frac{J_{diff,T}^+}{e_{GDL}} + \frac{J_{diff,T}^-}{e_{GDL}} + Q_T$	(H)
		MPLs	$\frac{\partial}{\partial t} [(1 - \varepsilon_{MPL}) \rho_{MPL} c_{pMPL} \overline{\underline{T}}_{MPL,e}^{MPL}] - \nabla \cdot [k_{MPL} \nabla_{2D} ((1 - \varepsilon_{MPL}) \overline{\underline{T}}_{MPL,e}^{MPL})] = \frac{J_{diff,T}^+}{e_{MPL}} + \frac{J_{diff,T}^-}{e_{MPL}} + Q_T$	(I)
		CLs	$\frac{\partial}{\partial t} [(1 - \varepsilon_{CL}) \rho_{CL} c_{pCL} \overline{\underline{T}}_{CL,e}^{CL}] - \nabla \cdot [k_{CL} \nabla_{2D} ((1 - \varepsilon_{CL}) \overline{\underline{T}}_{CL,e}^{CL})] = \frac{J_{diff,T}^+}{e_{CL}} + \frac{J_{diff,T}^-}{e_{CL}} + Q_T + S_T$	(J)
CW channels	Mass	$\nabla_{2D} \cdot \langle \underline{V}_{cw} \rangle_{f,e} = 0$	(K)	
	Momentum	$\rho_{cw} \frac{\partial}{\partial t} \langle \underline{V}_{cw} \rangle_{f,e} + \rho_{cw} (\langle \underline{V}_{cw} \rangle_{f,e} \cdot \nabla_{2D}) \langle \underline{V}_{cw} \rangle_{f,e} = -\nabla_{2D} p_{cw} + \nabla_{2D} \cdot [\mu_{cw} (\nabla_{2D} \langle \underline{V}_{cw} \rangle_{f,e} + \nabla_{2D}^T \langle \underline{V}_{cw} \rangle_{f,e})] + \frac{\mu_{cw}}{K} \langle \underline{V}_{cw} \rangle_{f,e} + \frac{1}{K_2} \ \langle \underline{V}_{cw} \rangle_{f,e}\  \langle \underline{V}_{cw} \rangle_{f,e} + \rho_{cw} \mathbf{g}$	(L)	
	Energy	$\rho_{cw} c_{p_{cw}} \frac{\partial \langle T_{cw} \rangle_{f,e}}{\partial t} + \nabla_{2D} \cdot [\rho_{cw} c_{p_{cw}} \langle \underline{V}_{cw} \rangle_{f,e} \langle T_{cw} \rangle_{f,e}] = \nabla \cdot [k_{cw}^{eff} \nabla_{2D} \langle T_{cw} \rangle_{f,e}] + \frac{J_{diff,T}^+}{e_{cw}} + \frac{J_{diff,T}^-}{e_{cw}}$	(M)	

### 3. Stack Design

In this chapter, a new flow-field design (Fig. IV-1), has been experimentally tested. Indeed, as seen previously, the liquid water distribution was mainly dependent on the temperature induced by the design of the cooling circuit inside the F-design bipolar plate. These strong heterogeneities were responsible for serious degradation and performance drops [71]. Conversely, the new flow-field design avoids hot spots in the active area with quite low temperature gradient along the cell length.

As seen on Fig. IV-1a, the fluids flow in the same direction in numerous undulating parallel channels. Therefore, it can be considered that a few channels are representative of the entire active area. A reduced geometry composed of only a few channels is modeled and simulated (Fig. IV-1b). A simplified gas distributor for both hydrogen and air inlets has been designed in the two-fluid model to simplify the boundary conditions to be implemented, considering a counter-current flow.

A dedicated stack composed of 3 cells has been built for neutron imaging measurement. Bipolar plates are made of stamped stainless steel with undulating parallel channels (Fig. IV-1) and low neutron absorption gilded aluminum end-plates. It comprises commercial Membrane Electrode Assembly composed of 15  $\mu\text{m}$  thick reinforced perfluorosulfonic acid membrane, Pt based Catalyst Layer with total loading of 0.4  $\text{mg}/\text{cm}^2$ , Freudenberg Gas Diffusion Layer including Micro-Porous Layer with a compressed thickness of 150  $\mu\text{m}$  on both sides. Heavy water is used as coolant because of its low neutron absorption. The geometrical parameters are listed in Table IV-2.

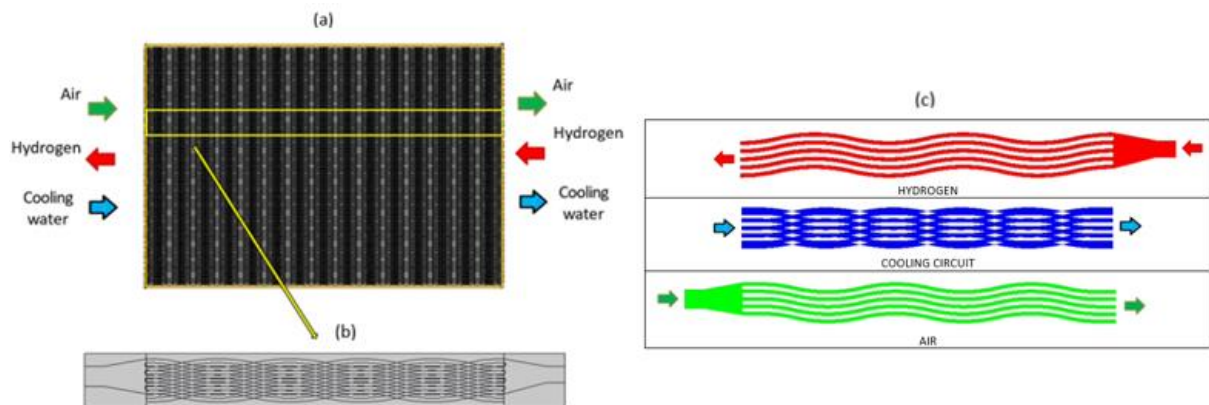


Fig. IV-1. (a) Reference geometry of the 3 cells stack – (b) Reduced geometry modeled – (c) Flow-field design: hydrogen, cooling circuit and air.

**Table IV-2**

Geometrical parameters

Component thickness		Value [ $\mu\text{m}$ ]
Bipolar Plate		200
Gas Channel depth	Anode	200
	Cathode	300
Gas Diffusion Layer (+ MPL)	Anode	150
	Cathode	150
Catalyst Layer	Anode	6
	Cathode	10
Membrane		15

## 4. Numerical Procedure

### 4.1 Preliminary Simulation with a 1D Model

A one-dimensional model (Fig. IV-2) was first developed to simulate the two-phase flow in a gas channel at the cathode side considering an isothermal process. The general form of Partial Differential Equations (PDEs) were used from the basic functionalities of the COMSOL Multiphysics® software to implement the two-fluid dynamic equations. The 1D model is composed of three sections where the ORR takes place only in the central section (Fig. IV-2). Many numerical problems were encountered during the modeling. First, the underlying finite element discretization method in COMSOL Multiphysics® is the Galerkin method, which becomes unstable for a Péclet number greater than one. The Péclet number, as a dimensionless number, represents the ratio between the convection and diffusion transport. From a classic convection-diffusion transport equation:

$$\frac{\partial \psi}{\partial t} + \underline{V} \cdot \nabla \psi = \nabla \cdot (D \nabla \psi) + S \quad (\text{IV-18})$$

where  $\psi$  is a transported scalar,  $\underline{V}$ , the convective velocity vector,  $D$ , the diffusion coefficient and  $S$ , a source term, the Péclet number is noted [157]:

$$P_e = \frac{\|V\|h}{2D} \quad (\text{IV-19})$$

where  $h$  is the mesh element size. If the convective effects dominate over the diffusive effects represented by a large Péclet number, numerical instabilities occur in the form of significant oscillations (Fig. IV-3) [158]. When considering the mass balance for the liquid phase (see section II-4.5), it appears that the Galerkin criterion cannot be respected. It is then necessary to add an artificial diffusion in the equation to achieve convergence. Accordingly, there is – in theory – a mesh resolution to match the diffusion term in order to reach a stable discretization ( $P_e < 1$ ). However, adding a non-physical diffusion necessarily alters the results especially if a high diffusion is implemented by “smoothing” the results. To keep consistent results, the diffusion coefficient should be as low as possible, which requires a very dense mesh. For example, considering a liquid phase velocity of  $1 \cdot 10^{-4}$  m/s [90] in the gas channels and a diffusion coefficient of  $5 \cdot 10^{-10}$  m<sup>2</sup>/s in order to get precise results, the size of a mesh element is 10  $\mu$ m to have a Péclet number equal to one. Around  $15 \cdot 10^6$  elements would be needed to mesh the reduced geometry presented in Fig. IV-1b. As a result, it is – in practice – impossible to simulate a large area cell with a mesh element about the size of a pore. Consequently, a reasonable compromise between accurate results and processing time is a difficult task to achieve.

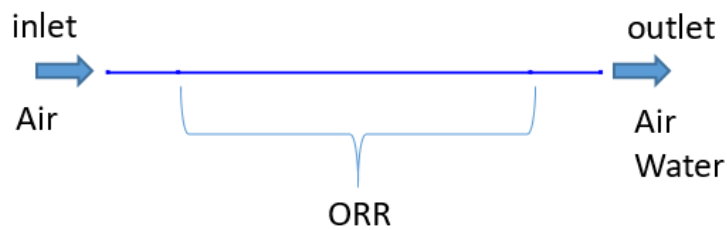


Fig. IV-2. 1D model of a cathode gas channel.

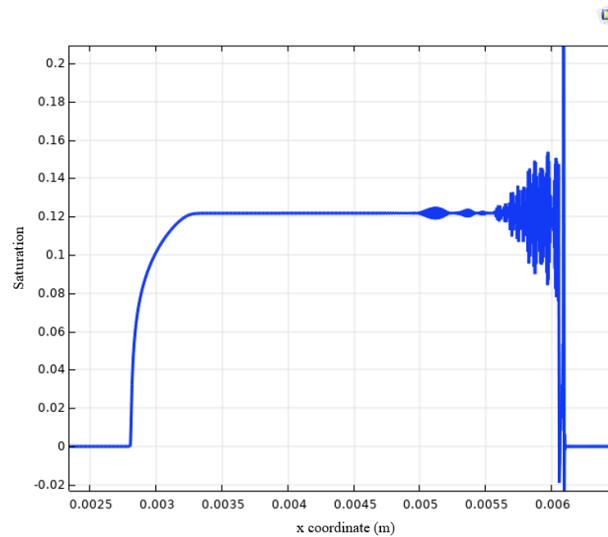


Fig. IV-3. Numerical oscillations when plotting the saturation with the 1D model at a cathode gas channel.

To go further, a sensitivity study to the diffusion coefficient while keeping the same number of mesh elements was carried out using the 1D model to analyze the impact on the convergence and the results accuracy. The element size is  $4.2 \mu\text{m}$  and the maximum velocity of the liquid phase obtained with the model is  $1.4 \cdot 10^{-4} \text{ m/s}$ . The time step and saturation are plotted in Fig. IV-4 and Fig. IV-5, respectively, according to different Péclet numbers / diffusion coefficients (from  $1 \cdot 10^{-8}$  to  $5 \cdot 10^{-11} \text{ m}^2/\text{s}$ ). As expected, the lower the Péclet number (the higher the diffusion coefficient), the faster the convergence (Fig. IV-4). Note that the model converges for Péclet numbers greater than one (Fig. IV-4). The model did not converge for a coefficient of  $1 \cdot 10^{-11} \text{ m}^2/\text{s}$ , i.e. a Péclet number close to 30. However, the higher the diffusion coefficient, the more the liquid water profile is smoothed (Fig. IV-5). The diffusion coefficient does not affect too much the 1D model results but strongly the pseudo-3D model ones, where the mesh size cannot be reduced sufficiently.

A module dedicated to fuel cells has recently been added to the COMSOL Multiphysics® software (Fuel Cell & Electrolyzer Module [159]). Some stabilizations can be integrated to improve the model convergence while maintaining consistent results. Fig. IV-6 shows the saturation (in blue) and the relative humidity (in green) of the air obtained with this new module used in the 1D model without adding artificial diffusion “by hand”. The appearance of liquid water ( $s > 0$  in the blue curve) coincides absolutely with the water vapor saturated air (relative humidity equal to 100% in the green curve).

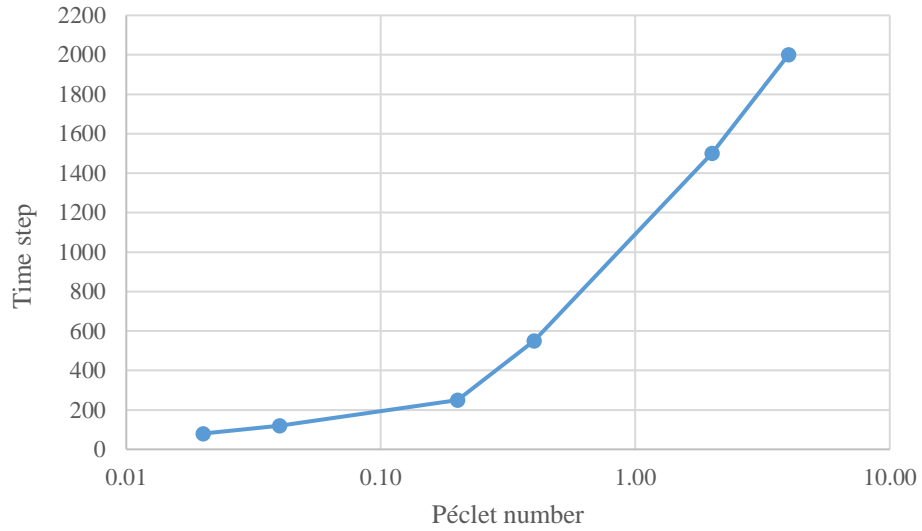


Fig. IV-4. Time step processing according to different Péclet numbers (diffusion coefficient from  $1 \cdot 10^{-8}$  to  $5 \cdot 10^{-11}$  m<sup>2</sup>/s) from the 1D model.

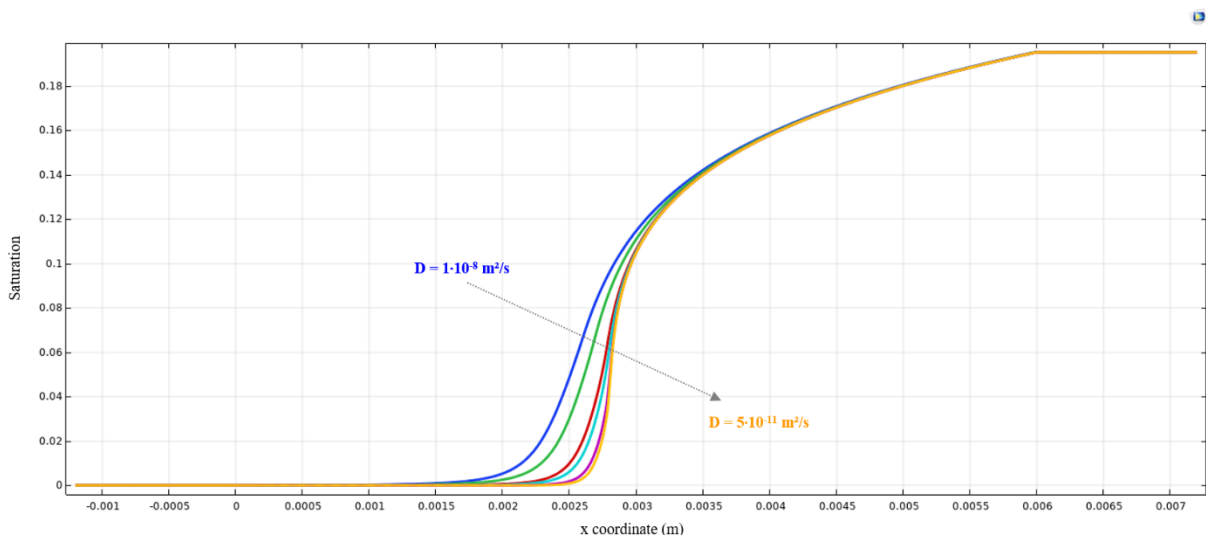


Fig. IV-5. Saturation obtained with the 1D model according to different diffusion coefficients (from  $1 \cdot 10^{-8}$  to  $5 \cdot 10^{-11}$  m<sup>2</sup>/s).

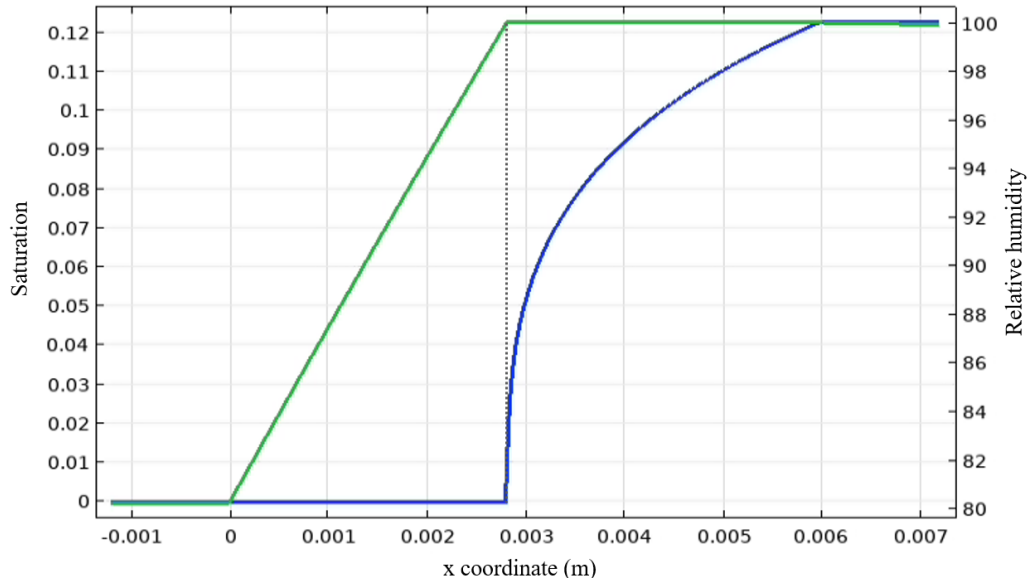


Fig. IV-6. Relative humidity (in green) and saturation (in blue) with the 1D model using the Fuel Cell & Electrolyzer module [159] in COMSOL Multiphysics®.

#### 4.2 Meshing and Resolution with the Pseudo-3D Model

Once the model feasibility validated with the 1D model, the governing equations are discretized for a representative geometry by the finite element method and solved by the 5.6 version of the COMSOL Multiphysics® software. The mesh is composed of 7817 elements (Fig. IV-7). The calculation time is about 7h30 on 2 x Intel® Xeon® CPU E5-2640 v4 at 2.40 GHz – use of 2 sockets with 16 cores to obtain a relative error of  $10^{-4}$  for a typical simulation of one operating condition. Direct solver is used with a MUMPS (MUltifrontal Massively Parallel Sparse direct Solver) for all physics. The simulation is divided in several steps, solving different physical problems, using a one-way coupling. The first step is to calculate the conservation equations of mass, species and momentum (reduced to the extended two-phase Darcy's law) in the gas channels and GDEs coupled to the electrochemical model. Heat equations in all the layers as well as fluid dynamics (mass and semi-heuristic momentum equations as described in Chapter III) in the cooling circuit are solved during the second step. A third step could be computed to solve the first step equations again from the computed temperatures obtained by the second step.

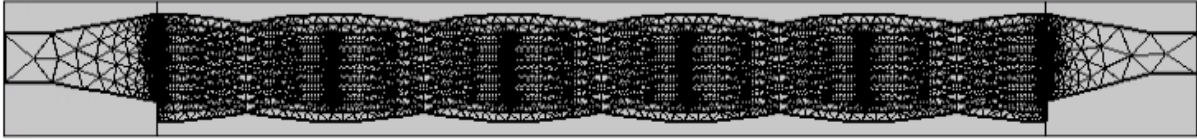


Fig. IV-7. Mesh model based on free triangle elements ( $\sim 8 \cdot 10^3$ ).

## 5. Results and discussion

### 5.1 Two-Fluid Model versus Experimental Tests

The numerical results obtained with the two-fluid model are compared to liquid water measurements by neutron imaging test (Fig. IV-8) for two different operating configurations (Table IV-3). The operating temperature is set at  $80^\circ\text{C}$  for both cases. Higher current density is considered compared to the low current density condition ( $0.25 \text{ A/cm}^2$  at  $65^\circ\text{C}$ ) described in Chapter III-7.2. As discussed before, these PEM conditions are representative of an automobile application operating at high power and for which the one-fluid model calculated unsatisfactory liquid water distribution. The plotted curves in Fig. IV-8 consider at each point the average of the liquid water thicknesses over the total width of the stack. First, the averaged liquid water thickness in the entire stack is:

- $76.2 \mu\text{m}$  (simulated) and  $87.5 \mu\text{m}$  (measured) for Setpoint No. 1 (12.9% difference)
- $68.7 \mu\text{m}$  (simulated) and  $96.4 \mu\text{m}$  (measured) for Setpoint No. 2 (28.7% difference)

Moreover, the model correctly captures the general trend of the liquid water distribution in the stack (Fig. IV-8) with a slight increase from the air inlet ( $\text{H}_2$  outlet) to the middle of the cell followed by a strong decrease until the air outlet ( $\text{H}_2$  inlet). The air outlet ( $\text{H}_2$  inlet) is almost dry. The calculated thickness is globally underestimated even if its order of magnitude remains satisfactory. The model convergence is difficult to achieve in that conditions because of liquid water accumulation in some areas where saturation is close to the unity. To mitigate these issues, two numerical strategies were implemented. First, the materials are considered as hydrophobic and the Leverett J-function is modified by a correction factor while maintaining consistent results in the lower saturation areas. In addition, the  $n_k$  coefficient in the relative permeabilities takes a value of two, because the first simulations showed that it was sufficient to evacuate the liquid water in the cell. Most authors [52][90][136][160] recommend a value of three, four or five for this parameter to better fit to the experimental tests. Unfortunately, the

model does not converge with higher values of  $n_k$ . This may explain the lower averaged values of the liquid water thickness obtained by the model (Fig. IV-8).

**Table IV-3**

Constant operating parameters.			
Experimental parameters		Setpoint No. 1	Setpoint No. 2
Inlet pressure reactant gases /bar		2.5	2
Coolant outlet temperature /°C		80.4	79.9
Coolant inlet temperature /°C		75.6	77.6
Current density /A cm <sup>-2</sup>		1.1	0.7
Stoichiometry coefficient	Hydrogen	2	1.5
	Air	1.6	1.6
Relative humidity (%)	Hydrogen	49.7	50.8
	Air	59.5	60.7

The two-fluid model is most suitable to simulate Setpoint No. 1 conditions along the entire length of the stack compared to Setpoint No. 2 conditions when confronting the numerical results (red curves in Fig. IV-8) to liquid water measures (black curves in Fig. IV-8). The simulation of a greater number of different operating conditions would be interesting to go further in the analysis of the accuracy of the model. However, in the next sections, this model is used to investigate the liquid water distribution in the different layers of the PEMFC, which is not accessible from experimental data.

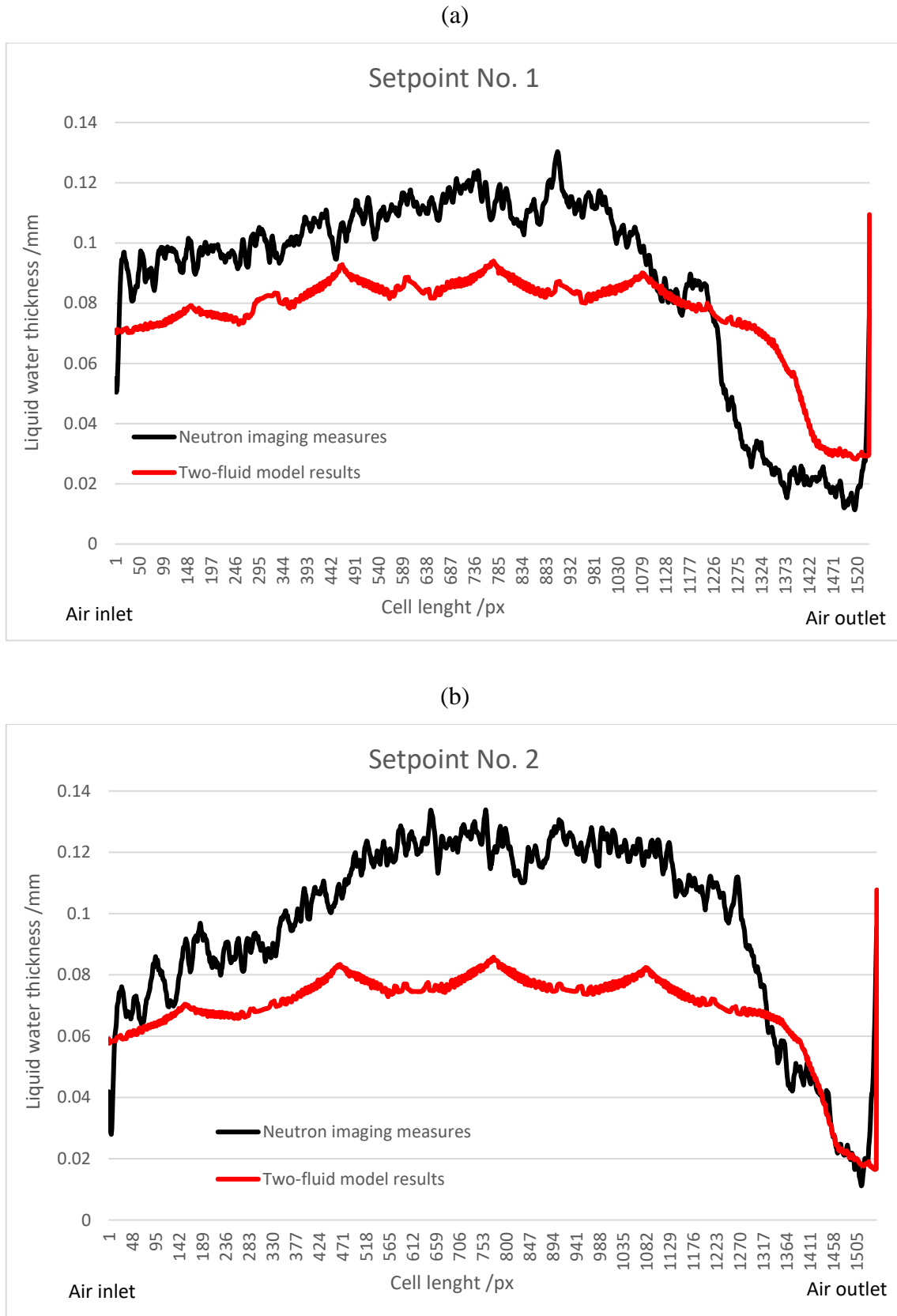


Fig. IV-8. Total averaged liquid water thickness [mm] for a stack of 3 cells for: (a) Setpoint No. 1 and (b) Setpoint No. 2 conditions (Table IV-3) from experimental (black curve) and numerical (red curve) data. The cathode inlet and anode outlet correspond to  $x=0$  and the anode inlet and cathode outlet to  $x=1547$ .

## 5.2 Two-Fluid Model versus One-Fluid Model

### 5.2.1 Total Liquid Water Comparison

Fig. IV-9 shows the simulated total water thicknesses predicted by the 1-F (blue curves) and 2-F (red curves) models for the two operation conditions presented in Table IV-3. For the entire stack, the averaged liquid water thicknesses are:

- 76.2  $\mu\text{m}$  (2-F model) and 149.3  $\mu\text{m}$  (1-F model) for Setpoint No. 1 (95.6% difference)
- 68.7  $\mu\text{m}$  (2-F model) and 146.2  $\mu\text{m}$  (1-F model) for Setpoint No. 2 (112.7% difference)

The one-fluid model largely overestimates the liquid water for both conditions compared to the two-fluid model (about two times more) and experimental tests (from 50 to 70% for the Setpoint No. 1 and Setpoint No. 2, respectively). The liquid water is particularly overestimated by the one-fluid model at the air outlet (anode inlet) while the cathode inlet (anode outlet) is slightly underestimated (Fig. IV-9).

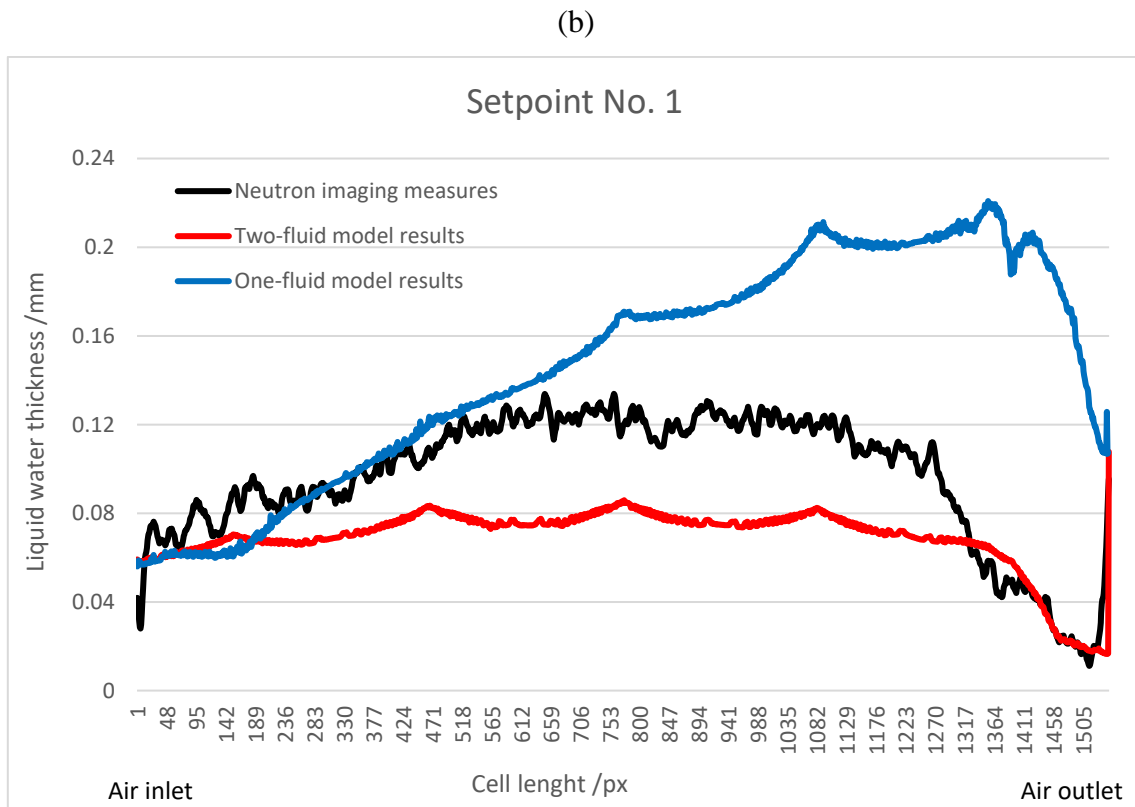
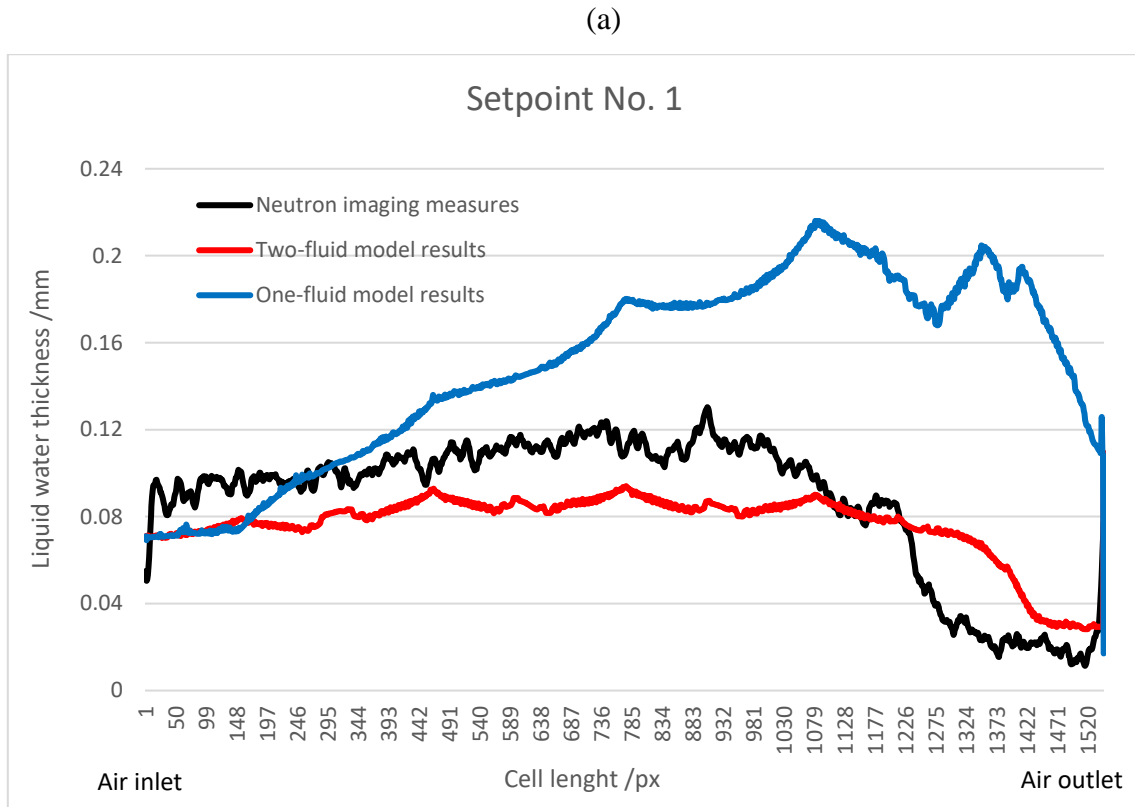


Fig. IV-9. Total averaged liquid water thickness [mm] for a stack of 3 cells for: (a) Setpoint No. 1 and (b) Setpoint No. 2 conditions (Table IV-3) from experimental (black curve), one-fluid model (blue curve) and two-fluid model (red curve) data. The cathode inlet and anode outlet correspond to  $x=0$  and the anode inlet and cathode outlet to  $x=1547$ .

### 5.2.2 Liquid Water Component Comparison

Fig. IV-10 and Fig. IV-11 show the simulated water thickness in the different components of the PEMFC obtained with both models. Note that the color scale is different for each component to compare water thicknesses simulated by the two models. It is worth mentioning that the liquid water distribution is significantly different at the component scale as at the cell scale. From a general point of view, the simulated liquid water thickness is higher in the cathode compartment (cGC–cGDE) with the one-fluid model than with the two-fluid model for both conditions (Fig. IV-10 and Fig. IV-11). Conversely, the liquid water thickness is lower in the anode compartment (aGC–aGDE) with the one-fluid model than with the two-fluid model (Fig. IV-10 and Fig. IV-11).

For the Setpoint No. 1 conditions, the thickness is about three times higher in the cathode GDE and two times lower in the anode GDE with the one fluid model. The same trend is observed for the anode and cathode gas channel. This can be related to the velocity ratio between gas and liquid phase. Indeed, on the one hand, the velocity ratios fixed with the one-fluid model, equal to the density ratio as discussed in Chapter III-4.1.1. On the other hand, it varies along the channel with the two-fluid model, where the velocity is calculated for each phase, depending on the liquid saturation (Chapter II-4.8). For example, Fig. IV-12 shows the value of the reciprocal velocity ratio in the cathode channels obtained with the two-fluid model for the Setpoint No. 1 conditions. The velocity ratio is lower than 1000 over the major part of the surface, and drops to 450 close to the air outlet, where the amount of liquid water is maximum. A higher ratio favors the evacuation of liquid water, which is consistent with the lower saturation obtained at the cathode with the two-fluid model. Finally, it has to be noticed that its order of magnitude is similar for both models (fixed to  $\sim 1000$  and from 450 to 2000 for the one-fluid and two-fluid models, respectively).

To conclude, the two-fluid model is able to predict the liquid water distribution at the cell scale for a large surface area in high power automotive conditions compared to the one-fluid model.

TWO-FLUID MODEL

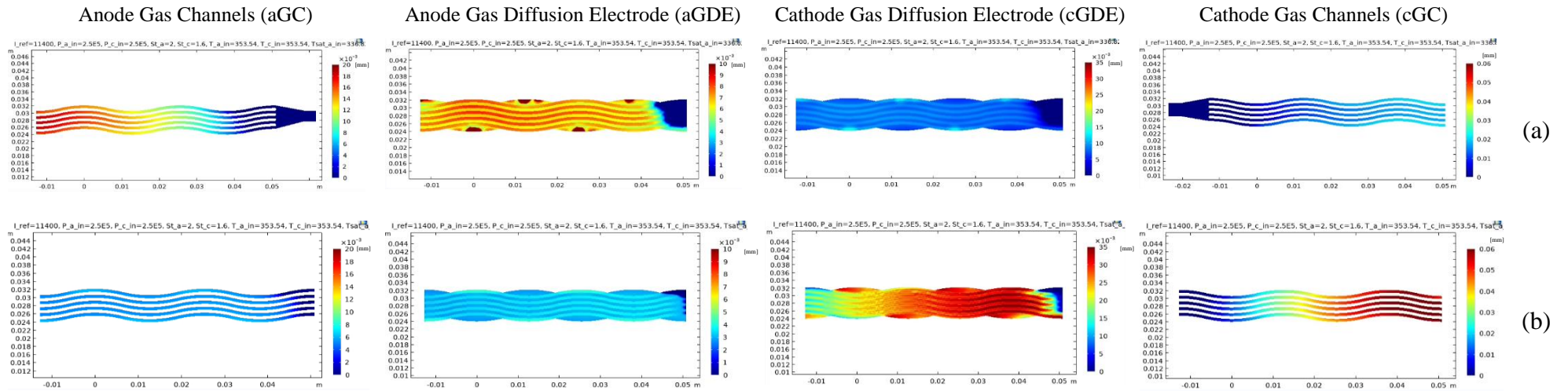


Fig. IV-10. Liquid water thickness in different layers for Setpoint No. 1 conditions (Table IV-3) from the: (a) two-fluid and (b) one-fluid models.

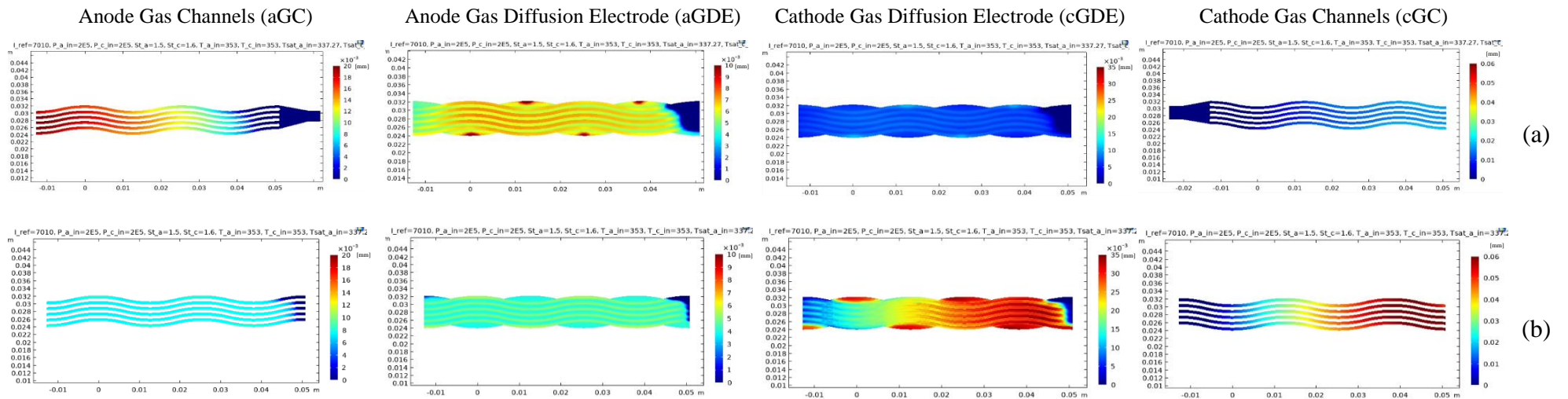


Fig. IV-11. Liquid water thickness in different layers for Setpoint No. 2 conditions (Table IV-3) from the: (a) two-fluid and (b) one-fluid models.

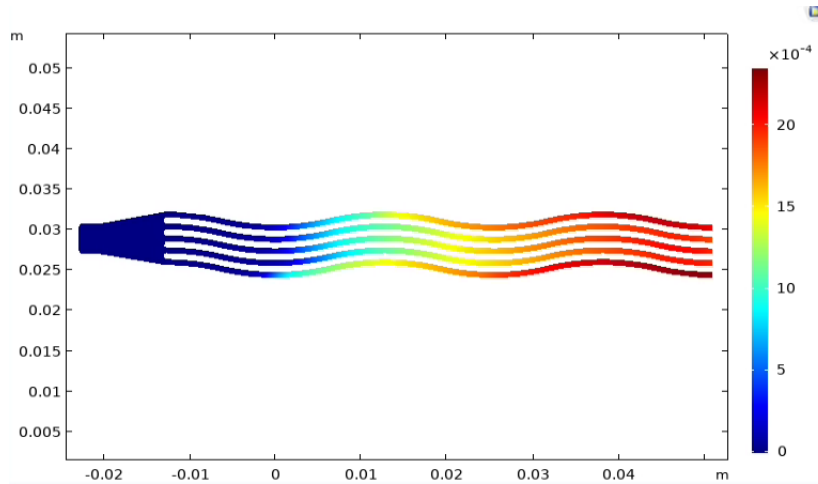


Fig. IV-12. Reciprocal of the gas and liquid velocity ratio obtained with the two-fluid model for the Setpoint No. 1 conditions (Table IV-3).

### 5.3 Water Distribution over the Cell Surface in Each Layer

According to the good agreement between the two-fluid model and the experimental tests, the water distribution over the cell surface in each layer is analyzed for different operating conditions. Namely, Fig. IV-13 and Fig. IV-14 show the liquid water thickness (a) and the saturation (b). On the entire stack, liquid water accumulates at the anode outlet (cathode inlet) while the anode inlet (cathode outlet) is dried whatever the operating condition. The progressive increase of the water at the anode gas channel is due to the back diffusion of water from the cathode side. Furthermore, the hydrogen consumption by its oxidation (HOR) induce an increase of the water vapor fraction. When the vapor saturates, liquid water appears, which is hard to evacuate by the hydrogen flow, due to its low density.

At the cathode side, the same trend is observed in the gas channel with a water accumulation from the inlet to the outlet. However, the liquid water distribution in each GDE is not always similar to the distribution of the corresponding channel. Indeed, the water distribution in both anode and cathode GDEs are very close together with a drier zone at the air outlet (hydrogen inlet). The distribution of liquid water in the cathode GDE is significantly different from the cathode channel with a humid zone at the air inlet. According to the current density distribution (Fig. IV-15), the water accumulation at the air inlet can be related to the high current density while the drier zone observed at the air outlet is due to the lower current density.

The local liquid water accumulations at the anode GDE on the edges (dark red zone in Fig. IV-13), inducing higher local current density, and higher liquid water saturation in the external cathode channels, are again due to no proper water convection by hydrogen gas (no anode channel in front of these zones). The phenomenon is amplified close to the hydrogen outlet. Conversely, no liquid water accumulation is observed at the cathode GDE on the edges (blue zone in Fig. IV-15) due to the very low current densities in these later zones.

For the Setpoint No. 2, the same trends are observed. Nonetheless, liquid water accumulation is lower at the anode GDE on the edges due to a lower water production (i.e. lower current density) in the zones that are not in front of anode channels.

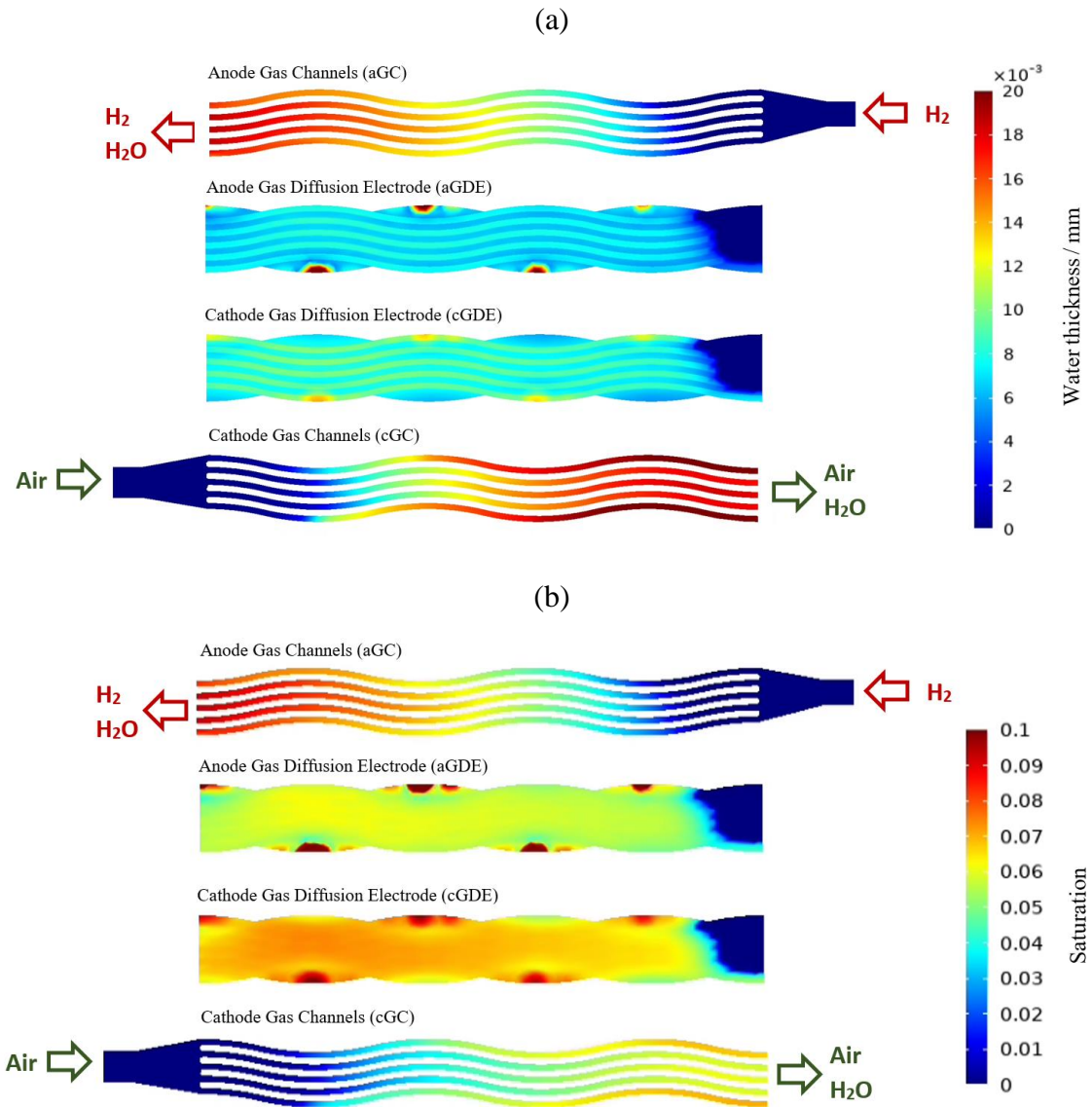


Fig. IV-13. (a) Water thickness and (b) saturation distribution in the anode and cathode gas channels and gas diffusion electrode, in the Setpoint No. 1 operating conditions (Table IV-3).

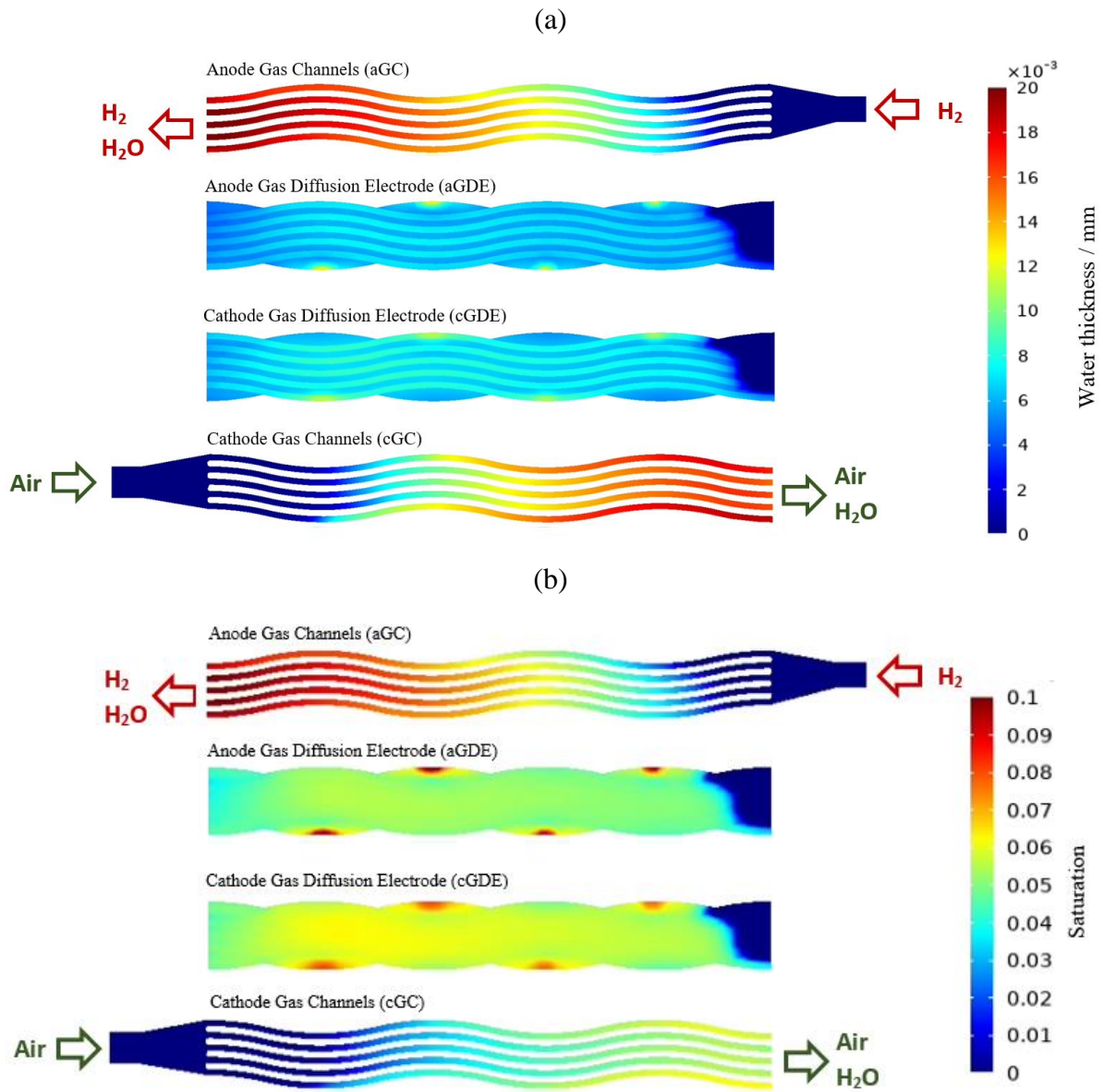


Fig. IV-14. (a) Water thickness and (b) saturation distribution in the anode and cathode gas channels and gas diffusion electrode, in the Setpoint No. 2 operating conditions (Table IV-3).

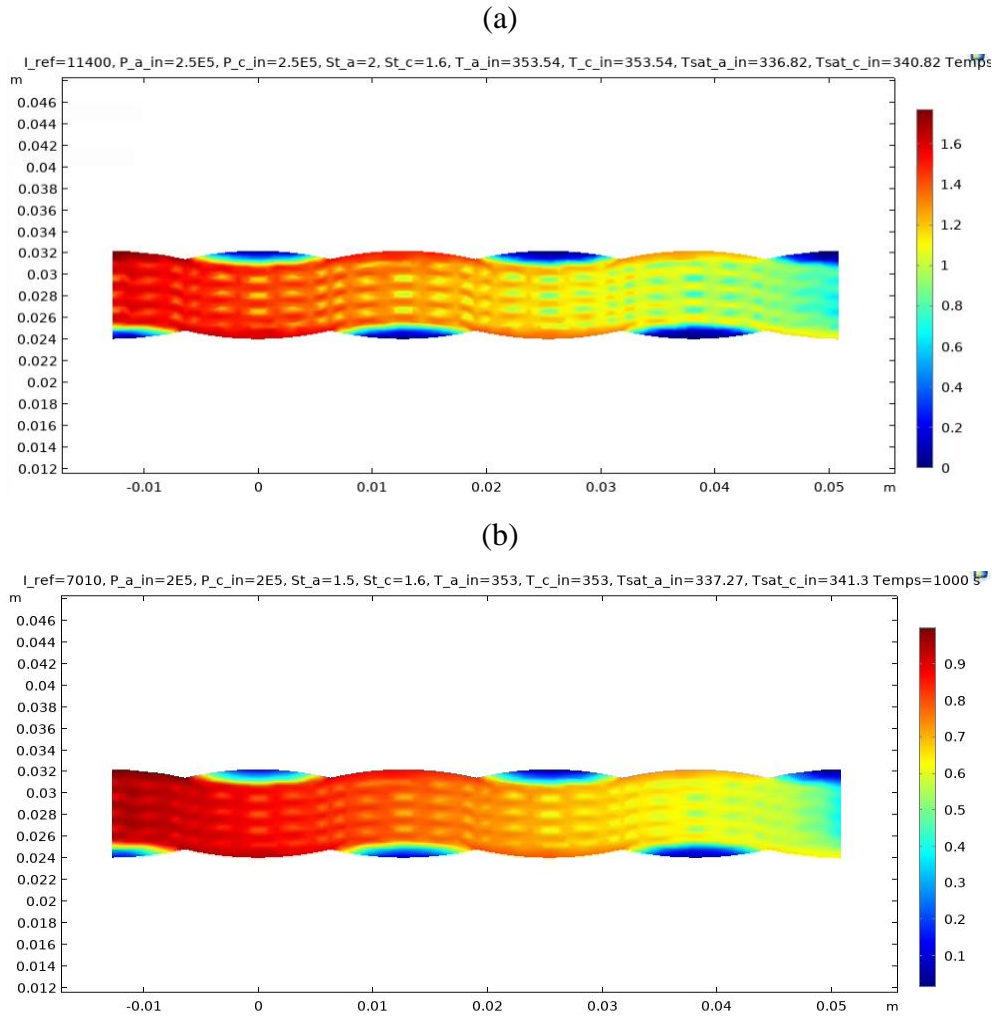


Fig. IV-15. Current density distribution for: (a) Setpoint No. 1 and (b) Setpoint No. 2 conditions (Table IV-3).

## Conclusion

In this chapter, the macroscopic equations of a two-phase flow described in Chapter II have been implemented under their pseudo-3D formulation in the COMSOL Multiphysics® software. This two-fluid model has been compared to liquid water measurements by neutron imaging carried out on a new fuel cell geometry under high power operating conditions. The new design made up of undulating parallel gas channels lead to reduce the temperature heterogeneities in comparison with the F-geometry presented in Chapter III. Therefore, the two-fluid model was validated on a reduced geometry representative of the entire cell while saving computing time. It is then compared to the one-fluid model on the same geometry. It appears that the numerical results of the one-fluid model greatly overestimate the quantity of liquid water and cannot correctly represent its distribution unlike the two-fluid model. In addition, the two-

fluid model can clearly identify high water concentration areas in each layer. It appears that the liquid water is not well evacuated at the anode side due to a low density gas. Furthermore, the air outlet (hydrogen inlet) is dry in the GDEs as well as in the anode gas channels, which can be explained by the low humidification of the inlet hydrogen and the lower current density in this zone. Finally, the saturation-dependent velocity ratio calculated by the two-fluid model can better describe the complex two-phase flow.

## General Conclusion

This manuscript is dedicated to the investigation of liquid water heterogeneities in large area PEM fuel cells using a two-phase flow multiphysics model. Up to date, the water and temperature management remains one of the major challenges in optimizing the performance and increasing the durability of a PEM fuel cell for a large scale commercialization. A state of the art highlights that only few two-phase flow models have been proposed in order to simulate the liquid water distribution in the different layers and at the different length scales.

In this work, the conservation equations were described for one-phase and two-phase flow from the local and instantaneous equations. The macroscopic equations are then obtained by the local volume-average method over the Representative Elementary Volume (REV) describing a porous medium at the meso-scale. The averaged equations are complex with many interfacial terms representing notably the phase transfer. Namely, it is very difficult to find realistic closure laws to model phase change, which can cause numerical issues.

Two PEM fuel cell models were developed for one-phase and two-phase flow by coupling an electrochemical model to the fluid thermodynamics. In this thesis, many efforts are dedicated to the modeling of a two-phase flow in a PEMFC. They were implemented in a simulation software, COMSOL Multiphysics®, using the Finite Element Method (FEM). First, a one-fluid model developed previously has been improved and used to analyze neutron imaging results at different scales, showing good results, but also some limitations for high power operating conditions. Then, a two-fluid model has been developed, either for 1D or pseudo-3D geometries. It finally led to first simulation results representing liquid water accumulation in cells with a satisfying accuracy compared to neutron imaging data. However, the two-fluid model still needs further improvement to increase its robustness. Indeed, many numerical problems have been encountered, especially for critical conditions. When significant liquid water accumulations (saturation close to the unity) are simulated in the porous media (flooding or pre-flooding), the model is no longer valid.

All the numerical results were compared to liquid water measurements by neutron imaging tests. The one-fluid model accurately locates and quantifies the liquid water in the F-geometry cell at low power operating in an automotive application while representing the real flow-field design. It appears that the distribution of water and temperature is highly heterogeneous due to

a non-optimal cooling circuit. Further, a sensitivity analysis showed significant variations of the liquid water quantity according to different electro-osmotic drag and diffusion coefficients without changing the general trend distribution.

The two-fluid model was used to simulate higher power automotive application for which the one-fluid model was reaching some limits. This model was implemented on a new bipolar plate design considering undulating parallel channels. It is validated for two conditions in this work by correctly reflecting the distribution of the liquid water on a large area cell. Other operating conditions at low and high power have to be simulated in order to know the two-fluid model validity range and to better understand the physical phenomena. Moreover, a sensitivity analysis of key parameters, such as the hydrophobicity of the porous materials and the relative permeability coefficient, should be done. Indeed, both parameters mentioned, which are still widely discussed in the literature, intervene in the (empirical) modeling of some transport mechanisms of the liquid water. They have a significant impact on the simulated distribution and quantity of the liquid water in PEM fuel cells. In addition, the fluid dynamics coupled to the electrochemical model could be solved again from a computed temperatures step to investigate the impact of the thermal transfer on water distribution. Furthermore, the Darcy-Forchheimer law or a complete momentum equation could be implemented instead of a Darcy law to take into account not only the viscous stress but also the convective transport in the gas channels. Eventually, it can be interesting to couple this two-fluid model at the cell scale with a finer model (e.g. Pore Network Model, Lattice-Boltzmann Model) describing more precisely the liquid water flow in the porous media.

Finally, this two-fluid model is able to forecast, in each component, dried and flooded zones in a large surface area PEMFC. Accordingly, it can be used to better observe and understand operating heterogeneities and their impact on both cell performance and durability especially for cell flooding circumstances. Thereby, innovative bipolar plates design can be modeled and simulated to better manage the water. Moreover, industrial manufacturers have a growing interest in increasing the fuel cell temperature in order to reduce the external heat exchanger for an automotive application. Such systems requirement (e.g.  $> 95^{\circ}\text{C}$ ) can be simulated with the two-fluid model.

## References

- [1] Wang, S. and Ge, M. (2019). *Everything You Need to Know About the Fastest-Growing Source of Global Emissions: Transport*. World Resources Institute. <https://www.wri.org/insights/everything-you-need-know-about-fastest-growing-source-global-emissions-transport>.
- [2] *Fossil Fuel Subsidies Database*. International Energy Agency. [Updated June 2021]. <https://www.iea.org/data-and-statistics/data-products>.
- [3] (2019). *Agir en cohérence avec les ambitions*. Haut Conseil pour le Climat. [https://www.hautconseilclimat.fr/wp-content/uploads/2019/09/hcc\\_rapport\\_annuel\\_grand\\_public\\_2019.pdf](https://www.hautconseilclimat.fr/wp-content/uploads/2019/09/hcc_rapport_annuel_grand_public_2019.pdf).
- [4] (2021). *European Green Deal: Commission proposes transformation of EU economy and society to meet climate ambitions*. European Commission [https://ec.europa.eu/commission/presscorner/detail/fr/IP\\_21\\_3541](https://ec.europa.eu/commission/presscorner/detail/fr/IP_21_3541).
- [5] Henning Lohse-Busch, Kevin Stutenberg, Michael Duoba, Xinyu Liu, Amgad Elgowainy, Michael Wang, Thomas Wallner, Brad Richard, Martha Christenson, Automotive fuel cell stack and system efficiency and fuel consumption based on vehicle testing on a chassis dynamometer at minus 18 °C to positive 35 °C temperatures, *International Journal of Hydrogen Energy*, Volume 45, Issue 1, 2020, Pages 861-872, ISSN 0360-3199, <https://doi.org/10.1016/j.ijhydene.2019.10.150>.
- [6] Sauvant-Moynot, V., Orsini, F., Juton, A. (2020). *État de l'art et perspectives des batteries de voitures électriques*. Éduscol. <https://eduscol.education.fr/sti/sites/eduscol.education.fr/sti/files/resources/pedagogiques/12098/12098-etat-de-lart-et-perspectives-des-batteries-de-ve-ensps.pdf>.
- [7] Van De Kaa, G.; Scholten, D.; Rezaei, J.; Milchram, C. The Battle between Battery and Fuel Cell Powered Electric Vehicles: A BMW Approach. *Energies* 2017, 10, 1707, <https://doi.org/10.3390/en10111707>.
- [8] Bethoux, O. Hydrogen Fuel Cell Road Vehicles: State of the Art and Perspectives. *Energies* 2020, 13, 5843. <https://doi.org/10.3390/en13215843>.
- [9] (2021). *Chiffres de vente & immatriculations de voitures électriques en France*. Automobile Propre. <https://www.automobile-propre.com/dossiers/chiffres-vente-immatriculations-france/>.
- [10] (2021). *Toyota Mirai breaks world record for distance driven with one fill of hydrogen*. Toyota Europe Newsroom. <https://newsroom.toyota.eu/toyota-mirai-breaks-world-record-for-distance-driven-with-one-fill-of-hydrogen/>.
- [11] Moretti, I., Webber, M. E. (2021). *Natural hydrogen : a geological curiosity or the primary energy source for a low carbon future ?* Renewable matter. <https://www.renewablematter.eu/articles/article/natural-hydrogen-a-geological-curiosity-or-the-primary-energy-source-for-a-low-carbon-future>.
- [12] Alain Prinzhofer, Cheick Sidy Tahara Cissé, Aliou Boubacar Diallo, Discovery of a large accumulation of natural hydrogen in Bourakebougou (Mali), *International Journal of Hydrogen Energy*, Volume 43, Issue 42, 2018, Pages 19315-19326, ISSN 0360-3199, <https://doi.org/10.1016/j.ijhydene.2018.08.193>.
- [13] Truche, Laurent & Bazarkina, Elena. (2019). Natural hydrogen the fuel of the 21 st century. E3S Web of Conferences. 98. 10.1051/e3sconf/20199803006.
- [14] Kane, M. (2020). *Battery Electric Vs Hydrogen Fuel Cell: Efficiency Comparison*. InsideEVs. <https://insideevs.com/news/406676/battery-electric-hydrogen-fuel-cell-efficiency-comparison/>.
- [15] (September, 2021). *Cours du platine par kilo EUR*. BullionByPost. <https://www.bullionbypost.fr/cours-platine/cours-du-platine-par-kilo/>.
- [16] Ganesan, A., Narayanasamy, M. Ultra-low loading of platinum in proton exchange membrane-based fuel cells: a brief review. *Mater Renew Sustain Energy* 8, 18 (2019). <https://doi.org/10.1007/s40243-019-0156-x>.

- [17] Aeree Seo, Jaeseung Lee, Kookil Han, Hasuck Kim, Performance and stability of Pt-based ternary alloy catalysts for PEMFC, *Electrochimica Acta*, Volume 52, Issue 4, 2006, Pages 1603-1611, ISSN 0013-4686, <https://doi.org/10.1016/j.electacta.2006.03.097>.
- [18] Chandran, P., Ghosh, A. & Ramaprabhu, S. High-performance Platinum-free oxygen reduction reaction and hydrogen oxidation reaction catalyst in polymer electrolyte membrane fuel cell. *Sci Rep* 8, 3591 (2018). <https://doi.org/10.1038/s41598-018-22001-9>.
- [19] Mathias MF, Roth J, Fleming J, Lehnert W. Diffusion Media Materials and Characterization. In: Vielstich W, Lamm A, Gastegier HA, editors. *Handbook of Fuel Cells, Fundamentals, Technology and Applications. Fuel Cell Technology and Applications*, vol. 3. New York: John Wiley & Sons; 2003. p. 517–37.
- [20] Tao Chen, Shihua Liu, Jiwei Zhang, Mengnan Tang, Study on the characteristics of GDL with different PTFE content and its effect on the performance of PEMFC, *International Journal of Heat and Mass Transfer*, Volume 128, 2019, Pages 1168-1174, ISSN 0017-9310, <https://doi.org/10.1016/j.ijheatmasstransfer.2018.09.097>.
- [21] Jin Hyun Nam, Kyu-Jin Lee, Gi-Suk Hwang, Charn-Jung Kim, Massoud Kaviani, Microporous layer for water morphology control in PEMFC, *International Journal of Heat and Mass Transfer*, Volume 52, Issues 11–12, 2009, Pages 2779-2791, ISSN 0017-9310, <https://doi.org/10.1016/j.ijheatmasstransfer.2009.01.002>.
- [22] Nanadegani, FS, Lay, EN, Sunden, B. Effects of an MPL on water and thermal management in a PEMFC. *Int J Energy Res.* 2019; 43: 274– 296. <https://doi.org/10.1002/er.4262>.
- [23] Barbir F. *PEM fuel cells: theory and practice*. New York: Academic Press; 2012.
- [24] Andersen, Shuang & Chen, Qian & Joergensen, Fleming & Stein, Paul & Skou, Eivind. (2007). F-19 NMR studies of Nafion (TM) ionomer adsorption on PEMFC catalysts and supporting carbons. *Solid State Ionics*. 178. 1568-1575. 10.1016/j.ssi.2007.10.007.
- [25] A. Arvay, J. French, J.-C. Wang, X.-H. Peng, A.M. Kannan, Nature inspired flow field designs for proton exchange membrane fuel cell, *International Journal of Hydrogen Energy*, Volume 38, Issue 9, 2013, Pages 3717-3726, ISSN 0360-3199, <https://doi.org/10.1016/j.ijhydene.2012.12.149>.
- [26] Yuan, Xiao-Zi & Wang, Haijiang & Zhang, Jiujun & Wilkinson, David. (2005). Bipolar plates for PEM fuel cells - From materials to processing. *Journal of New Materials for Electrochemical Systems*. 8. 257-267.
- [27] Yuxi Song, Caizhi Zhang, Chun-Yu Ling, Ming Han, Rui-Yuan Yong, Deen Sun, Jinrui Chen, Review on current research of materials, fabrication and application for bipolar plate in proton exchange membrane fuel cell, *International Journal of Hydrogen Energy*, Volume 45, Issue 54, 2020, Pages 29832-29847, ISSN 0360-3199, <https://doi.org/10.1016/j.ijhydene.2019.07.231>.
- [28] Baroutaji, Ahmad & Carton, James & Sajjia, Mustafa & Olabi, Abdul Ghani. (2015). Materials in PEM Fuel Cells. 10.1016/B978-0-12-803581-8.04006-6.
- [29] Brevet EP3624241, Method of manufacturing an electrochemical reactor flow guide, J. Salomon, B. Amestoy, J.-F. Blachot, D. Tremblay (2018).
- [30] Migliardini, F. & Capasso, Clemente & Corbo, P.. (2014). Optimization of hydrogen feeding procedure in PEM fuel cell systems for transportation. *International Journal of Hydrogen Energy*. 39. 10.1016/j.ijhydene.2014.08.070
- [31] F. Migliardini, T.M. Di Palma, M.F. Gaele, P. Corbo, Hydrogen purge and reactant feeding strategies in self-humidified PEM fuel cell systems, *International Journal of Hydrogen Energy*, Volume 42, Issue 3, 2017, Pages 1758-1765, ISSN 0360-3199, <https://doi.org/10.1016/j.ijhydene.2016.06.196>.
- [32] N. Marx, D. Hissel, F. Gustin, L. Boulon and K. Agbossou, "On Maximizing the Steady-State Efficiency of a Multi-Stack Fuel Cell System," 2018 IEEE Vehicle Power and Propulsion Conference (VPPC), 2018, pp. 1-6, doi: 10.1109/VPPC.2018.8605036.

- [33] Neigel Marx, Daniel Hissel, Frédéric Gustin, Loïc Boulon, Kodjo Agbossou, On the sizing and energy management of an hybrid multistack fuel cell – Battery system for automotive applications, *International Journal of Hydrogen Energy*, Volume 42, Issue 2, 2017, Pages 1518-1526, ISSN 0360-3199, <https://doi.org/10.1016/j.ijhydene.2016.06.111>.
- [34] Marx, N.; Cárdenas, D.C.T.; Boulon, L.; Gustin, F.; Hissel, D. Degraded mode operation of multi-stack fuel cell systems. *IET Electr. Syst. Transp.* 2016, 6, 3–11, <https://doi.org/10.1049/iet-est.2015.0012>.
- [35] Bernardinis, A.; Frappé, E.; Béthoux, O.; Marchand, C.; Coquery, G. Multi-port Power Converter for Segmented PEM Fuel Cell in Transport Application. Simulation with fault tolerant strategy. *Eur. Phys. J. Appl. Phys.* 2012, 58, 1–15, <https://doi.org/10.1051/epjap/2012120056>.
- [36] S. Rodosik, J.-P. Poirot-Crouvezier, Y. Bultel, “Simplified anode architecture for PEMFC systems based on alter-native fuel feeding: Experimental characterization and optimization for automotive applications”, *International Journal of Hydrogen Energy*, vol. 45, no. 38, pp. 19720-19732, July 2020.
- [37] Nandjou, F., (2015), *Etude locale de la thermique dans les piles à combustibles pour application automobile. Corrélation à la durée de vie*, [PhD dissertation, University of Grenoble Alpes, Grenoble].
- [38] *How Do Fuel Cell Electric Vehicles Work Using Hydrogen?* U.S. Department of Energy. <https://afdc.energy.gov/vehicles/how-do-fuel-cell-electric-cars-work>.
- [39] Torregrossa, M., (2021). Voiture hydrogène : quelles ventes en Europe en 2020 ? <https://www.h2-mobile.fr/actus/voitures-hydrogene-ventes-europe-2020/>.
- [40] U.S. DRIVE, (2017). *Fuel Cell Technical Team Roadmap*. Department of Energy [https://www.energy.gov/sites/prod/files/2017/11/f46/FCTT\\_Roadmap\\_Nov\\_2017\\_FINAL.pdf](https://www.energy.gov/sites/prod/files/2017/11/f46/FCTT_Roadmap_Nov_2017_FINAL.pdf).
- [41] T.E. Springer, T.A. Zawodzinski, S. Gottesfeld, Polymer electrolyte fuel cell model, *J. Electrochem. Soc.* 138 (8) (1991) 2334–2342.
- [42] S. Hwang, P. Lee, S. Jo, C. Cha, S. Hong, S. Han, J. Ko, Transient behavior of proton exchange membrane fuel cell under non-isothermal condition, *Renew. Energy* 42 (2012) 54–59.
- [43] F. Meier, G. Eigenberger, Transport parameters for the modelling of water transport in ionomer membranes for PEM-fuel cells, *Electrochim. Acta* 49 (2004) 1731–1742.
- [44] T. Zawodzinski, J. Dawy, J. Valerio, S. Gottesfeld, The water content dependence of electroosmotic drag in proton-conducting polymer electrolytes, *Electrochim. Acta* 40 (1994) 297–302.
- [45] Peng, Z.; Morin, A.; Hugué, P.; Schott, P.; Pauchet, J. In-situ measurement of electroosmotic drag coefficient in Nafion membrane for the PEMFC. *J. Phys. Chem. B* 2011, 115, 12835–12844, <https://doi.org/10.1021/jp205291f>.
- [46] Feina Xu, Sébastien Leclerc, Didier Stemmelen, Jean-Christophe Perrin, Alain Retournard, Daniel Canet, Study of electro-osmotic drag coefficients in Nafion membrane in acid, sodium and potassium forms by electrophoresis NMR, *Journal of Membrane Science*, Volume 536, 2017, Pages 116-122, ISSN 0376-7388, <https://doi.org/10.1016/j.memsci.2017.04.067>.
- [47] Schroeder, P. (1903). Über Erstarrungs- und Quellungserscheinungen von Gelatine. *Zeitschrift für Physikalische Chemie*, 45U(1), 75-117, <https://doi.org/10.1515/zpch-1903-4503>.
- [48] Fuller, Solid-polymer electrolyte fuel cells, PhD Dissertation, University of California, 1992.
- [49] T. Zawodzinski, M. Neeman, L. Sillerud, S. Gottesfeld, Determination of water diffusion coefficient in perfluorosulfonate ionomeric membranes, *J. Phys. Chem.* 95 (1991) 6040–6044.
- [50] S. Motupally, A. Becker, J.W. Weidner, Diffusion of water in Nafion 115 membranes, *J. Electrochem. Soc.* 147 (9) (2000) 3171–3177.
- [51] Kaviany, M., *Principles of Heat Transfer in Porous Media*, 2nd edn. Springer, New York, 1995.
- [52] Jin Hyun Nam, Massoud Kaviany, Effective diffusivity and water-saturation distribution in single- and two-layer PEMFC diffusion medium, *International Journal of Heat and Mass Transfer*, Volume

- 46, Issue 24, 2003, Pages 4595-4611, ISSN 0017-9310, [https://doi.org/10.1016/S0017-9310\(03\)00305-3](https://doi.org/10.1016/S0017-9310(03)00305-3).
- [53] Leverett, M.C.. "Capillary Behavior in Porous Solids." *Trans.* 142 (1941): 152–169. doi: <https://doi.org/10.2118/941152-G>.
- [54] Pasaogullari, Ugur & Wang, Chao-Yang & Chen, Ken. (2004). Liquid Water Transport in Polymer Electrolyte Fuel Cells With Multi-Layer Diffusion Media. American Society of Mechanical Engineers, Heat Transfer Division, (Publication) HTD. 375. 10.1115/IMECE2004-59283.
- [55] Raphaël Di Chiara Roupert, Développement d'un code de calcul multiphasique multiconstituants, dirigé par Gerhard Schäfer et Michel Quintard, 2009, Thèse de doctorat Mécanique des Fluides, Université de Strasbourg, <https://www.theses.fr/2009STRA6240>.
- [56] Gallagher, Kevin & Darling, Robert & Patterson, Timothy & Perry, Mike. (2008). Capillary Pressure Saturation Relations for PEM Fuel Cell Gas Diffusion Layers. *Journal of The Electrochemical Society - J ELECTROCHEM SOC.* 155. 10.1149/1.2979145.
- [57] Sole, JD, & Ellis, MW. "Determination of the Relationship Between Capillary Pressure and Saturation in PEMFC Gas Diffusion Media." *Proceedings of the ASME 2008 6th International Conference on Fuel Cell Science, Engineering and Technology. ASME 2008 6th International Conference on Fuel Cell Science, Engineering and Technology.* Denver, Colorado, USA. June 16–18, 2008. pp. 829-840. ASME. <https://doi.org/10.1115/FuelCell2008-65253>.
- [58] Jacob M. LaManna, James V. Bothe, Feng Yuan Zhang, Matthew M. Mench, Measurement of capillary pressure in fuel cell diffusion media, micro-porous layers, catalyst layers, and interfaces, *Journal of Power Sources*, Volume 271, 2014, Pages 180-186, ISSN 0378-7753, <https://doi.org/10.1016/j.jpowsour.2014.07.163>.
- [59] Ceballos, Loïc, Caractérisation des propriétés fluidiques des couches de diffusion des piles à combustible PEMFC par une approche numérique de type réseaux de pores et par une analyse d'images issues de la tomographie X, dirigé par Prat, Marc, 2011, Thèse de doctorat Energétique et Transferts Toulouse, INPT 2011, 2011INPT0001, <http://www.theses.fr/2011INPT0001/document>.
- [60] Zhang FY, Yang XG, Wang CY. Liquid water removal from a polymer electrolyte fuel cell. *J Electrochem Soc* 2006;153(2):A225–32, DOI: 10.1149/1.2138675.
- [61] Hussaini, I.S.; Wang, C.Y. Visualization and quantification of cathode channel flooding in PEM fuel cells. *J. Power Sources* 2009, 187, 444-451.
- [62] Pierre Carrere, Marc Prat. Liquid water in cathode gas diffusion layers of PEM fuel cells: Identification of various pore filling regimes from pore network simulations. *International Journal of Heat and Mass Transfer*, Elsevier, 2019, 129, pp.1043-1056. ff10.1016/j.ijheatmasstransfer.2018.10.004ff. ffhal02352160f.
- [63] Chen, Li & Luan, Hui-Bao & Tao, Wen-Quan. (2010). Liquid water dynamic behaviors in the GDL and GC of PEMFCS using Lattice Boltzmann method. *Frontiers in Heat and Mass Transfer*. 1. 10.5098/hmt.v1.2.3002.
- [64] Mengbo, Ji & Wei, Z.. (2009). A Review of Water Management in Polymer Electrolyte Membrane Fuel Cells. *Energies*. 2. DOI: [10.3390/en20401057](https://doi.org/10.3390/en20401057).
- [65] Wolfgang Schmittinger, Ardalan Vahidi, A review of the main parameters influencing long-term performance and durability of PEM fuel cells, *Journal of Power Sources*, Volume 180, Issue 1, 2008, Pages 1-14, ISSN 0378-7753, <https://doi.org/10.1016/j.jpowsour.2008.01.070>.
- [66] Trung V. Nguyen and Ralph E. White 1993 *J. Electrochem. Soc.* 140 2178, <http://dx.doi.org/10.1149/1.2220792>.
- [67] Sone, Y.; Ekdunge, P.; Simonsson, D. Proton conductivity of Nafion 117 as measured by a four-electrode AC impedance method. *J. Electrochem. Soc.* 1996, 143, 1254-1259.
- [68] Stumper, J.; Löhr, M.; Hamada, S. Diagnostic tools for liquid water in PEM fuel cell. *J. Power Sources* 2005, 143, 150-157.

- [69] B. Andreaus, A.J. McEvoy, G.G. Scherer, Analysis of performance losses in polymer electrolyte fuel cells at high current densities by impedance spectroscopy, *Electrochimica Acta*, Volume 47, Issues 13–14, 2002, Pages 2223–2229, ISSN 0013-4686, [https://doi.org/10.1016/S0013-4686\(02\)00059-2](https://doi.org/10.1016/S0013-4686(02)00059-2).
- [70] Felix N. Büchi and Supramaniam Srinivasan 1997 *J. Electrochem. Soc.* 144 2767.
- [71] F. Nandjou, J.-P. Poirot-Crouvezier, M. Chandesris, J.-F. Blachot, C. Bonnaud, Y. Bultel, Impact of heat and water management on proton exchange membrane fuel cells degradation in automotive application, *Journal of Power Sources*, Volume 326, 2016, Pages 182–192, ISSN 0378-7753, <https://doi.org/10.1016/j.jpowsour.2016.07.004>.
- [72] Li, H.; Tang, Y.; Wang, Z.; Shi, Z.; Wu, S.; Song, D.; Zhang, J.; Fatih, K.; Zhang, J.; Wang, H.; et al. A review of water flooding issues in the proton exchange membrane fuel cell. *J. Power Sources* 2008, 178, 103–117, <https://doi.org/10.1016/j.jpowsour.2007.12.068>.
- [73] Taniguchi, A.; Akita, T.; Yasuda, K.; Miyazaki, Y. Analysis of degradation in PEMFC caused by cell reversal during air starvation. *Int. J. Hydrogen Energy* 2008, 33, 2323–2329. <https://doi.org/10.1016/j.ijhydene.2008.02.049>.
- [74] Liu, Z.; Yang, L.; Mao, Z.; Zhuge, W.; Zhang, Y.; Wang, L. Behavior of PEMFC in starvation. *J. Power Sources* 2006, 157, 166–176, <https://doi.org/10.1016/j.jpowsour.2005.08.006>.
- [75] Borup, R.; Meyers, J.; Pivovar, B. Scientific Aspects of Polymer Electrolyte Fuel Cell Durability and Degradation. *Chem. Rev.* 2007, 107, 2904–3952, <https://doi.org/10.1021/cr050182l>.
- [76] Schulze, M.; Wagner, N.; Kaz, T.; Friedrich, K. Combined electrochemical and surface analysis investigation of degradation processes in polymer electrolyte membrane fuel cells. *Electrochim. Acta* 2007, 52, 2328–2336, <https://doi.org/10.1016/j.electacta.2006.05.063>.
- [77] Jens Eller, Tomas Rosén, Federica Marone, Marco Stampanoni, Alexander Wokaun, Felix Büchi, Progress in in situ X-ray tomographic microscopy of liquid water in gas diffusion layers of PEFC, *J. Electrochem. Soc.* 158 (2011) B963–B970, <https://doi.org/10.1149/1.3596556>.
- [78] Bernardi DM, Verbrugge MW. Mathematical Model of a Gas Diffusion Electrode Bonded to a Polymer Electrolyte. *AIChE Journal* 1991;Vol. 37(No. 8).
- [79] C. Siegel, Review of computational heat and mass transfer modeling in polymer-electrolyte-membrane (PEM) fuel cells, *Energy* 33 (2008) 1331–1352, <https://doi.org/10.1016/j.energy.2008.04.015>.
- [80] N. Djilali, Computational modelling of polymer electrolyte membrane (PEM) fuel cells: challenges and opportunities, *Energy* 32 (2007), <https://doi.org/10.1016/j.energy.2006.08.007>.
- [81] A.Z. Weber, R.L. Borup, R.M. Darling, P.K. Das, T.J. Dursch, W. Gu, et al., A critical review of modeling transport phenomena in polymer-electrolyte fuel cells, *J. Electrochem. Soc.* 161 (2014) F1254–F1299, <https://doi.org/10.1149/2.0751412jes>.
- [82] M. Secanell, J. Wishart, P. Dobson, Computational design and optimization of fuel cells and fuel cell systems: a review, *J. Power Sources* 196 (2011) 3690–3704, <https://doi.org/10.1016/j.jpowsour.2010.12.011>.
- [83] C. Fink, N. Fouquet, Three-dimensional simulation of polymer electrolyte membrane fuel cells with experimental validation, *Electrochim. Acta* 56 (28) (2011) 10820–10831, <https://doi.org/10.1016/j.electacta.2011.05.041>.
- [84] J.-P. Kone, X. Zhang, Y. Yan, G. Hu, G. Ahmadi, Three-dimensional multiphase flow computational fluid dynamics models for proton exchange membrane fuel cell: a theoretical development, *J. Comput. Multiphase Flows* 9 (1) (2017) 3–25, <https://doi.org/10.1177/1757482X17692341>.
- [85] C.Y. Wang, Ping Cheng, A multiphase mixture model for multiphase, multicomponent transport in capillary porous media—I. Model development, *Int. J. Heat Mass Transf.* 39 (1996) 3607–3618, [https://doi.org/10.1016/0017-9310\(96\)00036-1](https://doi.org/10.1016/0017-9310(96)00036-1).
- [86] Weilin Zhuge, Yangjun Zhang, Pingwen Ming, Xingsheng Lao, Xiao Chen, Numerical simulation of three-dimensional gas/liquid two-phase flow in a proton exchange membrane fuel cell, *Front.*

- Energy Power Eng. Chin. 1 (2007), <https://doi.org/10.1007/s11708-007-0044-4>.
- [87] C. Siegel. Two-Dimensional, Non-Isothermal, Two-Phase Flow inside the Gas Diffusion Layer Unit of the Polymer-Electrolyte-Membrane Fuel Cell, in: Proceedings of the COMSOL User Conference - Frankfurt, 2006.
- [88] Z.H. Wang, C.Y. Wang, K.S. Chen, Two-phase flow and transport in the air cathode of proton exchange membrane fuel cells, *J. Power Sources* 94 (1) (2001) 40–50, [https://doi.org/10.1016/S0378-7753\(00\)00662-5](https://doi.org/10.1016/S0378-7753(00)00662-5).
- [89] Wensheng He, Jung Yi, Trung Nguyen, Two-phase flow model of the cathode of PEM fuel cells using interdigitated flow fields, *AIChE J.* 46 (2000) 2053–2064, <https://doi.org/10.1002/aic.690461016>.
- [90] Yun Wang, Suman Basu, Chao-Yang Wang, Modeling two-phase flow in PEM fuel cell channels, *J. Power Sources* 179 (2008) 603–617, <https://doi.org/10.1016/j.jpowsour.2008.01.047>.
- [91] Suman Basu, Chao-Yang Wang, Ken Chen, Phase change in a polymer electrolyte fuel cell, *J. Electrochem. Soc.* 156 (2009) B748, <https://doi.org/10.1149/1.3115470>.
- [92] Tomasz Bednarek, Georgios Tsotridis, Issues associated with modelling of proton exchange membrane fuel cell by computational fluid dynamics, *J. Power Sources* 343 (2017) 550–563, <https://doi.org/10.1016/j.jpowsour.2017.01.059>.
- [93] M. Andersson, S.B. Beale, M. Espinoza, Z. Wu, W. Lehnert, A review of cell-scale multiphase flow modeling, including water management, in polymer electrolyte fuel cells, *Appl. Energy* 180 (2016) 757–778, <https://doi.org/10.1016/j.apenergy.2016.08.010>.
- [94] Guobin Zhang, Kui Jiao, Multi-phase models for water and thermal management of proton exchange membrane fuel cell: A review, *Journal of Power Sources*, Volume 391, 2018, Pages 120-133, ISSN 0378-7753, <https://doi.org/10.1016/j.jpowsour.2018.04.071>.
- [95] J. N. Reddy, Ph.D. Introduction to the Finite Element Method, Fourth Edition (McGraw-Hill Education: New York, Chicago, San Francisco, Athens, London, Madrid, Mexico City, Milan, New Delhi, Singapore, Sydney, Toronto, 2019, 2006, 1993, 1984). <https://www.accessengineeringlibrary.com/content/book/9781259861901>.
- [96] C.W Hirt, B.D Nichols, Volume of fluid (VOF) method for the dynamics of free boundaries, *Journal of Computational Physics*, Volume 39, Issue 1, 1981, Pages 201-225, ISSN 0021-9991, [https://doi.org/10.1016/0021-9991\(81\)90145-5](https://doi.org/10.1016/0021-9991(81)90145-5).
- [97] W.J. Yang, H.Y. Wang, Y.B. Kim, Channel geometry optimization using a 2D fuel cell model and its verification for a polymer electrolyte membrane fuel cell, *International Journal of Hydrogen Energy*, Volume 39, Issue 17, 2014, Pages 9430-9439, ISSN 0360-3199, <https://doi.org/10.1016/j.ijhydene.2014.03.243>.
- [98] Peng Quan, Biao Zhou, Andrzej Sobiesiak, Zhongsheng Liu, Water behavior in serpentine micro-channel for proton exchange membrane fuel cell cathode, *Journal of Power Sources*, Volume 152, 2005, Pages 131-145, ISSN 0378-7753, <https://doi.org/10.1016/j.jpowsour.2005.02.075>.
- [99] Chen, S., & Doolen, G.D. (1998). LATTICE BOLTZMANN METHOD FOR FLUID FLOWS. *Annual Review of Fluid Mechanics*, 30, 329-364.
- [100] G.R. Molaeimanesh, M.H. Akbari, Impact of PTFE distribution on the removal of liquid water from a PEMFC electrode by lattice Boltzmann method, *International Journal of Hydrogen Energy*, Volume 39, Issue 16, 2014, Pages 8401-8409, ISSN 0360-3199, <https://doi.org/10.1016/j.ijhydene.2014.03.089>.
- [101] Aghighi, M., Gostick, J. Pore network modeling of phase change in PEM fuel cell fibrous cathode. *J Appl Electrochem* 47, 1323–1338 (2017). <https://doi.org/10.1007/s10800-017-1126-6>.
- [102] Sung Hyun Kwon, Haisu Kang, Ji Hye Lee, Sunbo Shim, Jinhee Lee, Dong Sun Lee, Chi Myung Kim, Seung Geol Lee, Investigating the influence of the side-chain pendants of perfluorosulfonic

- acid membranes in a PEMFC by molecular dynamics simulations, *Materials Today Communications*, Volume 21, 2019, 100625, ISSN 2352-4928, <https://doi.org/10.1016/j.mtcomm.2019.100625>.
- [103] Lee, J.M., Han, H., Jin, S., Choi, S.M., Kim, H.J., Seo, M.H. and Kim, W.B. (2019), A Review on Recent Progress in the Aspect of Stability of Oxygen Reduction Electrocatalysts for Proton-Exchange Membrane Fuel Cell: Quantum Mechanics and Experimental Approaches. *Energy Technol.*, 7: 1900312. <https://doi.org/10.1002/ente.201900312>.
- [104] Jaeseon Lee, Issam Mudawar, Two-phase flow in high-heat-flux micro-channel heat sink for refrigeration cooling applications: Part I—pressure drop characteristics, *International Journal of Heat and Mass Transfer*, Volume 48, Issue 5, 2005, Pages 928-940, ISSN 0017-9310, <https://doi.org/10.1016/j.ijheatmasstransfer.2004.09.018>.
- [105] Y. Wang, C.Y. Wang, *J. Electrochem. Soc.* 152 (2005) A445–A453.
- [106] F. Barbir, *PEM Fuel Cells: Theory and Practice*, 2nd Edition, Elsevier Academic Press, 2012.
- [107] S. Whitaker, *Advances in theory of fluid motion in porous media*, *Industrial & Engineering Chemistry* 1969 61 (12), 14-28, DOI: 10.1021/ie50720a004.
- [108] Carbonell R.G., Whitaker S. (1984) *Heat and Mass Transfer in Porous Media*. In: Bear J., Corapcioglu M.Y. (eds) *Fundamentals of Transport Phenomena in Porous Media*. NATO ASI Series (Series E: Applied Sciences), vol 82. Springer, Dordrecht. [https://doi.org/10.1007/978-94-009-6175-3\\_3](https://doi.org/10.1007/978-94-009-6175-3_3).
- [109] William T. Sha, B.T. Chao, S.L. Soo, Porous-media formulation for multiphase flow with heat transfer, *Nuclear Engineering and Design*, Volume 82, Issues 2–3, 1984, Pages 93-106, ISSN 0029-5493, [https://doi.org/10.1016/0029-5493\(84\)90206-1](https://doi.org/10.1016/0029-5493(84)90206-1).
- [110] Faghri, A., & Zhang, Y. (2006). *Transport Phenomena in Multiphase Systems*.
- [111] Delhaye, J M. *Thermohydraulics of reactors; Thermohydraulique des reacteurs*. France: N. p., 2008. Web.
- [112] Ishii, M.; Hibiki, T., *Interfacial Transport*. In *Thermo-Fluid Dynamics of Two-Phase Flow*; Springer: New York, 2011; pp 143–154.
- [113] C. Morel, *Mathematical Modeling of Disperse Two-Phase Flows*, Springer, Volume 114, 2015.
- [114] A. Bazylak, Liquid water visualization in PEM fuel cells: A review, *International Journal of Hydrogen Energy*, Volume 34, Issue 9, 2009, Pages 3845-3857, ISSN 0360-3199, <https://doi.org/10.1016/j.ijhydene.2009.02.084>.
- [115] Joël Pauchet, M. Prat, P. Schott, S. Pulloor Kuttanikkad, Performance loss of proton exchange membrane fuel cell due to hydrophobicity loss in gas diffusion layer: Analysis by multiscale approach combining pore network and performance modelling, *International Journal of Hydrogen Energy*, Volume 37, Issue 2, 2012, Pages 1628-1641, ISSN 0360-3199, <https://doi.org/10.1016/j.ijhydene.2011.09.127>.
- [116] Ahmad El-kharouf, Thomas J. Mason, Dan J.L. Brett, Bruno G. Pollet, Ex-situ characterisation of gas diffusion layers for proton exchange membrane fuel cells, *Journal of Power Sources*, Volume 218, 2012, Pages 393-404, ISSN 0378-7753, <https://doi.org/10.1016/j.jpowsour.2012.06.099>.
- [117] Zhong, W.; Ji, X.; Li, C.; Fang, J.; Liu, F. Determination of Permeability and Inertial Coefficients of Sintered Metal Porous Media Using an Isothermal Chamber. *Appl. Sci.* 2018, 8, 1670. <https://doi.org/10.3390/app8091670>.
- [118] Ya-Ling He, Qing Liu, Qing Li, Wen-Quan Tao, Lattice Boltzmann methods for single-phase and solid-liquid phase-change heat transfer in porous media: A review, *International Journal of Heat and Mass Transfer*, Volume 129, 2019, Pages 160-197, ISSN 0017-9310, <https://doi.org/10.1016/j.ijheatmasstransfer.2018.08.135>.
- [119] Slattery, J. C., 1969, "Single-phase Flow Through Porous Media," *AICHE J.*, 15, 866-872.
- [120] Slattery, J. C., 1981, *Momentum, Energy, and Mass Transfer in Continua*, Second Edition, R. F. Krieger.

- [121] Darcy, H., 1856, *Les Fontaines Publiques de la ville de Dijon*, Dalmont, Paris.
- [122] Whitaker, S., 1986a, "Flow in Porous Media I: A Theoretical Derivation of Darcy's Law," *Transp. Porous Media*, 1, 3-25.
- [123] Ryan K. Phillips, Brooks R. Friess, Anthony D. Hicks, Julie Bellerive, Mina Hoorfar, Ex-situ Measurement of Properties of Gas Diffusion Layers of PEM Fuel Cells, *Energy Procedia*, Volume 29, 2012, Pages 486-495, ISSN 1876-6102, <https://doi.org/10.1016/j.egypro.2012.09.057>.
- [124] Hidetaka Taira, Hongtan Liu, In-situ measurements of GDL effective permeability and under-land cross-flow in a PEM fuel cell, *International Journal of Hydrogen Energy*, Volume 37, Issue 18, 2012, Pages 13725-13730, ISSN 0360-3199, <https://doi.org/10.1016/j.ijhydene.2012.03.030>.
- [125] Jeffrey T. Gostick, Michael W. Fowler, Marios A. Ioannidis, Mark D. Pritzker, Y.M. Volfkovich, A. Sakars, Capillary pressure and hydrophilic porosity in gas diffusion layers for polymer electrolyte fuel cells, *Journal of Power Sources*, Volume 156, Issue 2, 2006, Pages 375-387, ISSN 0378-7753, <https://doi.org/10.1016/j.jpowsour.2005.05.086>.
- [126] W.G. Gray, P.C.Y. Lee, On the theorems for local volume averaging of multiphase systems, *International Journal of Multiphase Flow*, Volume 3, Issue 4, 1977, Pages 333-340, ISSN 0301-9322, [https://doi.org/10.1016/0301-9322\(77\)90013-1](https://doi.org/10.1016/0301-9322(77)90013-1).
- [127] M. J. Lighthill, *An introduction to fourier analysis and generalized functions*, Cambridge (University Press), 1958. Pp. viii, 79. 17s. 6d, <https://doi.org/10.1002/qj.49708436232>.
- [128] Slattery, J. C., 1970, "Two-Phase Flow Through Porous Media," *AIChE J.*, 16, 345-352.
- [129] Whitaker, S., 1986b, "Flow in Porous Media II: The Governing Equations for Immiscible, Two-Phase Flow," *Transp. Porous Media*, 1, 105-125.
- [130] Gray, W. G., 1983, "General Conservation Equations for Multi-Phase Systems: 4. Constitutive Theory Including Phase Change," *Adv. Water Resour.*, 6, 130-140.
- [131] Bear, J. and Bensabat, J., 1989, "Advective Fluxes in Multiphase Porous Media Under Non-Isothermal Conditions," *Transp. Porous Media*, 4, 423-448.
- [132] Hassanizadeh, S. M. and Gray, W. G., 1990, "Mechanisms and Thermodynamics of Multiphase Flow in Porous Media Including Interface Boundaries," *Adv. Water Resources*, 13, 169-186.
- [133] Hassanizadeh, S. M. and Gray, W. G., 1993, "Thermodynamic Basis of Capillary Pressure in Porous Media," *Wat. Resour. Res.*, 29, 3389-3405.
- [134] Gray, W. G. and Hassanizadeh, S. M., 1991, "Unsaturated Flow Theory Including Interfacial Phenomena," *Wat. Resour. Res.*, 27, 1855-1863.
- [135] Muskat, M., Meres, M.W. *The flow of heterogeneous fluids through porous media*. *Physics* 1936, 7: 346-363, <https://doi.org/10.1063/1.1745403>.
- [136] Brooks, R.H. and Corey, A.T. (1964) *Hydraulic Properties of Porous Media*. *Hydrology Papers* 3, Colorado State University, Fort Collins, 27 p.
- [137] I.S. Hussaini, C.Y. Wang, Measurement of relative permeability of fuel cell diffusion media, *Journal of Power Sources*, Volume 195, Issue 12, 2010, Pages 3830-3840, ISSN 0378-7753, <https://doi.org/10.1016/j.jpowsour.2009.12.105>.
- [138] F. Nandjou, J.-P. Poirot-Crouvezier, M. Chandesris, Y. Bultel, A pseudo-3D model to investigate heat and water transport in large area PEM fuel cells – Part 1: Model development and validation, *International Journal of Hydrogen Energy*, Volume 41, Issue 34, 2016, Pages 15545-15561, ISSN 0360-3199, <https://doi.org/10.1016/j.ijhydene.2016.05.117>.
- [139] R.W. Lockhart, R.C. Martinelli, Proposed correlation of data for isothermal two-phase, two-component flow in pipes, *Chem. Eng. Prog.* 45 (1949) 38-48.
- [140] Omid Babaie Rizvandi, Serhat Yesilyurt, A pseudo three-dimensional, two-phase, non-isothermal model of proton exchange membrane fuel cell, *Electrochimica Acta*, Volume 302, 2019, Pages 180-197, ISSN 0013-4686, <https://doi.org/10.1016/j.electacta.2019.02.018>.

- [141] Ghanbarian, Behzad & Hunt, Allen & Ewing, Robert & Sahimi, Muhammad. (2013). Tortuosity in Porous Media: A Critical Review. *Soil Science Society of America Journal*. 77. DOI: [10.2136/sssaj2012.0435](https://doi.org/10.2136/sssaj2012.0435).
- [142] Brinkman, H.C. A calculation of the viscous force exerted by a flowing fluid on a dense swarm of particles. *Appl. Sci. Res.* 1, 27 (1949). <https://doi.org/10.1007/BF02120313>.
- [143] Wooding, R. (1957). Steady state free thermal convection of liquid in a saturated permeable medium. *Journal of Fluid Mechanics*, 2(3), 273-285. DOI: <https://doi.org/10.1017/S0022112057000129>.
- [144] F. Nandjou, J.-P. Poirot-Crouvezier, M. Chandesris, S. Rosini, D.S. Hussey, D.L. Jacobson, J.M. LaManna, A. Morin, Y. Bultel, A pseudo-3D model to investigate heat and water transport in large area PEM fuel cells – Part 2: Application on an automotive driving cycle, *International Journal of Hydrogen Energy*, Volume 41, Issue 34, 2016, Pages 15573-15584, ISSN 0360-3199, <https://doi.org/10.1016/j.ijhydene.2016.06.007>.
- [145] D. Chisholm, "Two-Phase Flow in Pipelines and Heat Exchangers", Longman Higher Education, 1983. ISBN 0-7114-5748-4.
- [146] C.R. Wilke, A viscosity equation for gas mixtures, *J. Chem. Phys.* 18 (1950) 517–519.
- [147] Akers, W., Deans, H., & Crosser, O.K. (1955). CONDENSING HEAT TRANSFER WITHIN HORIZONTAL TUBES. *Chemical Engineering Progress*.
- [148] Cicchitti, A, Lombardi, C, Silvestri, M, Soldaini, G, & Zavattarelli, R. TWO-PHASE COOLING EXPERIMENTS: PRESSURE DROP, HEAT TRANSFER AND BURNOUT MEASUREMENTS.
- [149] Dukler, A.E., Wicks, M., III and Cleveland, R.G. (1964), Frictional pressure drop in two-phase flow: A. A comparison of existing correlations for pressure loss and holdup. *AIChE J.*, 10: 38-43. <https://doi.org/10.1002/aic.690100117>.
- [150] K. Mishima, T. Hibiki, Some characteristics of air–water two-phase flow in small diameter vertical tubes, *Int. J. Multiphase Flow* 22 (1996) 703–712.
- [151] W. Zhang, T. Hibiki, K. Mishima, Correlations of two-phase frictional pressure drop and void fraction in mini-channel, *Int. J. Heat Mass Transfer* 53 (2010) 453–465.
- [152] W. Li, Z. Wu, A general correlation for adiabatic two-phase pressure drop in micro/mini-channels, *Int. J. Heat Mass Transfer* 53 (2010) 2732–2739.
- [153] Y.S. Muzychka, M.M. Awad, Asymptotic generalizations of the Lockhart–Martinelli method for two phase flows, *J. Fluids Eng.* 132 (2010) 0313021–313112.
- [154] Sung-Min Kim, Issam Mudawar, Universal approach to predicting two-phase frictional pressure drop for adiabatic and condensing mini/micro-channel flows, *International Journal of Heat and Mass Transfer*, Volume 55, Issues 11–12, 2012, Pages 3246-3261, ISSN 0017-9310, <https://doi.org/10.1016/j.ijheatmasstransfer.2012.02.047>.
- [155] B. Straubhaar, J. Pauchet, M. Prat, Pore network modelling of condensation in gas diffusion layers of proton exchange membrane fuel cells, *International Journal of Heat and Mass Transfer*, Volume 102, 2016, Pages 891-901, ISSN 0017-9310, <https://doi.org/10.1016/j.ijheatmasstransfer.2016.06.078>.
- [156] (2020), *Fuel Cell Cathode with Liquid Water*. COMSOL Multiphysics®. Application Gallery – Application ID: 90161 <https://www.comsol.com/model/fuel-cell-cathode-with-liquid-water-90161>.
- [157] COMSOL Documentation 5.6, COMSOL Multiphysics > COMSOL Multiphysics Reference Manual > Building a COMSOL Multiphysics Model > Numerical Stabilization, <https://doc.comsol.com/5.6>.
- [158] E.G.D. do Carmo and A.C. Galeão, “Feedback Petrov-Galerkin methods for convection-dominated problems”, *Computer Methods in Applied Mechanics and Engineering*, vol. 88, pp. 1–16, 1991.
- [159] COMSOL Documentation 5.6, Fuel Cell & Electrolyzer Module, <https://doc.comsol.com/5.6>.

- [160] Pasaogullari, U., & Wang, C. Y. (2005). Two-phase modeling and flooding prediction of polymer electrolyte fuel cells. *Journal of the Electrochemical Society*, 152(2), A380-A390. <https://doi.org/10.1149/1.1850339>.
- [161] D.S. Hussey, D.L. Jacobson, M. Arif, K.J. Coakley, D.F. Vecchia, In situ fuel cell water metrology at the NIST Neutron Imaging Facility, *ASME J Fuel Cell Sci Technol* 7 (2010) 21–24.
- [162] D.S. Hussey, D.L. Jacobson, High resolution of neutron radiography analysis of proton exchange membrane fuel cells, in: U. Pasaogullari, C.Y. Wang (Eds.), *Modeling and diagnostics of fuel cells*, Springer, New York, 2010, pp. 175–199.
- [163] T.A. Trabold, J.P. Owejan, J.J. Gagliardo, D.L. Jacobson, D.S. Hussey, M. Arif, Use of neutron imaging for proton exchange membrane fuel cell (PEMFC) performance analysis and design, in: *Handbook of fuel cells: advances in electrocatalysis, materials, diagnostics and durability*, 2010.

## Appendix

### Appendix A: Local Volume-Averaged Mass Equation

The local continuity equation for mass in PEMFC considering a single-fluid flow is:

$$\frac{\partial \rho_f}{\partial t} + \nabla \cdot [\rho_f \underline{V}_f] = r_f \quad (\text{A-1})$$

When volume averaged, Eq. A-1 becomes:

$$\left\langle \frac{\partial \rho_f}{\partial t} \right\rangle + \langle \nabla \cdot [\rho_f \underline{V}_f] \rangle = \langle r_f \rangle \quad (\text{A-2})$$

The matrix volume is considered rigid, i.e. independent of time. The unsteady term in Eq. A-2 becomes:

$$\left\langle \frac{\partial \rho_f}{\partial t} \right\rangle = \frac{1}{V} \int_{V_f} \frac{\partial \rho_f}{\partial t} dv = \frac{\partial}{\partial t} \left( \frac{1}{V} \int_{V_f} \rho_f dv \right) = \frac{\partial}{\partial t} \langle \rho_f \rangle \quad (\text{A-3})$$

By using the theorem of the volume-average of a divergence in Eq. A-2:

$$\frac{\partial}{\partial t} \langle \rho_f \rangle + \nabla \cdot \langle \rho_f \underline{V}_f \rangle = \langle r_f \rangle - \frac{1}{V} \int_{A_{sf}} \rho_f \underline{V}_f \cdot \underline{n}_f da \quad (\text{A-4})$$

However, the fluid velocity is assumed to be zero at the solid-fluid interface ( $\underline{V}_f = 0$  at  $A_{sf}$ ).

The solid-fluid interface term is therefore zero:

$$\frac{1}{V} \int_{A_{sf}} \rho_f \underline{V}_f \cdot \underline{n}_f da = 0 \quad (\text{A-5})$$

Eq. A-4 becomes:

$$\frac{\partial}{\partial t} \langle \rho_f \rangle + \nabla \cdot \langle \rho_f \underline{V}_f \rangle = \langle r_f \rangle \quad (\text{A-6})$$

Finally, by including the intrinsic averages in Eq. A-6:

$$\frac{\partial}{\partial t} [\varepsilon \langle \rho_f \rangle_f] + \nabla \cdot [\varepsilon \langle \rho_f \underline{V}_f \rangle_f] = \varepsilon \langle r_f \rangle_f \quad (\text{A-7})$$

## Appendix B: Local Volume-Averaged Species Mass Conservation Equation

The local species mass conservation equation in PEMFC considering a single-fluid flow is:

$$\frac{\partial \rho_{jf}}{\partial t} + \nabla \cdot [\rho_{jf} \underline{V}_f] = \nabla \cdot [D_{mj} \nabla \rho_{jf}] + r_{jf} \quad j = 1, N_f \quad (\text{B-1})$$

By applying the local volume-average in Eq. B-1, we have:

$$\left\langle \frac{\partial \rho_{jf}}{\partial t} \right\rangle + \langle \nabla \cdot [\rho_{jf} \underline{V}_f] \rangle = \langle \nabla \cdot [D_{mj} \nabla \rho_{jf}] \rangle + \langle r_{jf} \rangle \quad (\text{B-2})$$

The matrix volume is considered rigid, i.e. independent of time. The unsteady term in Eq. B-2 becomes:

$$\left\langle \frac{\partial \rho_{jf}}{\partial t} \right\rangle = \frac{1}{V} \int_{V_f} \frac{\partial \rho_{jf}}{\partial t} d\mathbf{v} = \frac{\partial}{\partial t} \left( \frac{1}{V} \int_{V_f} \rho_{jf} d\mathbf{v} \right) = \frac{\partial}{\partial t} \langle \rho_{jf} \rangle \quad (\text{B-3})$$

By using the theorem of the volume-average of a divergence in Eq. B-3, we obtain:

$$\langle \nabla \cdot [\rho_{jf} \underline{V}_f] \rangle = \nabla \cdot \langle \rho_{jf} \underline{V}_f \rangle + \frac{1}{V} \int_{A_{sf}} \rho_{jf} \underline{V}_f \cdot \mathbf{n}_f da \quad (\text{B-4})$$

$$\langle \nabla \cdot [D_{mj} \nabla \rho_{jf}] \rangle = \nabla \cdot [D_{mj} \langle \nabla \rho_{jf} \rangle] + \frac{D_{mj}}{V} \int_{A_{sf}} \nabla \rho_{jf} \cdot \mathbf{n}_f da \quad (\text{B-5})$$

However, the fluid velocity is assumed to be zero at the solid-fluid interface ( $\underline{V}_f = 0$  at  $A_{sf}$ ).

The solid-fluid interface term in Eq. B-4 is therefore zero:

$$\frac{1}{V} \int_{A_{sf}} \rho_{if} \underline{V}_f \cdot \underline{n}_f da = 0 \quad (\text{B-6})$$

By using the theorem of the volume-average of a gradient in Eq. B-5, we have:

$$\langle \nabla \rho_{jf} \rangle = \nabla \langle \rho_{jf} \rangle + \frac{1}{V} \int_{A_{sf}} \rho_{if} \underline{n}_f da \quad (\text{B-7})$$

Which leads to:

$$\nabla \cdot [D_{mj} \langle \nabla \rho_{jf} \rangle] = \nabla \cdot [D_{mj} \nabla \langle \rho_{jf} \rangle] + \nabla \cdot \left[ \frac{D_{mj}}{V} \int_{A_{sf}} \rho_{if} \underline{n}_f da \right] \quad (\text{B-8})$$

According to Kaviany [51] (p380), the following term is zero:

$$\nabla \cdot \left[ \frac{D_{mj}}{V} \int_{A_{sf}} \rho_{if} \underline{n}_f da \right] = 0 \quad (\text{B-9})$$

The last term in Eq. B-5 represents the sorption phenomenon, i.e. the adsorption and desorption at the solid-fluid interface:

$$\frac{D_{mj}}{V} \int_{A_{sf}} \nabla \rho_{jf} \cdot \underline{n}_f da = S_{jf}^{sf} \quad (\text{B-10})$$

Finally, Eq. B-2 becomes:

$$\frac{\partial}{\partial t} \langle \rho_{jf} \rangle + \nabla \cdot \langle \rho_{jf} \underline{V}_f \rangle = \nabla \cdot [D_{mj} \nabla \langle \rho_{jf} \rangle] + \langle r_{jf} \rangle + S_{jf}^{sf} \quad (\text{B-11})$$

Which can be written according to the intrinsic and Favre averaging:

$$\frac{\partial}{\partial t} [\varepsilon \langle \rho_{jf} \rangle_f] + \nabla \cdot [\varepsilon \langle \rho_{jf} \rangle_f \overline{\underline{V}}_f] = \nabla \cdot [D_{mj} \nabla [\varepsilon \langle \rho_{jf} \rangle_f]] + S_{jf} + S_{jf}^{sf} \quad (\text{B-12})$$

where  $S_{jf}$  is the volume-averaged source term of the  $j$ -specie by electrochemical reaction:

$$S_{jf} = \varepsilon \langle r_{jf} \rangle_f \quad (\text{B-13})$$

### Appendix C: Local Volume-Averaged Species Mass Conservation Equation

The local momentum conservation is expressed by considering the following equation:

$$\frac{\partial}{\partial t} [\rho_f \underline{V}_f] + \nabla \cdot [\rho_f \underline{V}_f \underline{V}_f] = -\nabla p_f + \nabla \cdot \tau_f + \rho_f \mathbf{g} \quad (\text{C-1})$$

By applying the local volume-average in Eq. C-1 and considering the matrix volume as rigid (see A-3), we have:

$$\frac{\partial}{\partial t} \langle \rho_f \underline{V}_f \rangle + \nabla \cdot \langle \rho_f \underline{V}_f \underline{V}_f \rangle = -\nabla \langle p_f \rangle + \nabla \cdot \langle \tau_f \rangle + \langle \rho_f \rangle \mathbf{g} + \frac{1}{V} \int_{A_{sf}} (\tau_f \cdot \mathbf{n}_f - p_f \mathbf{n}_f) da \quad (\text{C-2})$$

where the last term corresponds to an average term due to the pressure and viscous forces at the solid-fluid interface:

$$\langle d \rangle^{sf} = \frac{1}{V} \int_{A_{sf}} (\tau_f \cdot \mathbf{n}_f - p_f \mathbf{n}_f) da \quad (\text{C-3})$$

## Appendix D: Saturation Development

The molar concentration (defined on the fluid volume) for the gas, vapor and liquid can be expressed as following:

$$c_g = \frac{n_g}{V_f} = \frac{n_g V_g}{V_g V_f} = \frac{P_g}{RT} (1 - s) \quad (D-1)$$

$$\begin{cases} c_{\text{vap}} = c_{\text{H}_2\text{O}} & \text{if } P_{\text{H}_2\text{O}} \leq P_{\text{sat}}(T) \\ c_{\text{vap}} = \frac{n_{\text{vap}}}{V_f} = \frac{c_{\text{sat}}^g V_g}{V_f} = (1 - s) c_{\text{sat}}^g & \text{if } P_{\text{H}_2\text{O}} > P_{\text{sat}}(T) \end{cases} \quad (D-2)$$

$$\begin{cases} c_l = 0 & \text{if } P_{\text{H}_2\text{O}} \leq P_{\text{vap}} \\ c_l = \frac{n_l}{V_f} = c_{\text{H}_2\text{O}} - c_{\text{vap}} = c_{\text{H}_2\text{O}} - (1 - s) c_{\text{sat}}^g & \text{if } P_{\text{H}_2\text{O}} > P_{\text{vap}} \end{cases} \quad (D-3)$$

where  $c$  is the molar concentration ( $\text{mol m}^{-3}$ ),  $n$ , the number of mole (mol),  $V$ , the volume ( $\text{m}^3$ ) and  $P$ , the pressure (Pa). The subscripts  $g$ ,  $\text{vap}$ ,  $l$ ,  $\text{H}_2\text{O}$ ,  $f$ , denote the gas, vapor and liquid phase, water and fluid, respectively. Saturation is defined as the volume fraction of the liquid phase:

$$s = \frac{V_l}{V_f} \quad (D-4)$$

- If  $P_{\text{H}_2\text{O}} > P_{\text{vap}}$

$$s = \frac{V_l}{V_f} = \frac{n_l * V_l^M}{V_f} = c_l * V_l^M \quad (D-5)$$

$$s = (c_{\text{H}_2\text{O}} - c_{\text{vap}}) * V_l^M \quad (D-6)$$

$$s = (c_{\text{H}_2\text{O}} - (1 - s) c_{\text{sat}}^g) * V_l^M \quad (D-7)$$

$$s = c_{\text{H}_2\text{O}} V_l^M - (1 - s) c_{\text{sat}}^g V_l^M \quad (D-8)$$

$$s = c_{\text{H}_2\text{O}} V_l^M - c_{\text{sat}}^g V_l^M + s c_{\text{sat}}^g V_l^M \quad (D-9)$$

$$s (1 - c_{\text{sat}}^g V_1^M) = c_{\text{H}_2\text{O}} V_1^M - c_{\text{sat}}^g V_1^M \quad (\text{D-10})$$

$$s = \frac{c_{\text{H}_2\text{O}} V_1^M - c_{\text{sat}}^g V_1^M}{1 - c_{\text{sat}}^g V_1^M} \quad (\text{D-11})$$

$$s = \frac{c_{\text{H}_2\text{O}} - c_{\text{sat}}^g}{\frac{1}{V_1^M} - c_{\text{sat}}^g} \quad (\text{D-12})$$

where  $V_1^M$  is the molar volume of liquid water ( $\text{m}^3 \text{mol}^{-1}$ ) defined by:

$$V_1^M = \frac{M_{\text{H}_2\text{O}}}{\rho_1} \quad (\text{D-13})$$

where  $M_{\text{H}_2\text{O}}$  is the molar mass of water and  $\rho_1$ , the density of the liquid water.  $V_1^M$  is assumed constant due to the incompressibility of liquid water. Finally, by considering the liquid and vapor phase as vapor, the ideal gas law is used to obtain the following expression:

$$s = \frac{P_{\text{H}_2\text{O}} - P_{\text{sat}}(T)}{P - P_{\text{sat}}(T)} \quad (\text{D-14})$$

- If  $P_{\text{H}_2\text{O}} \leq P_{\text{vap}}$

$$c_1 = 0 \quad (\text{D-15})$$

Which leads directly to:

$$s = 0 \quad (\text{D-16})$$

## Appendix E: Water Content Measurement by Neutron Imaging

Neutron imaging was performed at the National Institute of Standards and Technology (NIST) Center for Neutron Research (NCNR), located in Gaithersburg, Maryland, and using the BT-2 beamline. The experimental setup is detailed in [144]. An amorphous silicon detector with 0.127 mm pixel pitch was used to record images with a field of view of 20 cm x 25 cm. Images were recorded continuously with an acquisition time of 1 Hz. Neutron images presented in this work were averages of 10 consecutive images recorded at 1 frame per second (fps) to reduce random shot noise [144], which is an effective neutron image rate of 0.1 fps. A dedicated post-treatment analysis was developed to quantify the amount of water from the images. Briefly, the image of the cell in operation (intensity  $i$ ) is referenced to the dry cell image (intensity  $i_0$ ) to attain a processed image of the water. For thin sections of water, the water thickness  $t$  can be approximately obtained from the Lambert-Beer Law:

$$t = \frac{1}{\mu_w} \ln \left( \frac{i}{i_0} \right) \quad (\text{E-1})$$

where  $\mu_w$  [ $\mu\text{m}$ ] is the water attenuation coefficient measured in the calibration experiment. More comprehensive details can be found in Refs. [161]-[163]. This routine makes it possible to determine water maps of the stack as illustrated and to draw water thickness profiles according to different sections of the cell (Fig. E-1). Recall that the stack is composed of 5 cells which they are supposed to work identically, i.e. with the same water distribution, given the fact that the difference between the cell voltages remain negligible. To obtain the liquid water thickness in a single cell, we divide the value obtained on the stack by 5. Cut lines at 25% and 50% are presented in Fig. E-1. They specifically represent the outlets (25% cut line) of the reactants/product and the middle of the cell (50% cut line). Note that negative values appear on the scale of the figures because of the presence of gas bubbles in the cooling circuits during the tests. It is clear that the saturation is never negative and null when the mixture is only in the gas phase.

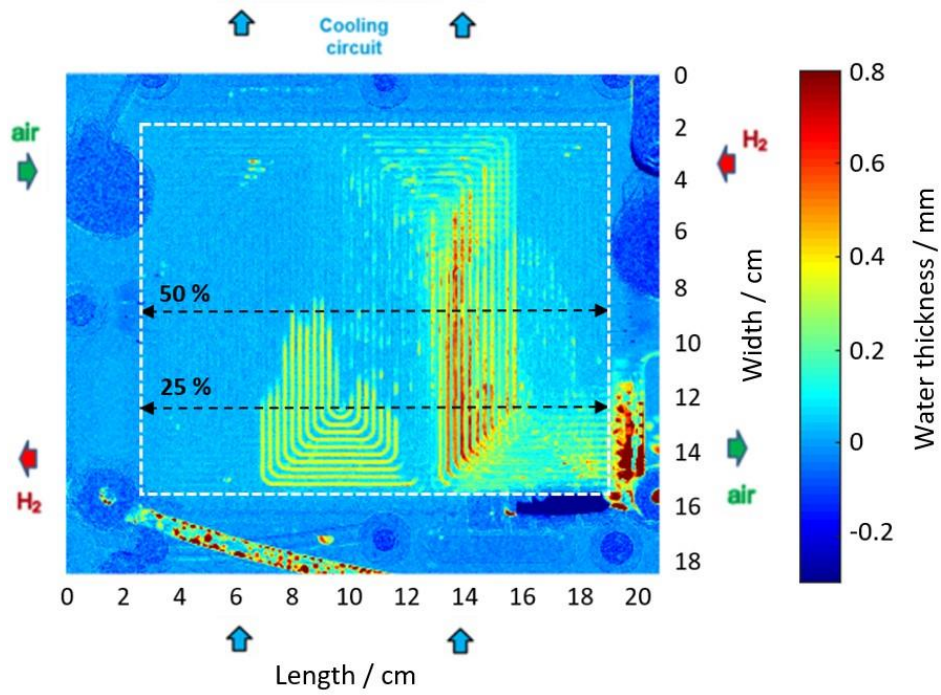


Fig. E-1. Cartography of the water thickness after post-treatment analysis. The white box represents the active area (220 cm<sup>2</sup>) and the black dashed lines represent the reference cut lines used in the Chapter III-7 results.

## Appendix F: Relationship between the Saturations $s_1$ and $s_2$ for Equal Pressure Drop

As a reminder, the pressure drop for the L-M ( $\Delta P_1$ ) and one-fluid ( $\Delta P_2$ ) models are respectively:

$$\phi_g^2 = \frac{\Delta P_2}{\Delta P_g} = \frac{\mu_2 \rho_g}{\mu_g \rho_2} \left( \frac{u_g \rho_g (1 - s_2) + u_1 \rho_1 s_2}{u_g \rho_g (1 - s_2)} \right) \quad (\text{F-1})$$

$$\Delta P_1 = \phi_g^2 \Delta P_g \quad (\text{F-2})$$

$$\Delta P_2 = 32 \mu_2 \frac{\dot{m}_g + \dot{m}_1}{\rho_2 A_c} \frac{1}{d_c^2} \quad (\text{F-3})$$

The pressure drop of both models are considered equal, i.e.  $\Delta P_1 = \Delta P_2$  and lead to:

$$\phi_g^2 = \frac{\Delta P_2}{\Delta P_g} = \frac{\mu_2 \rho_g}{\mu_g \rho_2} \left( \frac{u_g \rho_g (1 - s_2) + u_l \rho_l s_2}{u_g \rho_g (1 - s_2)} \right) \quad (\text{F-4})$$

By replacing the moist air density ( $\rho_2 = \rho_{\text{vapc}} s_2 + \rho_g (1 - s_2)$ ) in Eq. F-3, the two-phase multiplier becomes:

$$\phi_g^2 = \frac{\mu_2}{\mu_g} \frac{1}{1 - s_2} \quad (\text{F-5})$$

The Martinelli's parameter can then be expressed as a function of the pseudo-3D saturation  $s_2$ :

$$X^2 + CX + 1 - \frac{\mu_2}{\mu_g} \frac{1}{1 - s_2} = 0 \quad (\text{F-6})$$

To obtain:

$$X = \frac{1}{2} \left[ -C + \sqrt{C^2 - 4 \left( 1 - \frac{\mu_2}{\mu_g} \frac{1}{1 - s_2} \right)} \right] \quad (\text{F-7})$$

Finally, the saturation  $s_1$  described by the Lockhart-Martinelli model can be formulated according to the pseudo-3D saturation  $s_2$ :

$$s_1 = \left( 1 + \frac{u_g \mu_l}{u_l \mu_g} \frac{1}{X^2} \right)^{-1} = \left( 1 + 4S \frac{\mu_l}{\mu_g} \left[ -C + \sqrt{C^2 - 4 \left( 1 - \frac{\mu_2}{\mu_g} \frac{1}{1 - s_2} \right)} \right]^{-2} \right)^{-1} \quad (\text{F-8})$$

Appendix G:  $n_k$  Coefficient Sensitivity Study (from 2 to 5)

Fig. G-1 shows significant impact of the  $n_k$  coefficient (in the relative permeabilities) on (a) the saturation and (b) the liquid phase velocity obtained with the 1D two-fluid model.

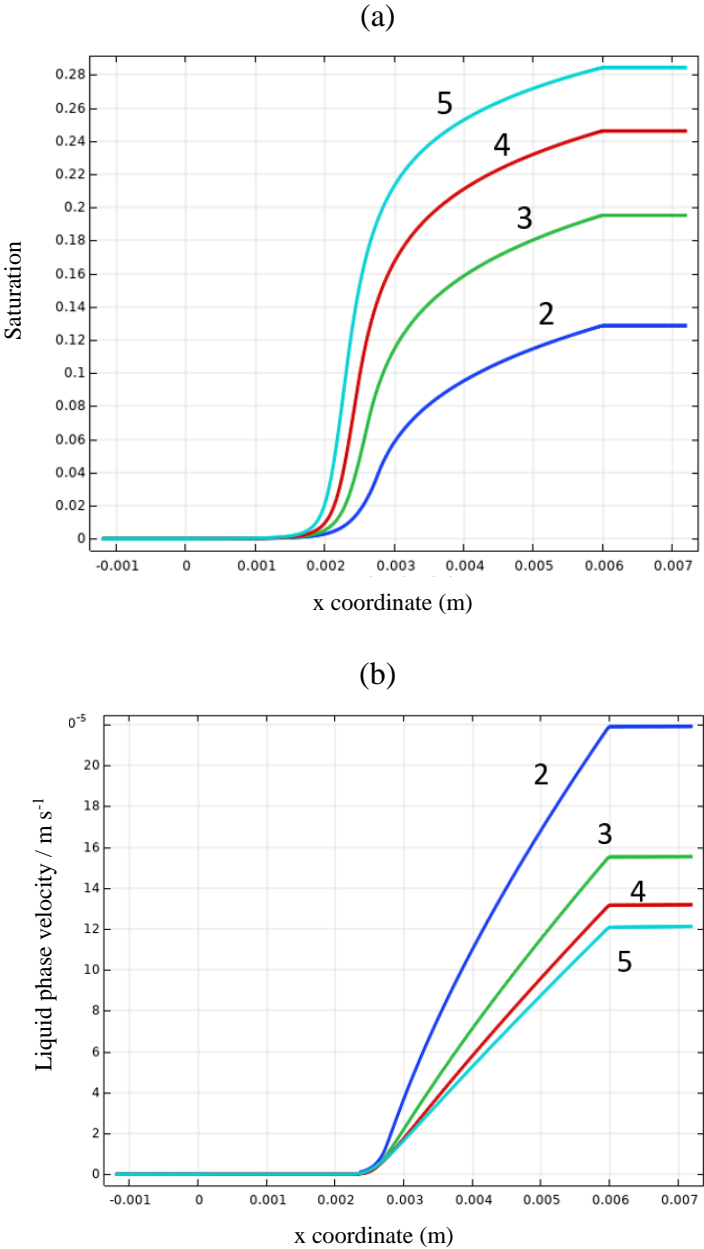


Fig. G-1.  $n_k$  coefficient sensitivity study (from 2 to 5).

## Appendix H: Physical and Geometric Parameters

The physical parameters used in the one-fluid model are presented in the next table.

### Physical parameters

Quantity		Value
<b>Bipolar plate thermal conductivity</b>		16.2 W/(m.K)
<b>Gas channels thermal conductivity</b>	Anode	0.0745 W/(m.K)
	Cathode	0.0282 W/(m.K)
<b>Gas diffusion layer thermal conductivity</b>	Anode crushed	3.6993 W/(m.K)
	Anode uncrushed	5.4062 W/(m.K)
	Cathode crushed	3.6993 W/(m.K)
	Cathode uncrushed	5.4062 W/(m.K)
<b>Micro-porous layer thermal conductivity</b>		0.4 W/(m.K)
<b>Catalyst layer thermal conductivity</b>		0.15 W/(m.K)
<b>Membrane thermal conductivity</b>		0.186 W/(m.K)
<b>Bipolar plate electric conductivity</b>		100000 S/m
<b>Gas diffusion layer electric conductivity</b>	Anode crushed	184 S/m
	Anode uncrushed	64 S/m
	Cathode crushed	184 S/m
	Cathode uncrushed	64 S/m
<b>Micro-porous layer electric conductivity</b>		50 S/m
<b>Catalyst layer electric conductivity</b>		100 S/m
<b>Membrane electric conductivity</b>		9.825 S/m
<b>Gas diffusion layer tortuosity</b>		1.23
<b>Micro-porous layer tortuosity</b>		1.6903
<b>Catalyst layer tortuosity</b>		1.3

The geometric parameters used in the one-fluid model are presented in the next table.

### Geometrical parameters

Quantity		Value
<b>Bipolar plate thickness</b>		200 $\mu\text{m}$
<b>Gas channel depth</b>	Anode	400 $\mu\text{m}$
	Cathode	400 $\mu\text{m}$
<b>Gas diffusion layer thickness</b>	Anode crushed	170 $\mu\text{m}$
	Anode uncrushed	200 $\mu\text{m}$
	Cathode crushed	170 $\mu\text{m}$
	Cathode uncrushed	200 $\mu\text{m}$
<b>Micro-porous layer thickness</b>	Anode	40 $\mu\text{m}$
	Cathode	40 $\mu\text{m}$
<b>Catalyst layer thickness</b>	Anode	5 $\mu\text{m}$
	Cathode	10 $\mu\text{m}$
<b>Membrane thickness</b>		25 $\mu\text{m}$
<b>Gas diffusion layer porosity</b>		76%
<b>Micro-porous layer porosity</b>		35%
<b>Catalyst layer porosity</b>		47%
<b>Gas diffusion layer permeability</b>		1e-8 $\text{m}^2$
<b>Micro-porous layer permeability</b>		2e-13 $\text{m}^2$
<b>Catalyst layer permeability</b>		1e-12 $\text{m}^2$

## Appendix I: Through-Plane Diffusive and Convective Mass-Fluxes

The through-plane diffusive and convective mass-fluxes for the different conservation equations due to the pseudo-3D formulation are presented in the next table.

	Diffusive ( $\Sigma J_{diff}$ )	Convective ( $\Sigma J_{conv}$ )
Species	$\varphi_{j,n} = \frac{1}{e_n} \cdot \left( \frac{1}{\frac{e_n}{2D_n} + \frac{e_m}{2D_m}} \right) \cdot ((\rho w_j)_m - (\rho w_j)_n)$	$\phi_{j,n} = \frac{1}{e_n} \cdot \left( \frac{1}{\frac{e_n}{2K_n} + \frac{e_m}{2K_m}} \right) \cdot \frac{\rho_{n,m} \cdot w_j}{\mu_{n,m}} \cdot (P_m - P_n)$
Mass	0	$\phi_n = \frac{1}{e_n} \cdot \left( \frac{1}{\frac{e_n}{2K_n} + \frac{e_m}{2K_m}} \right) \cdot \frac{\rho_{n,m}}{\mu_{n,m}} \cdot (P_m - P_n)$
Heat	$\varphi_{T,n} = \frac{1}{e_n} \cdot \left( \frac{1}{\frac{e_n}{2\lambda_n} + R_c + \frac{e_m}{2\lambda_m}} \right) \cdot (T_m - T_n)$	$\phi_{T,n} = \frac{1}{e_n} \cdot h_n \cdot (T_m - T_n)$

D: specie diffusivity  
 K: permeability  
 $\lambda$ : thermal conductivity  
 h: convection heat transfer  
 $R_c$ : thermal contact resistance

**Motive terms**

**Transport coefficients**

## **Résumé**

La pile à combustible à membrane échangeuse de protons (ou PEMFC selon l'acronyme anglais) est une candidate prometteuse pour de nombreuses applications notamment dans la décarbonation du domaine du transport. Parmi les obstacles, le coût et la durabilité représentent les deux défis principaux à relever pour le développement de systèmes pile à combustible propres, fiables et rentables. La gestion efficace de l'eau et de la chaleur produites dans les piles est indispensable pour atténuer les noyages et/ou assèchements de la membrane sur toute la plage de température de fonctionnement. Dans cette étude, deux modèles numériques ont été développés pour étudier la distribution de l'eau liquide dans les piles à combustible. Ces modèles ont été préalablement validés par comparaison à des mesures expérimentales. Ils permettent d'obtenir des informations précieuses sur la quantité d'eau dans les différents composants d'une pile à combustible.

## **Abstract**

The Proton Exchange Membrane Fuel Cell (PEMFC) is a promising candidate for many applications particularly in the decarbonation of the transport sector. Among the barriers, cost and sustainability represent the two main challenges for the development of clean, reliable and cost-effective fuel cell systems. Effective management of the liquid water and heat produced in the cells is essential to limit flooding and/or drying of the membrane over the entire operating temperature range. In this study, two numerical models were developed to study the distribution of liquid water in PEM fuel cells. These models were previously validated by comparison with experimental measurements. They provide valuable information on the amount of water in the different components of the PEM fuel cell.